Modelling protein localisation and positional information in subcellular systems

A thesis presented for the degree of

Doctor of Philosophy of Imperial College

and the

Diploma of Imperial College

by

Filipe John Tostevin

Department of Mathematics

Imperial College

180 Queen's Gate, London SW7 2AZ

APRIL 2008

I certify that this thesis, and the research to which it refers, are the product of my own work, and that any ideas or quotations from the work of other people, published or otherwise, are fully acknowledged in accordance with the standard referencing practices of the discipline.

Signed:

Copyright

Abstract

Cells and their component structures are highly organised. The correct function of many biological systems relies upon not only temporal control of protein levels but also spatial control of protein localisation within cells. Mathematical modelling allows us to quantitatively test potential mechanisms for protein localisation and spatial organisation. Here we present models of three examples of spatial organisation within individual cells.

In the bacterium *E. coli*, the site of cell division is partly determined by the Min proteins. The Min proteins oscillate between the cell poles and suppress formation of the division ring here, thereby restricting division to midcell. We present a stochastic model of the Min protein dynamics, and use this model to investigate partitioning of the Min proteins between the daughter cells during cell division.

The Min proteins determine the correct position for cell division by forming a time-averaged concentration gradient which is minimal at midcell. Concentration gradients are involved in a range of subcellular processes, and are particularly important for obtaining positional information. By analysing the low copy number spatiotemporal fluctuations in protein concentrations for a single polar gradient and two oppositely-directed gradients, we estimate the positional precision that can be achieved *in vivo*. We find that time-averaging is vital for high precision.

The embryo of the nematode *C. elegans* has become a model system for the study of cell polarity. At the one-cell stage, the PAR proteins form anterior and posterior domains in a dynamic process driven by contraction of cortical actomyosin. We present a continuum model for this system, including a highly simplified model of the actomyosin dynamics. Our model suggests that the known PAR protein interactions

are insufficient to explain the experimentally observed cytoplasmic polarity. We discuss a number of modifications to the model which reproduce the correct cytoplasmic distributions.

Acknowledgements

I am extremely grateful to my supervisor, Martin Howard, for his support over the last three and a half years. Without his guidance the completion of this thesis would not have been possible.

I also thank my friends and colleagues at Imperial College for making my time in the Maths Department so enjoyable. In particular, I would like to thank Nelson Bernardino, Daniel Lawson and Piers Ingram for stimulating discussions on various aspects of physics, maths and biology; and Nelson, Deborah Cromer and Adele Peel for their tireless work making the Department a more convivial environment. I also thank Jeroen van Zon for many interesting discussions on our various trips to Norwich.

I gratefully acknowledge financial support from the EPSRC.

Table of contents

Chapter 1

Introduction

1.1 Subcellular organisation and protein localisation

The propagation of life through the reproduction of cells requires many processes for which spatial location is important. The DNA replication machinery must form as a complex. This must then locate the correct site to initiate replication. The replicated chromosomes, plasmids and other organelles must be positioned appropriately for division. The division machinery must be correctly localised and assembled. The position of each of these elements relative to the others is important for the viability of the cell.

Many of these positioning functions are carried out by the cellular cytoskeleton. It has long been known that eukaryotic cells contain many highly ordered cytoskeletal structures, including filaments of actin and tubulin [1]. The cytoskeleton gives cells rigidity and function as tracks for motor proteins to carry vesicles to appropriate locations within the cell. These filaments and motors are also involved in generating the forces required for cell division, chromosome segregation and motility.

In recent years, our understanding of prokaryotic cells has been revolutionised. We now know that many bacterial cells contain the proteins FtsZ and MreB, which are homologues of the eukaryotic tubulin and actin proteins respectively [2, 3]. These proteins form a cellular cytoskeleton and provide rigidity and shape to the cell. Interestingly, the roles played by these proteins are often reversed from eukaryotic cells.

In bacteria, FtsZ forms the contractile division ring [4], a role played by actin in eukaryotes. MreB has been implicated in chromosome segregation and cell shape [5, 6], which require tubulin in eukaryotes. Generally, prokaryotic cells can also display remarkable levels of organisation and structure (see [7, 8] for recent reviews).

Spatial organisation is also important to enable cells to respond to external signals. While a signal may be detected at the cell membrane by receptors, the appropriate cellular response to this event may take place deep within the cell. If the signal triggers activation of a particular gene, for example, this must be transmitted from the membrane to activate transcription factors in the nucleus. Alternatively, the cell may wish to move in response to an external stimulus, such as towards a nutrient source. Then the machinery of cellular motility, be it the internal cytoskeleton or an exterior flagellum or actin tail, must be organised in such a way that the cell can move in the required direction. In order to accurately detect the direction of a signal, localisation or clustering of receptors may also be required, as in bacterial chemotaxis [9].

Protein localisation is not necessarily a static arrangement - a wealth of dynamic phenomena has also been discovered within individual cells. The development of new imaging techniques and in particular fluorescence microscopy has been key to our growing understanding of dynamic processes. The staining techniques which were previously used to study protein localisation required fixing and killing of cells. This made it impossible to record multiple images of a single cell. Attempts could be made to reproduce temporal dynamics by comparing images of different cells. However, it remained possible that these differences were due to static cell-to-cell variability rather than dynamics of a single copy of the system. With imaging of live cells it became possible to visualise a time-course of localisation within a single cell.

These novel imaging techniques led to the discovery of many examples of dynamic spatial localisation within single cells. Among the first dynamic patterns to be discovered in bacteria was the Soj/Spo0J system in *Bacillus subtilis*. Once the parent chromosome has been replicated, Spo0J accumulates at each nucleoid [10]. Soj is seen to gather in these same regions, and to move between the two points at irregular intervals [11], with a typical occupation time of tens of minutes at each position.

These jumps may be a result of fluctuations due to the limited protein numbers [12]. The exact function of the Soj/Spo0J system is not well understood, although it is thought to be involved in chromosome segregation. Even apparently static structures can however also have dynamic behaviour. The FtsZ septal ring previously appeared to be a fixed construction at midcell. However, FtsZ proteins are constantly being exchanged between the "Z-ring" and the cytoplasm [13], and a larger helical structure which extends along the length of the cell [14]. MreB filaments in *Caulobacter* appear to undergo a similar process of rearrangement from a helical distribution along the cell length to a ring at the site of division [6]. This dynamic behaviour is by no means limited to prokaryotic cells. The formation of two complementary domains of PAR proteins in *C. elegans*, described in sections 1.5 and 4, is an example of dynamic subcellular protein localisation in a multicellular organism.

Perhaps the best-studied example of dynamic protein localisation is the Min system in the bacterium *Escherichia coli*. The function of this system is to precisely locate the site for cell division to the middle of the parent cell, which is achieved through the pole-to-pole oscillation of the MinCDE proteins [15, 16]. This system will be discussed in more detail in section 1.3 and chapter 2. Mathematical modelling has proven extremely valuable for our understanding of these dynamic subcellular systems, allowing us to probe mechanisms which cannot be readily tested experimentally, and bringing together ideas from developmental biology and pattern formation.

1.2 Mathematical modelling

Traditional biological and biochemical experiments typically can reveal the complex networks of interactions between proteins. In some cases, the quantitative study of individual reactions is also possible and rates or saturation factors can be determined. However, in a complex systems of nonlinear interactions with multiple feedbacks, the dynamics of the system or the response to a particular condition may not be readily apparent, meaning that intuitive explanations may be incorrect. Here mathematical modelling plays a vital role as it allows us to qualitatively and quantitatively study these systems and mechanisms in detail. Models also enable us to investigate the

roles of particular components within the system. For example, it may be that in a system where two reaction pathways are possible, that the global behaviour of the system is dominated by one pathway over the other. This may not be obvious without the quantitative description which modelling allows. Modelling can also analyse mutations which have not been experimentally characterised, or the dynamics of a protein or other reactant which has not been measured experimentally. In this way, modelling allows us to make predictions and can then suggest new experiments to test these predictions, which helps to advance our understanding of a system.

We will consider models in which the variables represent the concentrations of reactants, and the model equations represent an approximation of the appropriate interaction network. Models of this type are often written as ordinary differential equations. In order to capture spatial phenomena, the densities of proteins must be modelled as a function of both position and time, necessitating the use of partial differential equations instead. Relocation of these proteins within the system must also be introduced. Free diffusion is generally assumed as an effective description of the motion. Models with this reaction-diffusion structure allow one to quantitatively investigate the spatial density distributions of the various proteins and how these quantities develop over time through the model dynamics.

Many of the dynamic models for biological patterning build from the complementary ideas of Turing [17] and Wolpert [18]. Wolpert introduced the idea of positional information in biological systems being encoded in density gradients of proteins. If the concentration of a protein varies with position, then by measuring the density at a point, information about position relative to the source can be obtained. This paradigm has traditionally been applied in developmental systems, where concentration gradients of morphogen proteins were initially observed. However, these ideas can equally be applied in subcellular contexts. We will return to this type of system in section 1.4 and chapter 3, where we estimate the potential accuracy of an example of this type of mechanism.

In contrast to the static predetermined gradients of Wolpert, Turing suggested that spatial patterns in biological systems could arise spontaneously due to a dynamic instability in a system which is driven out of equilibrium. This is an example

of self-organisation [19] - the appropriate pattern forms inevitably and solely due to interactions between components within the system - which is a particularly attractive property for biological mechanisms since it alleviates the requirement for a higher level of regulation. One large class of models which use dynamic instability mechanisms are the "activator-inhibitor"-type introduced by Gierer, Meinhardt and others [20]. In these models, the system is driven by constant protein production, with one protein enhancing and another inhibiting the levels of both. Models of this type have been applied to such diverse phenomena as animal markings (e.g. [21]) and the development of hair follicles [22]. More generally, pattern-forming systems in biology typically feature short-ranged activation and longer-ranged inhibition, but not necessarily through production and degradation reactions. Perhaps the most convincing application of "Turing patterns" in biology are models of the Min protein oscillations in *E. coli*, which will be discussed in more detail in section 1.3 and chapter 2. In the majority of these models, the activation and inhibition effects take the form of cooperative binding and dissociation reactions, with the total protein levels fixed.

Many subcellular components are present at extremely low copy numbers, from one to a few copies of a gene or plasmid to a few hundred protein molecules. Added to the fact that the biochemical reactions which are represented in mathematical models are intrinsically random events between discrete reactants, this means that fluctuation effects due to these low copy numbers may be highly significant. Stochastic models which include these fluctuations can therefore be considered. In such models, reaction rates are replaced by probabilities of moving between certain discrete states. The introduction of noise can make stocahstic models more difficult to analyse than the corresponding continuum model. However, the dynamic behaviour that these models reveal can be significantly different from continuum models, allowing us to probe the impact of noise in subcellular systems.

1.3 The Min system in *E. coli*

A well studied example of dynamical behaviour in bacterial systems is the Min system in *E.coli*. The Min system consists of three proteins: MinC, MinD and MinE. These

three proteins together direct cell division to mid-cell by preventing formation of the septal ring in the remainder of the cell. MinC and MinD are observed to accumulate at one cell pole [15, 16]. A MinE ring then forms at the medial end of this MinCD region, and gradually moves towards the pole [23, 24]. MinC and MinD then gather at the opposite pole. The period of these oscillation is approximately one minute.

The mechanisms by which these oscillations occur is relatively well understood. MinD:ATP first binds to the cell membrane. In the absence of MinE, MinD is distributed evenly throughout the membrane [15]. The rate of MinD accumulation, through cooperative binding or self-aggregation, increases with the amount of MinD present [25]. MinD forms oligomers [26, 27], and can form a complex with either MinC or MinE [28]. MinC inhibits polymerisation of FtsZ [29], preventing formation of the "Z-ring" which forms the basis for the division machinery. MinD enhances the effect of MinC by recruiting it to the membrane. MinC is co-localised with membrane-bound MinD [16, 30]. However, MinC is not required for the oscillation of MinD and MinE [15]. MinE is recruited to the membrane by MinD where it forms a MinDE complex and, in the process, expels MinC from the membrane [25]. MinE also stimulates ATP-hydrolysis of membrane-bound MinD, which causes dissociation of MinD from the membrane. MinD:ADP then undergoes nucleotide exchange in the cytoplasm to MinD:ATP.

There are a number of factors which make the Min system particularly susceptible to modelling. There are a small number of components within the system which must be incorporated into the model, essentially just the MinD and MinE proteins and the cell membrane. There is a large amount of experimental evidence to suggest which reactions are required within the model. For example we know that MinE will not bind to the membrane in the absence of MinD, and MinD will not dissociate from the membrane without MinE. The dynamics of the system are very regular, and so much easier to quantify and reproduce than random relocations. Finally, in filamentous *E. coli* cells, multiple regularly-spaced MinD bands form [15, 23, 24], suggesting that the molecular interactions specify a particular oscillation wavelength. A characteristic property of Turing patterns is the appearance of a typical length scale for the pattern which is independent of the system size but is instead set by microscopic parameters.

As a result of these features, a number of models [31-34] were devised which reproduced pole-to-pole oscillations. Although these models differed in the details, all were of reaction-diffusion-type, relying on a dynamical instability in the system. This showed that the *in vivo* dynamics could be achieved without the need for any additional elements in the system. It is possible for pole-to-pole oscillations to spontaneously begin simply due to the interactions between the proteins and their diffusive motion. Since the development of these models, additional experimental evidence has suggested that some details of these mechanisms are incorrect. The Meinhardt-de Boer model [31] relies on continuous protein synthesis, which is not required *in vivo*. In the model of Kruse [33], the formation of MinD polar regions relies on aggregation of membrane proteins after binding. The model by Howard et al [32] included reactions which have since been shown not to occur. Subsequent models have largely been based on the reaction scheme of [34], which introduced nucleotide exchange for cytoplasmic MinD.

The most dramatic new experimental result was that MinD formed helical filaments along the cell on the membrane [35]. Subsequently a number of new models [36-39] have been produced which attempt to incorporate this feature. In the Meacci-Kruse model [36] the membrane occupancy is limited, and MinD accumulation is due to self-aggregation once it has bound to the membrane. The model by Pavin et al [38] is a three-dimensional stochastic model incorporating MinD polymerisation, but it does not form the observed large scale helical filaments. The models by Drew et al [37] and Cytrynbaum and Marshall [39] differ somewhat in that preferential polar binding sites are specified, requiring that MinD filaments grow outward from the cell poles. This and other assumptions, such as regulating polymer growth rate according to length [37], are not required in other models. Unlike other models, the oscillations in [39] are not due to a dynamic reaction-diffusion instability, but instead are built in to the assumed polymerisation reactions.

In chapter 2 we describe one such model [40], which incorporates linear membrane polymers of MinD. This model is also a stochastic particle model rather than the continuous partial differential equation models which are more numerous. Stochastic models have been proposed in the past [38, 41], and have a number of advantages.

Since we are able to track individual particles rather than concentrations, it is easier to incorporate membrane polymerisation. We can also include the structure of these polymers, and hence vary binding probabilities according to the available binding sites. By tracking individual particles the model naturally includes fluctuations due to low protein copy numbers, which may have significant effects *in vivo*. It has been shown that such fluctuations can drive oscillations in parameter regimes where the corresponding continuum model is stable or bistable [41, 42], a strategy which may be exploited by the cell.

While the actual reaction mechanisms have been studied, other behaviour of the system has received little attention. This is an area where modelling can be of great value, by directing experiments to search for predicted behaviour. It is perhaps surprising that a system which has its function tied to cell division has not been studied in detail during the division process. We therefore apply our model to investigate how the Min system behaves during the process of division itself. We find that the distribution of the proteins into the daughter cells is highly unequal, and it would be interesting to see whether this feature is reproduced in experiments.

1.4 Noise in concentration gradients

It is widely believed that the Min system in *E. coli* is able to prevent formation of the division ring near the cell poles because the averaged concentration over the oscillation period is high near the poles and low at midcell [15, 19, 31-34, 40]. Other bacteria also employ polar gradients to direct cell division to midcell, although without pole-to-pole oscillations. *B. subtilis* produces MinC and MinD proteins but lacks MinE, and therefore the MinCD complex accumulates simultaneousy at both poles [43, 44]. MipZ is thought to play a similar inhibitory role in the bacterium *Caulobacter crescentus* [45]. Since the concentrations of MipZ/MinCD are higher near the cell poles, FtsZ accumulates near the cell centre. Below some critical threshold of MinCD or MipZ concentration, enough FtsZ will presumably accumulate to form the division apparatus. The locations where the concentration gradient crosses these thresholds mark positions within the cell.

The properties of intracellular protein gradients have been studied by Brown and Kholodenko [46]. Recently a number of other gradients have been observed experimentally in both prokaryotic and eukaryotic systems. The bacterial virulence factor IcsA forms a polar gradient on the cell membrane of *Shigella flexneri* [47]. Similarly to the MinC and MipZ division inhibitors in bacteria, cell division in eukaryotic cells is also believed to be regulated by concentration gradients. For example, in fission yeast, the protein Pom1p forms a cortical concentration gradient emanating from a cell tip, thereby restricting the cell division protein Mid1p to the cell centre [48, 49]. Also in eukaryotic cells, gradients of the Ran and HURP proteins aid the formation of the mitotic spindle by biasing microtubule growth towards the chromosomes [50-54]. Gradients may also play a role in the localisation of Cdc42 activation, thereby permitting a coupling between cell shape and protein activation [55, 56].

Prior to the discovery of these subcellular gradients, position determination by concentration gradients had been considered in the context of developmental biology [18]. The first experimental demonstration of this mechanism was the discovery of the Bicoid gradient in the *Drosophila* embryo, which regulates the expression of several genes along the anterior-posterior axis [57-59]. Many other morphogens have now been discovered which specify cell fate in a concentration-dependent manner, including different roles at different stages of development. Examples include Dpp and Wnt, which pattern the *Drosophila* wing disk [60, 61], and Shh, which is involved in patterning of the limbs [62, 63] and nervous system [64, 65] in vertebrates. Positional information is vital for development, to ensure not just the production of the correct tissue types but also their correct location relative to one another.

For a gradient mechanism to be biologically viable, position determination must be precise and therefore robust to noise. Variability from one copy of the system to another (e.g. from cell to cell or embryo to embryo) will certainly compromise positional precision. Production and degradation rates can vary, for example, due to different copy numbers of transcription factors or proteases. The physical size of the system will also vary and this may affect proper positioning. Most previous analyses of morphogen gradients have focused on robustness to changes in these extrinsic factors [66-68] between different copies of the system. However, there will also be intrinsic

noise affecting the gradient within a single copy of the system, for example due to the unavoidably noisy nature of the biochemical reactions involved. This dissection of the fluctuations into extrinsic or intrinsic mirrors that introduced into the analysis of stochastic gene expression [69-71]. However, here intrinsic noise alters not only the overall protein copy numbers (similar to [69]), but crucially also the spatiotemporal protein distribution. Even if all extrinsic variation could be eliminated, intrinsic biochemical noise would still lead to a fundamental limit to the precision of position determination, in a similar way to limits on the precision of protein concentration measurement [72, 73].

In chapter 3 we therefore examine the question of how precisely a concentration gradient can specify positional information, and calculate the limits on positional precision for a simple, but biologically relevant, gradient formation mechanism with first order reaction kinetics [74]. Quantitative measurements have suggested that concentration gradients can specify position with remarkable precision. Using mechanisms of this sort, division site placement in bacteria can achieve an impressive precision of $\pm 1\%$ of the cell length [75, 76]. The *hunchback* expression boundary in the *Drosophila* embryo is localised to midcell within $\pm 4\%$ of the embryo length. Understanding the fundamental limits to the precision of concentration gradients is therefore an important issue in both developmental and cell biology.

1.5 Polarity in the *C. elegans* embryo

Another important example of spatial organisation is cell polarity, which is used by many single cell organisms for a variety of functions. Many bacteria develop polar flagella or other structures for propulsion, sometimes in response to a polar gradient as described above [47]. The life-cycle of the bacterium *Caulobacter crescentus* features two cell types, both of which are highly polarised [77]. This asymmetry is regulated in part through localised phosphorylation and dephosphorylation of DivK at opposite poles [78]. Under starvation conditions, *B. subtilis* can undergo polarised cell division in order to create a spore [79, 80]. The eukaryotic budding yeast, *Saccharomyces cerevisiae*, also has a highly polarised cell cycle. At cell division, the new cell bud

forms adjacent to the previous division site [81, 82]. Cells can also become polarised in response to an external signal. For example, during sporulation the polarity axis of a budding yeast cell can be aligned to signals from another cell [82, 83].

Cell polarity can also play an important role in multicellular organisms. During development, many cells become polarised as part of the processes of morphogenesis [84, 85]. Epithelial cells become polarised in order to ensure tight junctions between cells [86], forming a secure boundary between internal and external environments. During the growth of neurons, polarity is essential for both cellular differentiation [87], and later for growth of axons and the correct synaptic connections between cells [88, 89]. The establishment of polarity in the *C. elegans* embryo is highly representative of more general properties of cell polarity. The PAR proteins involved are highly conserved and determine cell polarity in diverse cell types and organisms [90-92]. Polarity establishment in *C. elegans* is also coupled to actomyosin rearrangement, another feature frequently found in polarised cells [93-95].

The *C. elegans* embryo has also become an important system for the study of developmental regulation. Cell lineages are invariant, and the formation and fate of each cell has been recorded [96]. The adult *C. elegans* worm consists of 959 cells for a hermaphrodite, or 1031 cells for a male. During development growth, division and apoptosis are highly spatially and temporally regulated at the level of individual cells. The earliest stages of development are characterised by a series of asymmetric division events [96-98]. The one-cell embryo P_0 divides asymmetrically, with the division plane shifted towards the posterior pole, to produce the large anterior blastomere AB and the smaller posterior P_1. AB divides along an axis perpendicular to the anterior-posterior axis, producing A and B cells. P_1 divides later and along the anterior-posterior axis, producing the cells EMS and P_2. The temporal control and polarisation of these division events is not understood. This sequence of asymmetric cell divisions produces cells which differ not only in size but also in their cytoplasmic contents and gene expression. During the first cell cycle, P-granules and other cytoplasmic proteins which determine the germline are restricted to the posterior of P_0, so that after division they are present in P_1 but not AB [97, 99, 100]. Early embryonic cells must therefore be highly polarised in order to ensure the correct division plane

and distribution of proteins to the following generation. The PAR proteins determine polarity in the P_0 cell by marking the anterior and posterior halves of the cell. PAR-3, PAR-6 and PKC-3 (the anterior PAR proteins) occupy the cortex in the anterior half of the cell. PAR-1 and PAR-2 (the posterior PAR proteins) form a complementary posterior cortical domain [101]. PAR-4 and PAR-5 are uniformly distributed along the cell. Similar asymmetries are also seen in later generations prior to asymmetric cell divisions. The PAR proteins also regulate the position of cell division by regulating microtubule forces between the cortex and mitotic spindle [102].

The cell polarity and asymmetric accumulations of PAR proteins are not simply intrinsic to the embryo - in fact the establishment of polarity is a highly dynamic process in response to a localised polarity signal. Goldstein and Hird [103] showed that polarity was established after fertilisation, with the polarity axis determined by the position of sperm entry near the future posterior pole. Three recent studies have investigated further details of polarity establishment. Cuenca et al [104] showed that the PAR domains form gradually in an approximately 7 minute window during the 30 minute period between fertilisation and cell division. Cheeks et al [105] linked these dynamic PAR domains to flows of cortical and central cytoplasm which were previously known to carry germline factors to the posterior pole [106]. Finally, Munro et al [107] showed that the dynamic PAR domains and flows are due to contraction of a network of cortical actomyosin towards the anterior pole.

The considerable complexity of these dynamics calls for a mathematical description of the system that can quantitatively investigate possible mechanisms of polarisation. While PAR proteins have been extensively studied experimentally in different organisms, mathematical modelling of these systems has not previously been undertaken. In chapter 4 we discuss such a model for polarity establishment in the one-cell *C. elegans* embryo, which couples the known PAR protein interactions to a simple model of actomyosin contraction. This model is able to reproduce the correct polarisation of the embryo cortex, but not the observed cytoplasmic polarity which is vital for appropriate differentiation between daughter cells. This result suggests that our understanding of cytoplasmic polarity may be incomplete. We therefore consider a number of modifications enabled the model to generate the appropriate cytoplasmic

polarity, and suggest experiments that could potentially distinguish between these alternative mechanisms.

Chapter 2

Min oscillations and segregation during cell division

2.1 Introduction

In this chapter, we present a simple one-dimensional stochastic model that reproduces many of the experimental observations of the Min oscillations. We allow the MinD to form linear membrane-bound polymers along the cell length. However, as we will see, oscillatory dynamics can be reproduced independent of many of the details of the polymer structure. In our model we have therefore chosen a particularly simple implementation of membrane polymerisation. We also assume that proteins incorporated into membrane-bound polymers are fixed in place and cannot diffuse. This difference in mobility between the membrane and cytoplasm is crucial for enabling pattern formation in our model.

Although the Min oscillations have been studied in detail, there have only been a few comments describing oscillations in constricting and recently divided cells [15, 16]. We therefore use our model to investigate the Min system during these phases by incorporating division at the centre of the cell into the simulations. We find that the dynamics of the Min proteins during contraction of the Z-ring is generally consistent with the available experimental observations: the pole-to-pole oscillations continue for some time and then the dynamics changes sharply to independent oscillations on

each side of the septum.

We also study the numbers of Min proteins that are found in the two daughter cells. The numbers of Min proteins in each half of the parent cell vary greatly over the pole-to-pole oscillation period, and we find that the protein numbers in the daughter cells also vary from cell to cell over a similar range. This result suggests that the number of Min proteins may fluctuate strongly from cell to cell, but also that there may be other mechanisms for controlling protein numbers *in vivo*, such as the rates of Min protein synthesis being regulated by the Min protein concentration levels.

2.2 The model

The *E. coli* cell is modelled in 1-dimension by dividing the length L into N discrete intervals of width $\delta x = L/N$. Each interval i contains n_p^i of each of the five protein states in the model. These are cytoplasmic MinD:ADP ($p = \mathrm{D:ADP}$), cytoplasmic MinD:ATP ($p = \mathrm{D:ATP}$), cytoplasmic MinE ($p = \mathrm{E}$), membrane-bound MinD ($p = \mathrm{d}$), and membrane-bound MinDE complex ($p = \mathrm{de}$). MinE is present as a homodimer [108], so one MinE unit is actually a dimer rather than a single protein. Experiments show that MinC is not required for the oscillations, so it is not included explicitly in the modelling. Since MinC is co-localized with MinD in a MinCD complex, we assume that the amount of membrane-bound MinC can be quantified by measuring n_d^i. In our simulations we use a fixed time step δt. Simulations begin with either uniform initial protein distributions or random distributions without affecting our results.

Membrane filaments are modelled by subdividing the cell membrane into N_c linear arrays of n_{max} possible binding sites for each of the N discrete intervals. Each of the N_c arrays extends along the length of the cell, allowing filaments to grow regardless of the discretization boundaries in the cytoplasm. During the reaction steps, cytoplasmic molecules may bind to membrane sites contained within the interval they currently occupy, as shown in figure 2.1. Each of these membrane sites influences only its immediate neighbours on the membrane, and any molecules occupying neighbouring sites are considered bound in a polymer chain. The dynamical behaviour is

independent of the values of N_c and n_{max} provided the total number of membrane binding sites per cytoplasmic site, $N_c n_{max}$, is maintained. This result suggests that the overall number of MinD molecules that can bind to the membrane influences the dynamical behaviour, but the number of filaments into which they are arranged does not.

In this model we employ a particularly simple way to incorporate polymerisation, with a minimal number of assumptions about the *in vivo* polymerisation and structure. Since we can reproduce the Min oscillations with this model, the exact details of polymerisation appear not to be important for generating the experimentally observed Min dynamics. In particular we include only the basic effects which any more advanced polymerisation model must also contain, the most important of which is reduced mobility for proteins which are membrane bound. In the model, once bound to the membrane a molecule cannot move and is fixed in place until it dissociates from the membrane. We have also tested the model with diffusion of isolated membrane MinD with a similar diffusion constant to that in the cytoplasm. This change has no effect on the behaviour of the model as the amount of isolated membrane MinD is small compared to the amount of membrane MinD bound together into polymers.

All cytoplasmic proteins diffuse with diffusion constant D. The probability of a molecule moving to the left or right,

$$n_p^i \to n_p^i - 1,\ n_p^{i\pm1} \to n_p^{i\pm1} + 1, \tag{2.1}$$

in a time interval δt is $D\delta t/(\delta x)^2$.

MinD:ATP binds to the cell membrane:

$$n_{D:ATP}^i \to n_{D:ATP}^i - 1,\ n_d^i \to n_d^i + 1. \tag{2.2}$$

Cooperative binding and self-assembly of MinD are simulated by using two different rates for membrane attachment. If a MinD molecule is present on the membrane and a neighbouring membrane site is empty, cytoplasmic MinD:ATP will bind with probability $\sigma_{d,coop}\delta t$ for each such site. MinD may also bind to any other empty site

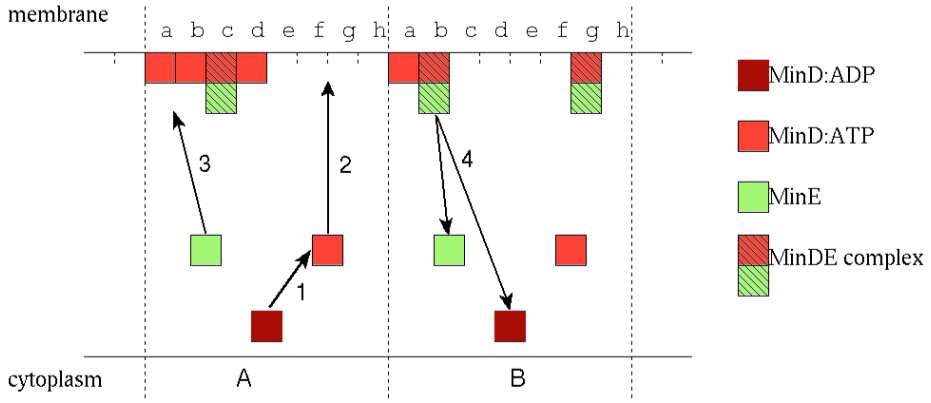

Figure 2.1: Schematic showing the model steps with one membrane filament ($N_c = 1$), with $n_{max} = 8$: 1. MinD:ADP converts to MinD:ATP. 2. MinD:ATP binds to the membrane. In this case, a MinD:ATP in cytoplasmic site A could bind at membrane position Ae or Ah with probability $\sigma_{d,coop}\delta t$, or at Af or Ag with probability $\sigma_{d,sp}\delta t$. MinD:ATP in cytoplasmic site B could bind with the lower probability to each empty site as there are no suitable sites for cooperative binding. 3. MinE binds to membrane MinD with probability $\sigma_e\delta t$ per binding site. 4. The MinDE complex dissociates, giving cytoplasmic MinD:ADP and MinE. The complex would unbind from site Bg with probability $\sigma_{dis,iso}\delta t$, since both neighbouring sites are empty; from Bb with probability $\sigma_{dis,end}\delta t$; and from Ac with probability $\sigma_{dis,bulk}\delta t$, since both neighbouring sites are occupied.

with a lower probability, $\sigma_{d,sp}\delta t$. Since the binding rate is much higher if there is already MinD on the membrane, polymer chains form as protein particles preferentially bind to the MinD already present. In the model, MinD is not allowed to bind cooperatively to the MinDE complex. If this reaction is allowed to take place at the faster rate $\sigma_{d,coop}$, then oscillations do not occur. MinD is allowed to bind adjacent to the MinDE complex, but at the slower rate $\sigma_{d,sp}$. We consider that MinE at the end of a polymer blocks the tendency for self-assembly, but cannot completely block MinD binding.

Cytoplasmic MinE may bind to a membrane-bound MinD molecule, with probability $\sigma_e\delta t$ for each such site, forming the MinDE complex:

$$n_E^i \rightarrow n_E^i - 1,\ n_d^i \rightarrow n_d^i - 1,\ n_{de}^i \rightarrow n_{de}^i + 1. \tag{2.3}$$

Dissociation of the complex releases one MinD:ADP molecule and one MinE dimer

into the cytoplasm:

$$n^i_{de} \rightarrow n^i_{de} - 1, n^i_{D:ADP} \rightarrow n^i_{D:ADP} + 1,\ n^i_E \rightarrow n^i_E + 1. \tag{2.4}$$

There are three rates for dissociation, depending on the position in the membrane array. The fastest rate and hence highest probability, $\sigma_{dis,iso}\delta t$, is for isolated molecules of the MinDE complex, which have no immediate neighbours on the membrane. The complex unbinds from the end of a chain (i.e. if it has one empty neighbouring site) with lower probability $\sigma_{dis,end}\delta t$, and from within a chain (neither neighbouring site empty) with a still lower probability $\sigma_{dis,bulk}\delta t$. These slower rates result from the existence of bonds to neighbouring units in the polymer chain. However, these different rates are not required for the oscillations, which can be achieved with a single dissociation rate independent of position. This suggests that the cooperative binding and reduced mobility introduced by polymerisation are more important in generating oscillations than the details of disassembly. However, we still include these three rates to take account of the polymer nature of the membrane proteins.

MinD is released from the membrane in the MinD:ADP form. Before it is able to rebind it must undergo nucleotide exchange to the MinD:ATP form:

$$n^i_{D:ADP} \rightarrow n^i_{D:ADP} - 1,\ n^i_{D:ATP} \rightarrow n^i_{D:ATP} + 1. \tag{2.5}$$

This occurs in an interval δt with probability $\sigma_{DT}\delta t$. This reaction step is also not required for the oscillations, but its inclusion makes the model more robust to changes in protein numbers.

2.2.1 Parameters

We use $\delta x = 0.01\mu m$ and $\delta t = 10^{-5}s$. We have checked that reducing δt by a factor of 10, or reducing δx by a factor of 4 while keeping L and the total number of membrane sites constant, does not affect our results. We take $N_c = 2$ since observations suggest that there are about two independent helical MinD filaments in living cells [35]. In our model there is no interaction between different filaments, since they are likely to be

spaced far apart on the cell membrane. MinD proteins have a length of approximately $5nm$ [27]. Assuming that during polymerisation there is some overlap or interlocking, and that the helical filaments have a relatively large angle with the cell's long axis [35], we assume it takes 6 MinD molecules to span the $\delta x = 0.01\mu m$ interval. Furthermore, MinD polymers are likely to be double-stranded [27], and we have therefore taken $n_{max} = 2 \times 6 = 12$. However, we have observed oscillations for $N_c n_{max}$ in the range 12-30 and N_c from 1 to 4, indicating a high degree of robustness in the values of these parameters. For smaller $N_c n_{max}$ values, MinD fails to form the high density polar regions required for oscillation, instead filling the membrane uniformly. For larger $N_c n_{max}$, large amounts of MinD are able to gather in small regions, and as a result regions of high MinD concentration are not observed to extend long distances across the cell.

Unless otherwise specified, simulations are performed with $L = 3\mu m$. The densities used are $\rho_D = 1000\mu m^{-1}$ MinD protein particles and $\rho_E = 400\mu m^{-1}$ MinE homodimers [109]. We use $D = 2.0\mu m^2 s^{-1}$, from experimental measurements of the diffusion rates of (unrelated) cytoplasmic proteins in *E. coli* [110]. The other parameters take the following values: $\sigma_{DT} = 1s^{-1}$, $\sigma_{d,sp} = 0.005s^{-1}$, $\sigma_{d,coop} = 30s^{-1}$, $\sigma_e = 50s^{-1}$, $\sigma_{dis,iso} = 10s^{-1}$, $\sigma_{dis,end} = 0.3s^{-1}$, and $\sigma_{dis,bulk} = 0.1s^{-1}$.

These values were chosen to fit the results of the model with experimental results, particularly the oscillation period. Increasing σ_{DT} increases the period, since MinD is able to rebind more quickly and will therefore rebind more times within one polar zone before diffusing to the opposite pole of the cell. $\sigma_{dis,end}$ controls the rate at which MinD polar zones are disassembled, and hence also has a significant effect on the period. However, the fundamental oscillatory dynamics are robust to significant changes in each of the parameter values individually. For example, oscillations persist if $\sigma_{d,coop}$ or σ_e are changed by a factor of 2. The values of $\sigma_{dis,bulk}$, $\sigma_{dis,iso}$ and $\sigma_{d,sp}$ have little effect on the dynamics, as long as $\sigma_{d,sp} \ll \sigma_{d,coop}$, although increasing $\sigma_{d,sp}$ or decreasing $\sigma_{dis,iso}$ does lead to increased noise in the oscillatory pattern.

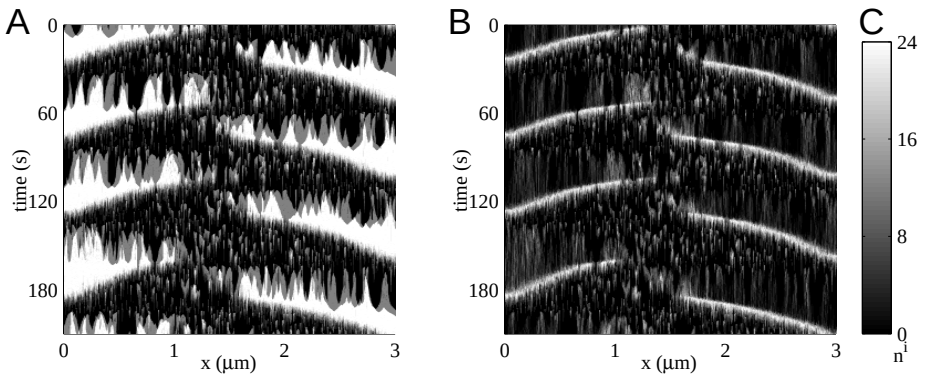

Figure 2.2: Kymograph plots of protein densities for **A** membrane-bound MinD, and **B** the MinDE complex; **C** shows the scale used.

2.2.2 Results

Pole-to-pole oscillations: Initially there is a transient period which lasts about one to two minutes, during which pole-to-pole oscillations are established. After this time, the oscillations are stable and persist over at least 90 minutes of simulated time.

In our model, MinD filaments tend not to grow out from the cell poles, instead the MinD filaments grow from random sites in the half of the cell where the concentration of MinE is lower. This is in contrast with experiment, where MinD polar regions often grow from the cell pole towards midcell. This difference in behaviour is a general feature of our model, independent of specific parameter values. In particular, it is difficult to prevent binding away from the cell pole because the MinE levels are low and roughly constant over this region. A more significant change to the model, such as adding favourable binding sites near the cell poles, could perhaps overcome these difficulties.

When a polymer has a chance to form in a region with little MinE, fast cooperative binding means the polymer grows rapidly in both directions, towards the centre and the pole of the cell. MinD polymers in regions with high MinE concentrations do not grow to a significant length, as the MinE prevents further cooperative binding and causes dissociation from the membrane. From figures 2.2 and 2.3 we can see that near mid-cell there are a large number of small patches of MinD, which are short in length and short-lived. These are quickly occupied by MinE and displaced from the

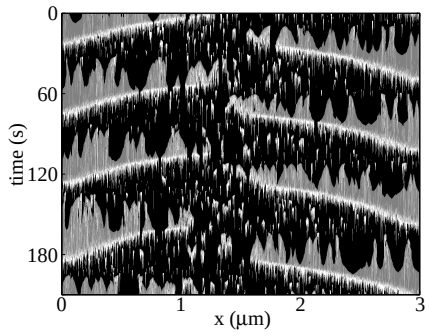

Figure 2.3: Kymograph plot for occupancy of a single membrane filament with $n_{max} = 12$ and $N_c = 2$. Black areas are empty, gray shows MinD and white is the MinDE complex.

membrane. Figure 2.3 shows that the pattern of each individual filament follows that of both filaments taken together.

As MinE relocates from the other end of the cell by cytoplasmic diffusion, it will tend to bind to the membrane at the first encountered region of elevated MinD concentration. Hence, as can clearly be seen in figure 2.2**B**, a tightly localised region of high MinE concentration (the "MinE ring") typically accumulates at the end of the region of high MinD concentration. Since MinD forms polar zones, the MinE ring is nucleated close to mid-cell and thereafter moves towards the pole, via detachment, diffusion and reattachment, as the MinD region shrinks. Although the different filaments are independent, they are disassembled simultaneously since MinE binds equally to each.

Time-averaged concentrations: Oscillation cycles were identified as periods between the MinE ring reaching one cell pole. This was done manually by looking at n^1_{de}, identifying times where the occupancy was high for an extended period, and defining the end of the cycle as the time when the occupancy dropped to below $N_c n_{max}/2$. For each of the Min proteins, the membrane density as a function of position was averaged over each oscillation cycle. Figure 2.4 shows the mean and standard deviation of these profiles over a large number of oscillation cycles. We can see that fluctuations in our stochastic model do not destroy the biologically important midcell concentration minima for MinC and MinD.

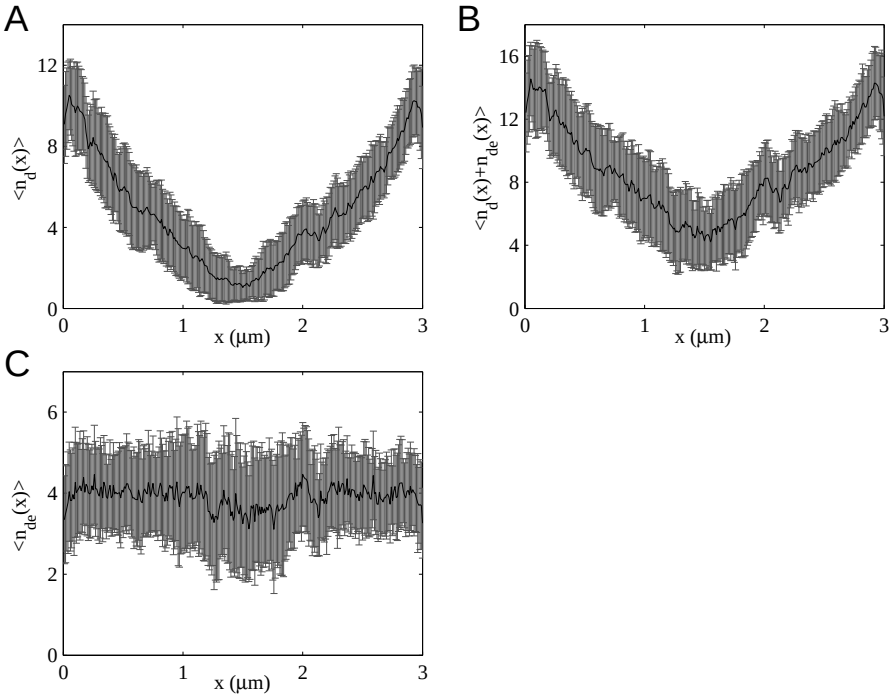

Figure 2.4: The time-averaged amount and oscillation-to-oscillation variability of **A** MinD not including the MinDE complex, **B** total MinD and **C** MinDE present on the membrane as a function of position along the cell.

The key result for cell division is that the concentration of MinC (which in our model is quantified by n_d^i) is maximised at the ends of the cell, suppressing Z-ring formation at these locations. The total amount of membrane-bound MinD, including the MinDE complex ($n_d^i + n_{de}^i$), also has a minimum around the cell centre and maxima at the cell ends. This result is in good agreement with experimental observations [36]. In our model, the average amount of membrane-bound MinE is roughly constant along the length of the cell, although with large fluctuations. This contrasts with other models which have a minimum [33, 34, 36, 38] or maximum [32] for membrane MinE at the cell centre. This profile has not been measured experimentally. Such a measurement could potentially distinguish between the various models.

Variation of period with protein numbers: Figure 2.5 shows that the oscillation period increases with increasing MinD concentration, and decreases with increasing MinE concentration. This is consistent with experimental observations [15]. The range of periods supported in this model also covers that observed *in vivo*, where the

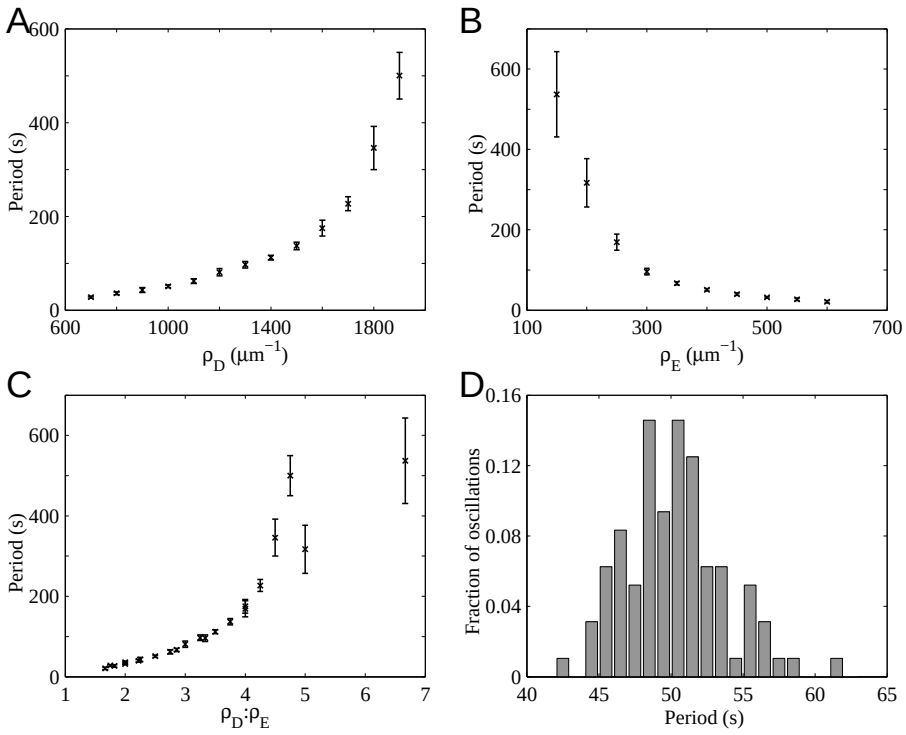

Figure 2.5: Variation of oscillation period when varying **A** ρ_D with $\rho_E = 400\mu m^{-1}$, **B** ρ_E with $\rho_D = 1000\mu m^{-1}$, and **C** $\rho_D : \rho_E$ ratio. **D** Distribution of 96 periods for the case with $\rho_D = 1000\mu m^{-1}$ and $\rho_E = 400\mu m^{-1}$. The distribution is similar in other cases. In those cases where the observed period is less than about $100s$, the standard deviation is always close to 10% of the period.

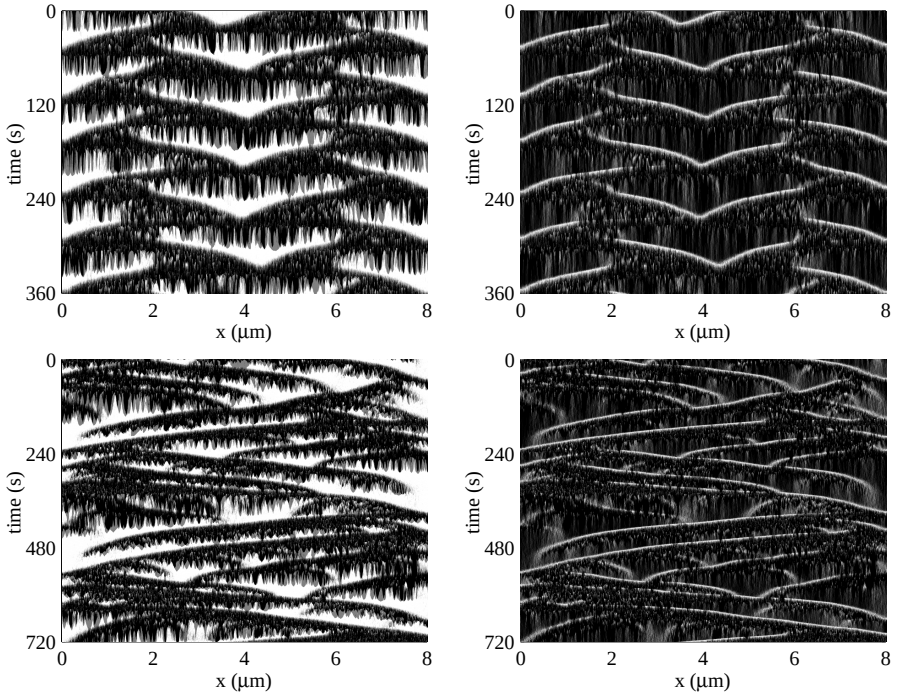

Figure 2.6: Membrane occupancy in $8\mu m$ cells, showing both periodic and more disordered dynamics. Plots on the left show membrane MinD. Plots on the right show the corresponding MinDE complex distribution.

variation is likely due to the fluctuations in protein copy numbers between different cells.

Oscillations occur for a fairly large range of $\rho_D : \rho_E$ ratios, but cut off when the $\rho_D : \rho_E$ ratio drops below about 1.6. At these concentration levels, MinD filaments are unable to grow to a significant length because they are removed from the membrane too quickly. At the opposite end of this scale there is no sharp transition; increasing $\rho_D : \rho_E$ causes the polar zones to extend further into the opposite half of the cell. Above the range shown in figure 2.5**A**, the "polar zone" effectively extends for the whole length of the cell and MinE is unable to empty the membrane.

Filamentous cells: Observations of filamentous cells which are unable to divide have revealed regularly spaced bands of MinD with accompanying MinE rings [15, 23, 24]. This is strong evidence in favour of a dynamic instability mechanism for the oscillations, since the presence of bands supports the existence of a characteristic wavelength for the dynamics independent of the cell length. Figure 2.6 shows the

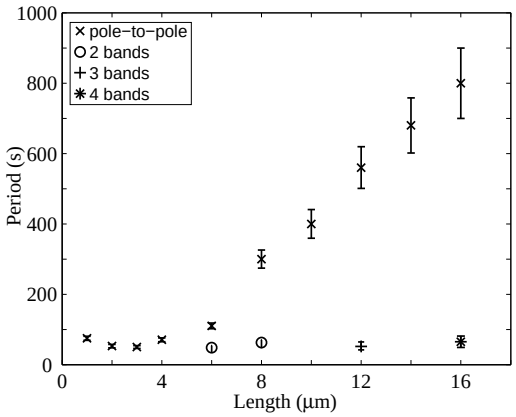

Figure 2.7: Variation of period with cell length, L.

results of simulations of our model performed in longer cells. In some cases, periodic oscillations with a number of MinD bands are observed, with the number of bands increasing with the cell length. In other cases, several regularly spaced bands form, but these all advance towards the same cell pole. In these cases the dynamics is more disordered. Such disordered behaviour has not yet been reported experimentally. However our model predicts that, while periodic behaviour may be seen over some intervals of up to 10 minutes, many filamentous cells will also have periods of irregular dynamics or switch between single and double banded oscillations. Such irregularity is perhaps not surprising given the stochastic nature of our model, and would certainly be interesting to search for experimentally.

Variation of period with length: Figure 2.7 shows the variation of oscillation period with cell length, while keeping the protein concentrations constant so the total protein number increases proportional to L. Over the range $1\mu m \leq L < 6\mu m$, where only single banded pole-to-pole oscillations are observed, the period remains approximately constant as the length is varied. The available experimental evidence [36] suggests that any change in the period with length *in vivo* is much smaller than the variation in period at constant length, which is presumably due to concentration levels differing between individual cells. When multiple oscillation bands are observed in longer cells, beginning at about $L = 6\mu m$, their period is similar to that of the pole-to-pole oscillations in shorter cells. In the case of disordered behaviour it is more difficult to

identify a characteristic period in the observed dynamics. However, the dynamics is often dominated by the bulk of the MinD sweeping regularly from one pole to the other, and we use this to find the dominant period of oscillation. For example in the lower panels of figure 2.6, $t = 230s$ to $t = 530s$ would be considered to be one period. The period of this type of oscillation increases linearly with cell length, in contrast to the roughly constant period observed for $L < 6\mu m$.

During the sweeping pole-to-pole motion in filamentous cells, MinD typically forms short bands at intervals of $3 - 4\mu m$ with an accumulation of MinE at one end. MinD dissociates from this short filament predominantly in the region where MinE is present, and tends to rebind cooperatively at opposite end. This leads to the ordered and approximately constant movement of narrow MinD bands across the cell, as seen in figure 2.6. The dynamics changes somewhat as the MinD band approaches the cell pole. The boundary prevents MinD binding at the former leading edge, leaving only the shrinking edge of the MinD region as a preferential binding site. Therefore, the overall binding rate in this region increases, slowing the net dissociation rate of MinD. This effect can be seen in figure 2.6, where it appears that shrinking of a MinD band slows down as it approaches the poles. Similar behaviour can also be seen when two MinD bands travelling in opposite directions meet, and in the regular dynamics of figure 2.6. The polar MinD zones which form in this way are similar to the continuous polar zones between the cell pole and the MinE ring which appear in shorter cells. These polar zones have a characteristic time associated with their disassembly regardless of cell length.

The results of figure 2.7 can therefore be explained by the qualitatively different dynamics which are observed in different situations. In filamentous cells, MinD bands move across the cell at approximately constant speed. This type of motion scales with cell length, giving the linear increase in period for the disorder dynamics. However, the linear variation intersects the L-axis at approximately $L = 4\mu m$. MinD bands in long cells travel less than the full length of the cell, because they form slightly away from the previously occupied pole and because as these MinD bands approach the cell pole a continuous polar zone is formed. So we can consider the oscillation period in long cells to be made up of two parts: the time to disassemble the polar zones,

which is the oscillation period in short cells, plus the time taken for the MinD bands to travel twice across about $(L-4)\mu m$ of the cell.

2.3 Oscillations during cell division

Now that we have established that our model reproduces the *in vivo* behaviour of the Min system, we use the model to investigate the Min dynamics during cell division. We investigate two mechanisms to simulate the closing septum, and examine how the Min oscillations are altered both during this process and once the daughter cells have separated. In particular we would like to study the distribution of the numbers of the Min proteins in each daughter cell, as this has not yet been measured experimentally.

Model A: Let t be the time since invagination began and T be the total time from when invagination begins to when there is no longer a cytoplasmic connection between the daughter cells. Over a length, $2l$, centred at $x = L/2$, we assume that the invagination of the cell membrane causes "compression" of the cytoplasm, making diffusion more difficult. As a result of this compression, diffusion decreases to zero in this region by time T, and unless otherwise stated we assume that this decrease occurs quadratically with time. In model A, we therefore employ a reduced diffusion probability, $D'(t)\delta t/(\delta x)^2$, in the region $L/2 - l \leq x \leq L/2 + l$ with

$$D'(t) = D_0 \left(\frac{T-t}{T}\right)^2, \tag{2.6}$$

and where D_0 is the cytoplasmic diffusion constant in the rest of the cell.

Model A provides a simple way to implement the division process. However it is perhaps unrealistic to assume that diffusion is reduced equally over the whole range $2l$, particularly as there is little clear evidence for this "compression" of the cytoplasm. This model also neglects the importance of the direction of diffusive motion, whether towards or away from the septum and into a narrower or wider region. We therefore also investigate a second, possibly more realistic, model.

Model B: Figure 2.8 shows a schematic of this mechanism. Let y be the distance from the outer edge of the narrowing region measured towards the centre. We assume

that the cell radius decreases linearly with y, and that the radius closes linearly with time:

$$r(y,t) = r_0 \left(1 - \frac{y}{l}\frac{t}{T}\right). \tag{2.7}$$

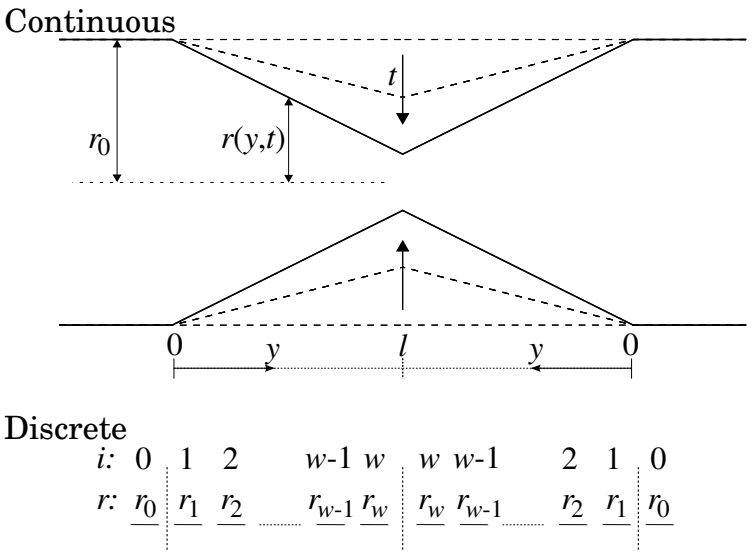

Figure 2.8: Schematic of the Model B septal region.

Equation (2.7) discretizes to give

$$r_i(t) = r_0 \left(1 - \frac{i-1}{w}\frac{t}{T}\right), \; i \geq 1. \tag{2.8}$$

where w is the number of sites in the contracting region and i is the site number counting from the polar end of this region. The presence of the -1 in the numerator simply reflects a choice in the discrete model of precisely where the invagination begins in space. The probability of diffusing into the next site towards the cell centre is assumed to vary with the ratio of the cross-sectional areas A_i, where $A_i \propto r_i^2$, since the narrowing cell radius may restrict the mobility of protein particles close to the membrane. This is equivalent to reducing the diffusion probability towards the

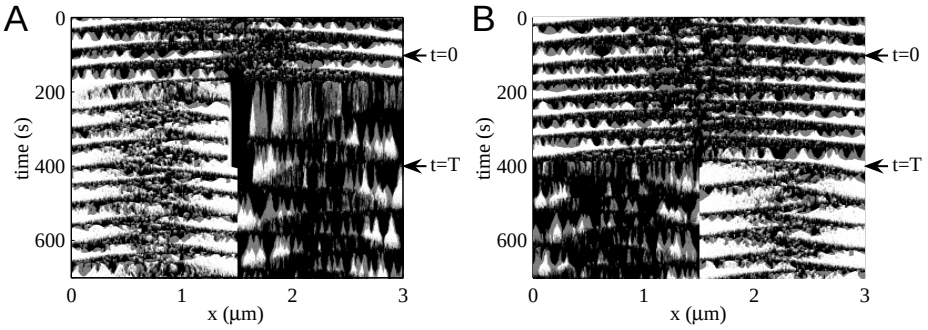

Figure 2.9: Kymograph plots showing MinD oscillations in a dividing cell, for **A** model A and **B** model B. The division process begins at the point marked $t = 0$ and ends at $t = T$. The grey-scale used is the same as in figure 2.2.

septum from site i to site $i+1$, $D_i(t)\delta t/(\delta x)^2$, according to

$$\begin{aligned} D_i(t) &= D_0 \frac{A_{i+1}(t)}{A_i(t)} \\ &= D_0 \frac{\left(1 - \frac{i}{w}\frac{t}{T}\right)^2}{\left(1 - \frac{i-1}{w}\frac{t}{T}\right)^2}, \ i = 1, \ldots, w. \end{aligned} \tag{2.9}$$

The probability of diffusion away from the septum is unchanged at $D_0\delta t/(\delta x)^2$.

Unless otherwise stated we use $T = 300s$ and $l = 0.1\mu m$ (estimated from [4]) or $w = 10$.

2.3.1 Results

Oscillations are initially unaffected as diffusion through the septum is reduced. Then at some later time diffusion through the septum cuts off sharply. After this time the two daughter cells are effectively independent, even though there remains a connection through the cytoplasm. This cut-off time varies between models but is approximately independent of the density distributions at $t = 0$. In model A, pole-to-pole oscillations cease relatively quickly, after approximately one minute. In model B, where the diffusion rate is on average greater because of the additional spatial variation, oscillations continue with little obvious alteration for about 270 seconds.

At the centre of the cell there is a region where the membrane remains empty,

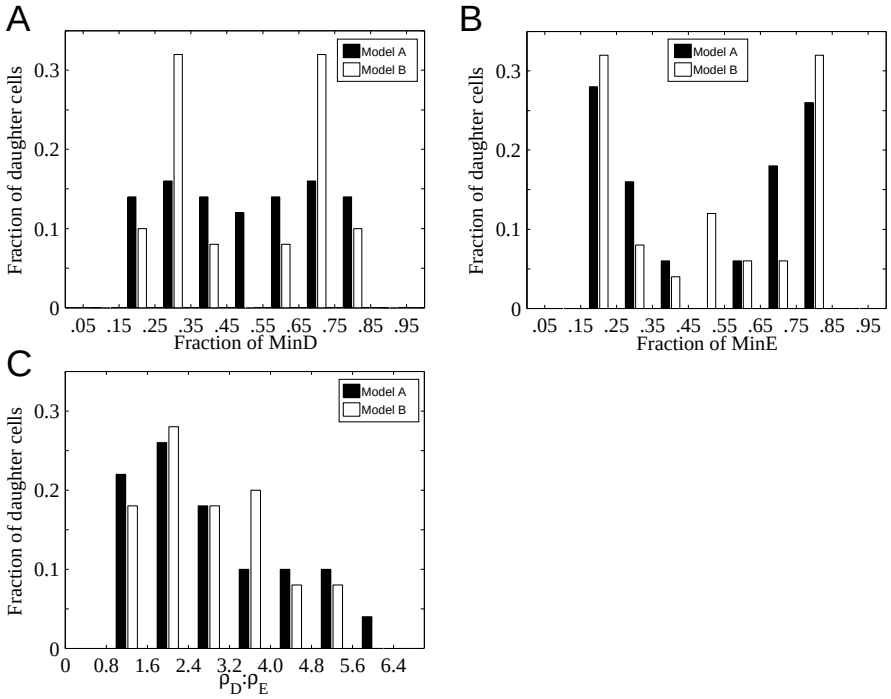

Figure 2.10: Comparison of the division models A and B, showing the distributions of the fraction of **A** MinD molecules and **B** MinE molecules from the parent cell, and **C** of $\rho_{\mathrm{D}} : \rho_{\mathrm{E}}$ ratios, in the daughter cells.

which appears at about the time when pole-to-pole oscillations are disrupted. Possibly the reduced diffusion probability makes it less likely that any proteins will be able to enter these sites, and thus reoccupy the membrane. For model A this includes about half of the contracting region, as can be clearly seen in figure 2.9**A**. At $t = T$ the empty central region is quickly reoccupied because we restore the diffusion rate to D_0 (except at $x = L/2$) and proteins can once again access these sites. For model B, the empty region extends only over a few sites at the centre of the cell and appears much later during division. Again this is due to the greater diffusion rates in model B.

Protein numbers in the daughter cells vary from 85% to 15% of the total in the parent cell for both MinD and MinE. This range is the same as the variation in protein numbers in each half of the parent cell during normal pole-to-pole oscillations. Figure 2.10 compares the daughter cell distributions between the two models. In both cases, the MinE distribution peaks at high and low concentrations. In model A, an equal distribution into the two daughter cells is never observed. The $\rho_{\mathrm{D}} : \rho_{\mathrm{E}}$ ratios in

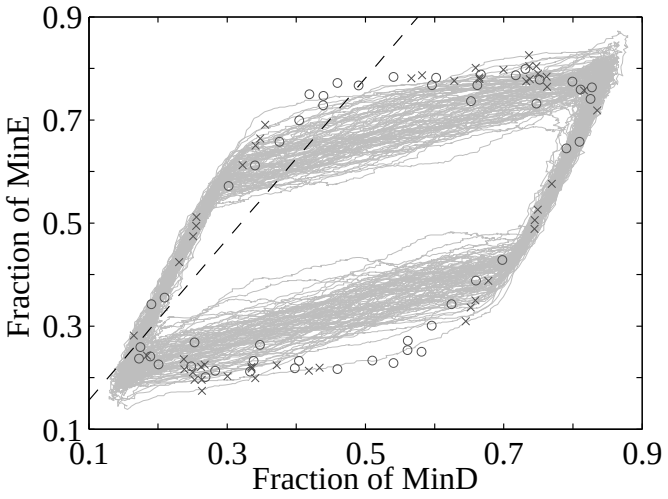

Figure 2.11: Points show the fraction of MinE from the parent cell in each daughter cell plotted against the fraction of MinD in the same cell. After division, these fractions are of course constant for each daughter cell. Circles represent model A, and crosses model B. The gray lines show the fraction of each protein in one half of the parent cell as a function of time during pole-to-pole oscillations. This is slightly disordered due to fluctuations. The dashed line indicates $\rho_D : \rho_E = 1.6$. Daughter cells to the left of this line do not have pole-to-pole oscillations.

daughter cells are also similar in the two models. Only the MinD distribution shows a significant difference between the two models. In model A, all concentrations are approximately equally likely. In model B, however, copy numbers in the daughter cells between 25-35% and 65-75% of the total from the parent cell are strongly favoured and a 50%-50% split is never observed.

The $\rho_D : \rho_E$ ratio in daughter cells ranges from about 1.3 to 6. Those daughter cells with $\rho_D : \rho_E < 1.6$, approximately 20% of the total produced in our simulations, cannot support pole-to-pole oscillations because MinD is unable to form sufficiently long filaments on the membrane. This is consistent with our results in section 2.2.2. All daughter cells with $\rho_D : \rho_E > 1.6$ did have Min oscillations. However when the protein copy number is low, polar zones are less dense and fluctuations become more significant in the dynamics.

If we plot the fractions of MinE and MinD in the same half of the parent cell as a function of time as pole-to-pole oscillations take place, the result is a cycle as shown

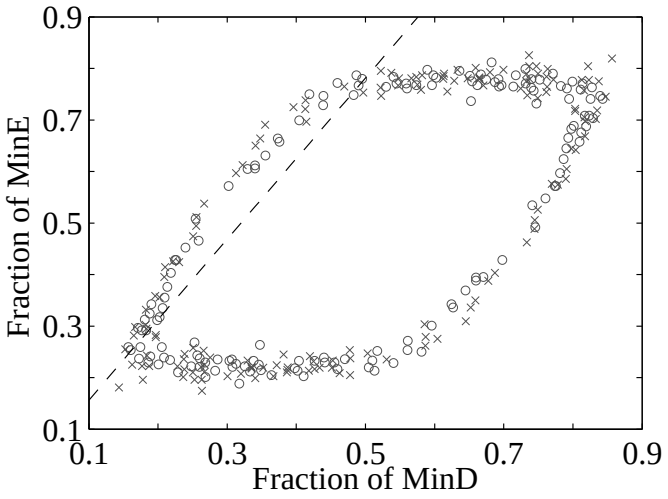

Figure 2.12: As for figure 2.11, but with data added for different w and T values and different functional time dependences.

in figure 2.11 (gray lines). During the division process, the Min protein dynamics are of course altered. Hence, as can be seen in Figure 2.11, the data points showing the fraction of the proteins ending up in the daughter cells lie on another closed loop which is similar, though not identical to, the cycle of the parent cell. We can also see that both models A and B produce daughter cells with protein fractions that lie on the same closed loop.

2.3.2 Robustness

The results presented above appear to be general and are qualitatively the same under a number of changes (discussed below) to the division models. No systematic trends were observed when varying any of the parameters in either of the models. In fact when additional data from these perturbed models is added to the data from figure 2.11, all the data points continue to lie on the same loop (see figure 2.12).

Width of contracting region: Increasing w means that the pole-to-pole oscillations of the parent cell are disrupted sooner, because the cumulative probability of diffusion from one half of the cell to the other is reduced. Conversely, if w is reduced oscillations in the parent cell will continue later into the division process. However there is no

obvious effect on the protein numbers in the daughter cells when w is increased to 20 or reduced to 5.

We have also tested the case where diffusion is reduced only when crossing from one half of the cell to the other, a limiting case of our earlier models. The observed distribution of protein numbers into the daughter cells is again the same.

Form of time-dependence: We have tested model B with $r(y,t)$ decreasing quadratically with t, and model A with linear time dependence. Again the behaviour is qualitatively the same. The time at which oscillations cease is earlier if the diffusion probability decreases more rapidly with t, and later if the diffusion probability decreases more slowly. However the distributions of the Min proteins into the daughter cells are unaffected.

Division time, T: Again the distribution of Min proteins into the daughter cells showed no systematic changes. The time at which the oscillations in the parent cell ceased appeared to vary linearly with T, suggesting that oscillations were disrupted when a minimum threshold for the diffusion probability was reached. $T = 150s$ and $T = 450s$ were tested in addition to $T = 300s$.

Stochastic vs. continuous models: We also implemented a similar mechanism to model A into continuous partial differential equation models adapted from [32] and [34]. The results obtained were qualitatively the same as those shown above. This indicates that the observed behaviour is not a result of the stochastic nature of our model.

2.4 Discussion

In this chapter we have introduced a model for the Min protein oscillations, incorporating both membrane polymerisation and stochasticity. As we have seen, the model is able to account for much of the observed Min dynamics. While the model presented above was limited to one dimension, Krstić et al performed simulations of a three-dimensional version of this model [111]. The three-dimensional model with the parameters listed above also displayed pole-to-pole oscillations, although with reduced fidelity and higher levels of noise than observed in our one-dimensional simulations.

This could potentially be improved by varying parameters. Nevertheless, this shows that the results presented above are not specific to the one-dimensional geometry we have considered, but that the mechanism proposed is more generally viable.

We have also applied our model to the dynamics of the Min proteins during cell division and found that diffusion alone is insufficient to equalise the protein copy numbers between the two daughter cells. Previous experimental observations of constricting cells [15, 16] have suggested that oscillations of the Min proteins continue unaffected well into the division process. After this time, oscillations occur separately between each pole and mid-cell, and continue once the daughter cells have separated. These features are reproduced in our simulations - oscillations cut off sharply at some time during the closing of the septum, after which the daughter cells are effectively independent even though they have not yet completely separated. However the experimental data available on this aspect of the Min dynamics are limited. There have been no experiments looking systematically and quantitatively at protein dynamics in large numbers of cells undergoing the division process. We hope that future experiments will investigate the partitioning of the Min proteins and follow the Min oscillations into the daughter cells. Although the results we have presented appear to be general and independent of the division mechanism, it is possible that other models would produce different behaviour. This provides potentially another way to test these models against experimental observations and each other.

Our simulations suggest that the distribution of the Min proteins is very often unequal and often largely skewed to one daughter cell. The variation of periods observed *in vivo* also leads us to believe that there is some variation of copy number between cells. However, in the most extreme cases of our simulations, Min oscillations are not supported in the daughter cells. Wild-type *E. coli* without pole-to-pole Min oscillations have not been reported in the literature. It may be that our model cannot reproduce oscillations at the extremes of the range where they can occur *in vivo*. However, in these cases the period of oscillation would probably lie well outside the range typically observed. This suggests that, at least in these extreme cases, some additional way of regulating protein numbers in the daughter cells may be required.

For most cytoplasmic proteins that are present in high numbers, diffusion effec-

tively distributes them evenly throughout the cell so that at division the number in each daughter cell is roughly equal. The dynamics of the Min proteins, however, means that the distributions are normally skewed greatly towards one end of the cell. From our simulations we conclude that diffusion through the septum is not by itself able to equalise the Min protein numbers in each daughter cell.

Recently, Sengupta and Rutenberg [112] performed a similar analysis of Min protein partitioning during divsion with the continuum model of Huang et al [34]. Their results were quantitatively similar to those presented above, with oscillations absent from at least 15% of daughter cells. They suggest that through a coupling of septal closure to the "phase" of the Min oscillation it is possible to ensure that both daughter cells have viable oscillations even if the distribution of Min proteins is unequal. Hoewever, our stochastic model suggests that triggering the initiation of division at a particular point in the Min oscillation cycles will not guarantee appropriate partitioning. Between the initiation of contraction of the division ring and the time the Min proteins are partitioned just before septal closure there will be a significant delay. Over this time, fluctuations in the oscillation period cause the phase of the oscillation in the stochastic model to drift relative to the corresponding continuum model. Since the time taken for the division ring to contract is much longer than the oscillation period, we found in our simulations that the phases at the initiation of contraction and at septal closure were essentially uncorrelated. In principle the coupling between division and Min oscillations could also occur at a later stage, with the contracting ring waiting for the correct Min distribution before completing division. Such a mechanism appears unlikely, since these delays in contraction are not observed experimentally. An alternative would be some form of active transport through the closing septum. This also appears unlikely, and there is certainly no experimental evidence for such a mechanism. It therefore seems improbable that the protein numbers are regulated by the division mechanism itself, which leaves open the possibility that levels are corrected shortly after division.

In our simulations, those cells which did not have Min oscillations had a ρ_D : ρ_E ratio below 1.6. This could be rectified by producing more MinD shortly after division. Additionally those cells with a very low copy number of both proteins had

small and low-density polar zones, where fluctuations had a much more significant impact on the pole-to-pole oscillations, leading to a much less pronounced MinD mid-cell concentration minimum. These cells would also benefit from increased copy numbers of both proteins. This could be achieved if the production rate of the Min proteins is controlled according to their concentrations, without needing a direct trigger from the division event. The production of the Min proteins has yet to be studied experimentally, so it is not known which, if any, factors affect their production rates.

Previous studies [113, 114] have found that there is no evidence for cell-cycle dependent protein synthesis in *E. coli*, including cell division proteins such as FtsZ and FtsA. For proteins involved in the division machinery such as FtsZ, a constant production rate is sufficient for these proteins to be equally distributed at cell division. The majority of FtsZ is cytoplasmic and so the concentration throughout the parent cell would be largely equalised by diffusion. The remaining FtsZ is located at the septum in the "Z-ring", and proteins in this structure could easily be equally divided between the daughter cells.

However, as described above, the situation for the Min proteins is likely to be rather different. Potentially the concentration levels of the Min proteins may feedback to their production (or even degradation) rates, so that, for example, their rates of synthesis increase whenever their concentrations are low. After division some cells would therefore have a burst of protein synthesis, but this would not be directly triggered due to the cell having recently divided. As the cell continues to grow the same mechanism could also keep the Min protein concentrations roughly constant. In future experiments it will be interesting to thoroughly test some of these possibilities.

Chapter 3

Intrinsic Fluctuations in Concentration Gradients

3.1 Introduction

The Min system functions by producing a time-averaged concentration gradient which is minimal at mid-cell. Concentration gradients are also employed in many other biological systems for finding positional information. However, intrinsic low copy number fluctuations will limit the potential accuracy of such systems. In this chapter we consider some simplified models of gradient formation, and calculate a limit to the potential precision of these systems due to intrinsic low copy number noise.

We first consider a system with a single planar morphogen source and linear degradation, thereby producing an exponentially decaying average concentration profile. While this model is very simple, it remains biologically relevant in both developmental and intracellular contexts. Gradients of Bicoid, Wingless and Dpp in *Drosophila* and IcsA in *Shigella* have been quantitatively measured and shown to fit this exponential decay profile on average to high accuracy [47, 115, 116]. We then calculate the expected distribution of positions where a noisy gradient crosses a concentration threshold. With typical cellular copy numbers of order a thousand proteins, these systems will be unable to identify the correct threshold position from a single measurement. In order to achieve reliable position determination the concentration must

be averaged over time. The effect of time-averaging depends strongly on the number of spatial dimensions in the system. We show that by averaging measurements, even with only the few hundred protein copies typically present in a subcellular system, precision in position determination of a few percent of the system size can be achieved, a result we verify by computer simulations. Furthermore, we find that the precision of position determination is maximised when a particular choice of the gradient decay length is made. We also show that the precision possible after a certain averaging time is independent of the detector size (i.e. the volume over which the density measurement is made) in a one-dimensional system and very weakly dependent on the detector size in two dimensions.

In our analysis we will simply postulate the existence of a well-defined critical threshold, where the gradient sharply switches a downstream signal from on to off. Clearly any real gradient cannot act as such a sharp switch – in reality a certain amount of smearing is inevitable. Furthermore, there will be additional noise in the process of actually measuring the concentration due both to the binding of the gradient proteins to the receptor molecules [72, 73], and also to the downstream reactions that process this incoming signal [69-71, 117-119]. In general, the noise of the output signal of a processing network can be written as the sum of a contribution from the noise in the input signal plus a contribution from the reactions that constitute the processing network. We assume here that the detector and the processing network are ideal and do not add any noise to the gradient input signal. As a result, our calculated variation constitutes a lower bound; any real gradient signalling system will inevitably have a lower precision.

We also consider the ability of gradients from two poles to identify the centre of the system, as in the MipZ and Pom1p gradients which regulate the position of cell division in *Caulobacter* and fission yeast respectively [45, 48, 49]. As before, we find that the precision of the system can be optimised by a particular choice of the decay length. However, if the threshold position is set at the system centre, time-averaging improves precision more slowly than in the single-source model. For subcellular gradients we find that a few thousand copies of the gradient proteins may therefore be required for high precision. Our results strongly constrain the possible

concentrations of gradient proteins in two gradient systems.

Gradient systems with interactions have also been proposed theoretically for the control of *hunchback* positioning in *Drosophila* [67, 68, 120]. In these systems, two opposite polar gradients are formed by different proteins which react and cause the inactivation or degradation of one another. We find that this mechanism typically is able to locate the central position more precisely that the two non-interacting gradients described above.

3.2 A simplified gradient model

We consider a protein gradient which is used to determine a particular position along the length of a cylindrical system. We will let d be the spatial dimension of the system. We choose the x-axis along the long axis of the system. Position in the remaining coordinates is denoted by the vector $\mathbf{y}$. The system length is L, and the size of the system in the remaining directions is taken to be $L_\perp$. For $d = 2$, periodic boundary conditions are appropriate in the y-direction, so $L_\perp = 2\pi r$, where r is the system radius. Otherwise, zero-flux boundary conditions are used throughout. A source on the $x = 0$ plane produces proteins at rate J per unit area, which then diffuse with diffusion constant D, and are degraded uniformly at rate μ. Neglecting fluctuations, the protein concentration $\rho(x, \mathbf{y}, t)$ will be described by

$$\frac{\partial \rho}{\partial t} = D\nabla^2\rho - \mu\rho + J\delta(x). \tag{3.1}$$

If $L \gg \lambda = \sqrt{D/\mu}$, the characteristic decay length of the gradient, we find that, at steady state, the density is

$$\rho(x) = \frac{J\lambda}{D} \exp\left(-x/\lambda\right). \tag{3.2}$$

Symmetry dictates that the average density is independent of $\mathbf{y}$. Gradients with the form (3.2) have been found to accurately fit quantitatively measured concentration profiles in both developmental [115, 116] and subcellular [47] systems.

While we have outlined the model in terms of production and degradation, (3.1)

could equally apply to other mechanisms in which the active protein originates in a single location, but deactivation occurs uniformly throughout the system. The same equation would therefore describe a protein which is phosphorylated by a polar-localised kinase and dephosphorylated by a uniformly distributed phosphatase, or a protein which is activated by being injected into the membrane at a pole and deactivated when it dissociates. These biochemical details do not affect the behaviour of the model.

We suppose that signalling is active where the local gradient protein concentration is above some threshold value, ρ_T, and inactive otherwise. The average concentration profile for a single gradient, (3.2), suggests that the system will be divided into a region $0 \leq x < x_T$ where signalling is active, and a region $x_T \leq x \leq L$ where signalling is not active, with $\rho_T = \rho(x_T)$. However, noise in the local protein concentration will cause this threshold position to fluctuate. This noise may come from intrinsic fluctuations in the diffusion, injection and decay processes, or from extrinsic factors which produce systematic changes in the boundary position when comparing one copy of the system to another. Here we consider only intrinsic biochemical fluctuations.

Protein production and degradation events are considered to be single molecule reactions with a fixed probability per unit time, and hence will be Poisson processes. We also assume that the hopping of proteins in or out of a particular region of space is governed by Poisson statistics, thereby generating a diffusive process for molecular transport. Since the system is linear, the instantaneous fluctuations in molecular number, n, within a volume $(\Delta x)^d$ centred on the position $(x, \mathbf{y})$ should also obey Poisson statistics, with

$$\left\langle n(x)^2 \right\rangle - \left\langle n(x) \right\rangle^2 = \left\langle n(x) \right\rangle . \tag{3.3}$$

In terms of protein density, this becomes

$$\left\langle (\Delta\rho(x))^2 \right\rangle = \left\langle \rho(x)^2 \right\rangle - \left\langle \rho(x) \right\rangle^2 = \frac{\left\langle \rho(x) \right\rangle}{(\Delta x)^d}. \tag{3.4}$$

This relation can also be established using more elaborate field theoretic techniques (see [121]). From this expression for the variation in the density we can compute the width of the threshold position distribution by expanding about the average threshold

position x_T. To leading order, this width is given by

$$w_0 = \frac{\Delta\rho(x_T)}{|\,\langle\rho'(x_T)\rangle\,|} = \sqrt{\frac{\lambda D}{J(\Delta x)^d}}\exp\left(x_T/2\lambda\right), \tag{3.5}$$

where $\rho'(x_T)$ denotes the first derivative of the density at $x = x_T$.

We identify $(\Delta x)^d$ as the size of the region in which the concentration is being measured. For subcellular gradients involved in positional information, this volume will be determined by the size of an individual receptor or protein with which the gradient protein interacts, an example being the interaction between the MinCD and FtsZ proteins in *B. subtilis*. The size of the detector, Δx, will then be on a molecular scale. This conclusion still holds even if the gradient proteins bind cooperatively to the "detection" protein/receptor due to the close physical proximity of the bound molecules. In contrast, however, the cellular length scale will be much larger, 1μm or bigger. Such small detector sites will lead to very low average occupancies, and hence to large density fluctuations. To quantify this, we consider the examples of IcsA in *Shigella* and Pom1p in fission yeast. Since both proteins are localised to the cell membrane, we consider systems with $d = 2$.

A cell will typically have a few thousand copies of IcsA [122], forming a gradient with $\lambda \approx 0.5\mu$m [47]. We take the detector size to be $\Delta x = 0.01\mu$m, consistent with an interaction between IcsA and actin nucleation proteins. For diffusion on the cell membrane, we take $D = 1\mu\text{m}^2 s^{-1}$. On the membrane of a cell of this size, there would be approximately $LL_\perp/(\Delta x)^2 \sim 10^5$ potential detector sites, many more than the typical copy number. Even near to the source pole, detector sites will typically be unoccupied. A detector region at a distance $x = 0.5\mu$m from the highly-occupied pole will have average occupancy of $\langle n\rangle \sim 10^{-1}$. In the cytoplasm of a similarly sized bacterium, the number of potential detector sites will be $\sim 10^6$, again much larger than the protein copy numbers typically supported by bacteria.

Similar estimates can be made for single polar gradients in fission yeast ($L = 10\mu$m, $L_\perp = 6\mu$m), such as for Pom1p [48, 49]. Here we assume a total of 2000 protein copies (this concentration has not yet been measured but this number is plausible

[49]). We also take $D = 1\mu m^2 s^{-1}$ and a decay length of $\lambda = 2\mu$m, parameters that are approximately consistent with the Pom1p gradient imaged by Padte et al [49]. We again assume that $\Delta x = 0.01\mu$m corresponding to a molecular sized detector, as would be the case if the gradient protein interacted with other membrane proteins (such as Mid1p) [48, 49]. The typical occupancy of a $\Delta x = 0.01\mu$m site is then $\langle n \rangle \sim 10^{-2}$ at $x = 2\mu$m from the source.

Average detector site occupancies that are very much less than one ensure that the threshold concentration must necessarily be less than one protein per site. Since most regions will be devoid of any copies of the protein, a single instantaneous measurement of the protein density cannot give a good estimate of the local average concentration. Additionally, multiple positions where the concentration crosses ρ_T will be observed simultaneously in such a measurement since the concentration will be above the threshold everywhere there is a protein molecule present, and below the threshold where there is no protein molecule. In order to reliably determine the average concentration profile the system must therefore integrate the measured concentration over time.

3.2.1 Time averaging

The noisy concentration profile provided by the gradient protein forms the input signal that is then time-averaged by a downstream signal processing network. In general, the mechanism for time averaging is provided by the lifetimes of the states in the processing network. For instance, in the case of gene expression, fluctuations in the occupancy of the promoter by a gene regulatory protein can be filtered by the lifetime of the mRNA transcript, provided that lifetime is much longer than the timescale of fluctuations in the promoter occupancy [71, 73]. Similarly, for subcellular gradients, as in *Shigella*, fluctuations in the gradient can be filtered by the lifetime of activated receptors/detector proteins or their downstream products. Provided this time scale is much longer than the sub-millisecond timescale of the gradient fluctuations, then good time-averaging can be achieved. Importantly, the reactions in the downstream network not only time-average the noise of the input signal, but also add further noise

to the signal [69-71, 117-119]. Here, we focus exclusively on noise in the concentration gradient and do not model the downstream reactions explicitly, but simply assume they are noiseless and model them with an effective averaging time. In essence we assume that the detector and the network that the process the gradient signal are ideal and do not add further noise, and are thus able to time-average the gradient signal in the best possible way. Our results thus provide a lower bound to the output noise set by the Poissonian fluctuations of the signalling molecules.

If we were to average over N independent measurements of the density, we would expect the error in this average to decline as $N^{-1/2}$. If we can take independent measurements at intervals of τ_{ind}, then averaging over a time-interval τ we would expect to take $N_\tau = \tau/\tau_{ind}$ independent measurements of the concentration. We would then expect that the fluctuations in the concentration will decrease according to $1/\sqrt{N_\tau}$. In reality, measurements will generally be taken at much shorter intervals than this. This will lead to correlations between consecutive measurements. For a series of correlated measurements taken at time intervals δt over a period $0 \leq t \leq \tau$, with $\tau \gg \delta t$, the expected error for the time-averaged concentration at position $\mathbf{x} = (x, \mathbf{y})$, $(\Delta\rho(\mathbf{x}, \tau))^2$, is given by [123]

$$(\Delta\rho(\mathbf{x}, \tau))^2 = \frac{\delta t}{\tau}(\Delta\rho(\mathbf{x}, 0))^2 \left[1 + \frac{2}{\delta t}\int_0^\tau \left(1 - \frac{t}{\tau}\right) C(t)dt\right], \tag{3.6}$$

where $(\Delta\rho(\mathbf{x}, 0))^2$ is the variance of a single measurement,

$$(\Delta\rho(\mathbf{x}, 0))^2 = \left\langle \rho(\mathbf{x}, 0)^2 \right\rangle - \left\langle \rho(\mathbf{x}, 0) \right\rangle^2, \tag{3.7}$$

and $C(t)$ is the normalised density correlation function,

$$C(t) = \frac{\langle \rho(\mathbf{x}, t)\rho(\mathbf{x}, 0)\rangle - \langle \rho(\mathbf{x}, 0)\rangle^2}{\langle \rho(\mathbf{x}, 0)^2\rangle - \langle \rho(\mathbf{x}, 0)\rangle^2}. \tag{3.8}$$

We therefore define the timescale τ_{ind} to be

$$\tau_{ind}(\tau) = 2\int_0^\tau \left(1 - \frac{t}{\tau}\right) C(t)dt, \tag{3.9}$$

and assuming $\tau_{ind} \gg \delta t$ we recover

$$\Delta\rho(\mathbf{x},\tau) = \Delta\rho(\mathbf{x},0)\left(\frac{\tau_{ind}(\tau)}{\tau}\right)^{1/2}. \tag{3.10}$$

For large enough values of τ we can therefore interpret τ_{ind} as the time-interval required for successive measurements to be independent.

The correlation function $C(t)$ will be determined solely by the reaction-diffusion dynamics of the proteins in the model. For pure diffusion, we expect:

$$C_{diff}(t) \sim \begin{cases} 1 & \text{for } t \ll \frac{(\Delta x)^2}{D} \\ \left(\frac{(\Delta x)^2}{Dt}\right)^{d/2} & \text{for } t \gg \frac{(\Delta x)^2}{D} \end{cases}. \tag{3.11}$$

On time scales $t \ll (\Delta x)^2/D$ the system remains perfectly correlated as there has been insufficient time for particles to hop away to neighboring sites. However, for $t \gg (\Delta x)^2/D$, an algebraically decaying correlation function is found, characteristic of diffusion. Adding decay to the system simply alters the correlation functions by a multiplicative factor of $\exp(-\mu t)$. We therefore have

$$C(t) \sim e^{-\mu t}\begin{cases} 1 & \text{for } t \ll \frac{(\Delta x)^2}{D} \\ \left(\frac{(\Delta x)^2}{Dt}\right)^{d/2} & \text{for } t \gg \frac{(\Delta x)^2}{D} \end{cases}. \tag{3.12}$$

This can now be used in (3.9) to find the leading order contributions to τ_{ind}. In the biologically relevant limits where $\tau \gg (\Delta x)^2/D$ and $1/\mu \gg (\Delta x)^2/D$, and assuming $\lambda \lesssim L$ so that boundary effects can be neglected, the leading order terms are found to have the following forms:

$$d = 1 \qquad \tau_{ind} \sim \frac{(\Delta x) l}{D} \tag{3.13}$$

$$d = 2 \qquad \tau_{ind} \sim \frac{(\Delta x)^2}{D}\left(\ln\left(\frac{l^2}{(\Delta x)^2}\right) + \text{constant}\right) \tag{3.14}$$

$$d \geq 3 \qquad \tau_{ind} \sim \frac{(\Delta x)^2}{D}. \tag{3.15}$$

In $d = 3$ or greater we find the mean-field result, in which diffusion rapidly removes any correlations between density measurements. However, in $d = 2$, density correlations decay away more slowly, leading to the appearance of logarithmic corrections. The length scale l represents the maximum distance over which density correlations persist, which is approximately set by the maximum distance over which particles can diffuse in time τ. For $\tau\mu \ll 1$, $l \sim \sqrt{D\tau}$ is determined purely by diffusion. Protein decay effectively caps the possible l at longer time-scales, so for $\tau\mu \gg 1$ we have $l \sim \lambda$. In one dimension, density correlations persist much longer, since diffusion is far more restricted, and so these correlations have a large effect on time-averaging.

3.2.2 Two- and three-dimensional systems

With the instantaneous width and the appropriate averaging time for density measurements, we can now determine the effective limiting width of these time-averaged measurements. Here we will restrict ourselves to the two- and three-dimensional systems which are of most biological importance. The system will have dimension $d = 2$ if the gradient is restricted to the membrane, or $d = 3$ if the gradient is in the cytoplasm.

From (3.10), we see that the uncertainty in density measurements goes as

$$\Delta\rho(\mathbf{x}, \tau) = \Delta\rho(\mathbf{x}, 0) \left(\frac{\tau_{ind}(\tau)}{\tau} \right)^{1/2}. \tag{3.16}$$

Combining this with (3.5), we have

$$w(\tau) = \frac{\Delta\rho(x_T, \tau)}{|\langle \rho'(x_T) \rangle|} = \frac{\Delta\rho(x_T, 0)}{|\langle \rho'(x_T) \rangle|} \left(\frac{\tau_{ind}(\tau)}{\tau} \right)^{1/2} \tag{3.17}$$

$$= w_0 \left(\frac{\tau_{ind}(\tau)}{\tau} \right)^{1/2}. \tag{3.18}$$

For long averaging times, $\tau \gg 1/\mu$, the width determined from time-averaged mea-

surements will be

$$w(\tau) = k_{2d}\left[\frac{\lambda}{\tau J}\exp\left(x_T/\lambda\right)\left(\ln\left(\frac{\lambda^2}{(\Delta x)^2}\right)+\alpha\right)\right]^{1/2} \tag{3.19}$$

in $d = 2$, and for $d = 3$

$$w(\tau) = k_{3d}\left[\frac{\lambda}{\tau J(\Delta x)}\exp\left(x_T/\lambda\right)\right]^{1/2}, \tag{3.20}$$

where k_{2d}, k_{3d} and α are constants.

As we have discussed above, Δx will be set by the concentration detection mechanism. However, in a subcellular context, Δx also sets the highest possible resolution of the system. Once $w \approx \Delta x$ the cell cannot resolve the target position with any higher precision. Equation (3.19) suggests that in $d = 2$, precision depends only very weakly on the detector size, through the logarithmic correction factor. Reducing the detector size will increase the number of independent measurements made in a given averaging time. However, since fewer proteins will be measured by each detector over one averaging period, reducing Δx will therefore increase the instantaneous density fluctuations. In $d = 2$ these two effects will largely cancel. Hence, even if we have over/underestimated the detector volume, this will have little effect on the precision of two dimensional gradients, such as IcsA in *Shigella* or Pom1p in fission yeast. In three dimensions, however, w varies as $(\Delta x)^{-1/2}$. Since increasing Δx reduces w in both $d = 2$ and $d = 3$, an optimal strategy would be to choose Δx to match the desired precision in order to minimise the required averaging time.

Intriguingly, from equations (3.19) and (3.20) we find that there exists an optimal decay length such that precision is maximised. This result can be understood as follows: for fixed x_T, and for $\lambda \gg x_T$, the value of $|\langle\rho'(x_T)\rangle|$ tends to a constant J/D, independent of x_T. However, as λ increases, $\langle\rho(x_T)\rangle$ increases and therefore the absolute size of the fluctuations in the density also increases. Therefore, for large and increasing values of λ, $w \propto \langle\sqrt{\rho(x_T)}\rangle/|\langle\rho'(x_T)\rangle|$ must be increasing. Now if λ is small ($\lambda \ll x_T$) and decreasing, when computing the width $\propto \langle\sqrt{\rho(x_T)}\rangle/|\langle\rho'(x_T)\rangle|$ the presence of the square root means that the numerator decreases much more slowly

than the denominator. Hence the width must again increase as λ is decreased for small λ. Combining these results for small and large λ, the width must have a minimum, optimum value as a function of λ. This occurs at $\lambda = x_T$ in $d = 3$. In $d = 2$, the optimal decay length is given approximately by

$$\lambda \approx x_T \left(1 - \frac{1}{\ln(x_T/(\Delta x))}\right), \tag{3.21}$$

where we have retained the first order logarithmic correction.

Simulations

In order to examine the biological impact of equation (3.19) we again consider the Pom1p membrane gradient in fission yeast [48, 49], using the parameters described earlier. Simulations of this example system were performed with on average 100 proteins in the system on a two-dimensional square lattice with $N_x = L/\delta x$ sites in the x-direction and $N_y = L_\perp/\delta x$ sites in the y-direction, where $\delta x = 0.01\mu m$ is the lattice spacing. The detector size Δx was normally set equal to δx except for cases where the detector size was varied, in which case Δx was set to be a multiple of δx. Zero-flux boundaries were implemented at $x = 0$ and $x = L$, and a periodic boundary was used to connect $y = 0$ with $y = L_\perp$. A fixed time step, $\delta t = 2.5 \times 10^{-5} s$, was chosen so that for the given diffusion constant the total probability of diffusion out of a site in all directions approached 1. However, a timestep 5 times smaller was also tested with no effect on any of the results. For each $x = 0$ site, particles were injected at each time step in a Poisson process with mean $j = J\delta x\delta t$. Diffusion and decay were also treated as Poisson processes, with hopping and decay probabilities of $D\delta t/(\delta x)^2$ and $\mu\delta t$ per particle respectively. Simulations were initialised with the mean number of particles in the system, $JL_\perp/\mu$ for the one-gradient model or twice this value for the two-gradient model, with a probability distribution that followed the average density distribution.

The mean occupancy for each detector site was calculated over the averaging period, τ. For each site this mean occupancy was compared with each neighbouring site. If one occupancy was above the threshold and the other below, this boundary

was identified as a threshold crossing position. This process was repeated for many averaging periods, ranging from 10^5 repeats for short averaging times to 500 repeats for very long averaging times, to generate a distribution of crossing positions throughout the system. Threshold crossings in both the x- and $y-$directions were observed. We found that the distributions as a function of $x-$position of these two types of crossing were the same. For each row of sites, $x = 0$ to $x = L$ at fixed y, the mean ("measured threshold") and root-mean-squared deviation ("width") of the threshold distribution from many averaging periods were calculated independently.

The standard parameter values used in the simulations were as follows: $L = 10\mu m$, $L_\perp = 6\mu m$, $D = 1\mu m^2 s^{-1}$, $\mu = 0.25 s^{-1}$, $J = 4.17\mu m^{-1} s^{-1}$, $\Delta x = 0.01\mu m$, $x_T = 2\mu m$. To generate the data collapse in figures 3.1**C** and **F**, simulations were also performed with: $D = 0.5\mu m^2 s^{-1}$; $J = 6.25\mu m^{-1} s^{-1}$; $\Delta x = 0.02\mu m$; $\mu = 1 s^{-1}$; $\mu = 0.11 s^{-1}$; $x_T = 1\mu m$; $x_T = 3\mu m$.

Results

Figures 3.1**A** and **B** show how the measured threshold position, $\bar{x}$, and width, w, vary with averaging time. For long averaging times the simulation data gives excellent agreement with (3.19), with the constants $k_{2d} = 0.40 \pm 0.02$ and $\alpha = 2.5 \pm 0.8$. Figure 3.1**C** shows the $w \sim \tau^{-1/2}$ behaviour predicted in (3.19), and figure 3.1**D** confirms that the width has a minimum as a function of λ. The simulation results are consistent with the position of the minimum predicted by (3.21). Figure 3.1**E** shows that the distribution of measured threshold positions is Gaussian to a good approximation.

Since the averaging timescale τ_{ind} in a subcellular system is of order $\sim 10^{-4} s$, time-averaging over a period of minutes can achieve great precision even with very few copies of the gradient protein. With the parameter values given above, equation (3.19) predicts that the position $x_T = 2\mu m$ can be located to within $\pm 0.5\mu m$ within an averaging time $\tau = 60s$ even if the system contains on average only about 20 copies of the protein. $\pm 0.1\mu m$ precision can be achieved in the same averaging time with around 400 copies of the protein, a remarkably high level of precision for such a low concentration. *In vivo* Pom1p gradients may be formed by a few thousand protein

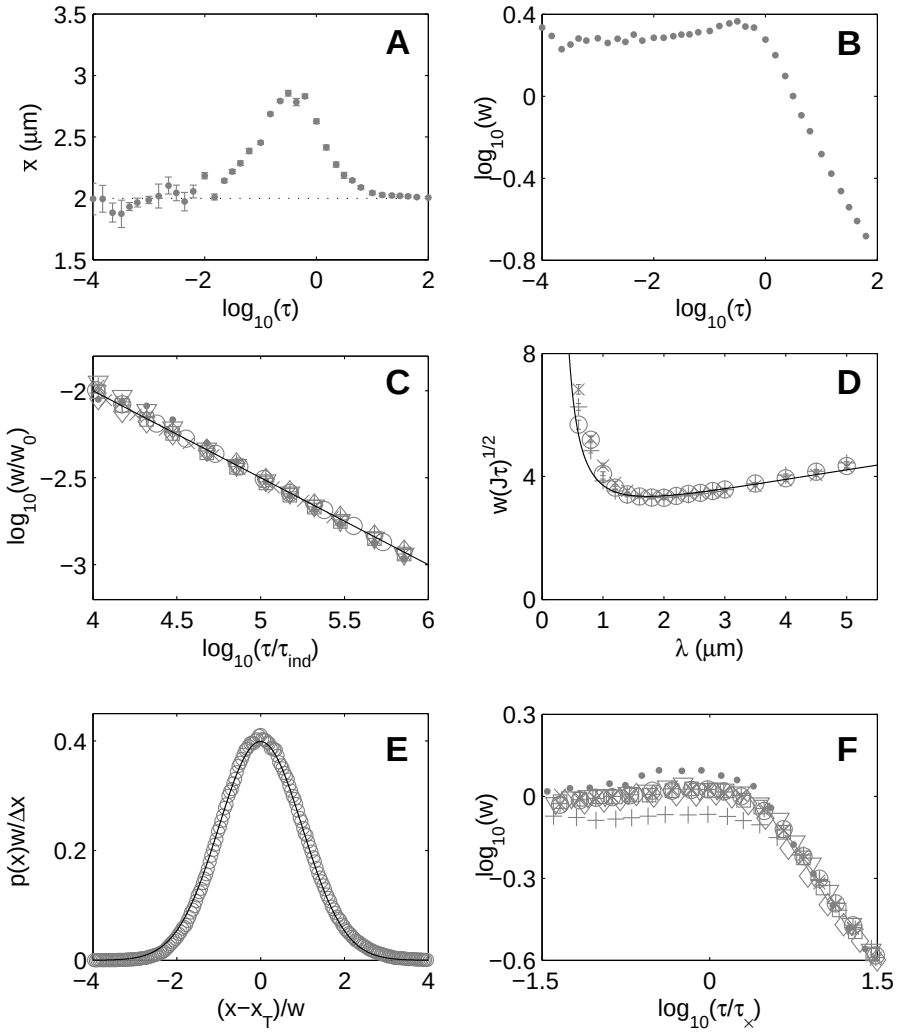

Figure 3.1: Simulation results for our simple gradient model in $2d$. **A** Variation of the estimated threshold position with averaging time, with $x_T = 2\mu m$ and $\lambda = 2\mu m$. **B** Variation of the width as a function of averaging time. **C** Data collapse of the width at large τ for a range of parameter values. Full line shows the prediction of equation (3.19) with $k_{2d} = 0.40$ and $\alpha = 2.5$. **D** $w(\tau)$ as a function of decay length, with $x_T = 2\mu m$. Results for three different averaging times are shown: $\times$: $\tau = 10s$; $\circ$: $\tau = 15s$; and $+$: $\tau = 22.5s$. The full line shows the prediction from equation (3.19). At large λ the simulation results deviate from the prediction since the assumption that $L \gg \lambda$ is no longer valid. **E** Plot of the probability distribution for measuring the threshold at position x with an averaging time $\tau = 45s$. The full line shows a normal distribution. **F** Scaling of the cross-over time, $\tau_\times$, according to equation (3.25). In figures **A**, **B** and **E** the standard parameter values given in the text were used. In figures **C** and **F**, $*$ indicates the standard parameter values. For the other data sets one parameter value was changed as follows: $\circ$: $D = 0.5\mu m^2 s^{-1}$; $\square$: $J = 6.25\mu m^{-1} s^{-1}$; $\times$: $\Delta x = 0.02\mu m$; $\bullet$: $\mu = 1s^{-1}$; $+$: $\mu = 0.11s^{-1}$; $\diamond$: $x_T = 1\mu m$; ∇: $x_T = 3\mu m$.

copies, allowing for even greater precision.

However, we can see in figure 3.1**B** that for averaging times of less than about a second, the simulation results are not consistent with (3.19). In this regime both w and $\bar{x}$ are equal to λ. As discussed above, at very short averaging times the presence of a particle at any position will cause the time-averaged concentration to be above ρ_T at that point and hence generally will generate a threshold crossing. The probability distribution of threshold measurements, $p(x)$, will therefore follow the probability distribution of particles. Assuming $L \gg \lambda$ we have

$$p(x)dx = \lambda^{-1} \exp(-x/\lambda)dx. \tag{3.22}$$

The cell will on average estimate the threshold position to be

$$\bar{x} = \int_0^L xp(x)dx \approx \lambda, \tag{3.23}$$

and measurements will be distributed about this position with variance

$$w^2 = \int_0^L (x - \bar{x})^2 p(x)dx \approx \lambda^2. \tag{3.24}$$

The system is therefore unable to resolve the correct threshold position at these short time scales if this is different from λ. Associated with the average concentration at the threshold is a length scale, $l \sim \rho_T^{-1/d}$, the typical distance between proteins at this position. The average time for a protein to diffuse this distance will scale as l^2/D. In two dimensions, this time is given by

$$\tau_\times \sim (\langle \rho(x_T) \rangle \, D)^{-1} = (J\lambda)^{-1} \exp(x_T/\lambda). \tag{3.25}$$

Since $\tau_\times$ is the timescale on which a diffusing particle first arrives at x_T, if $\tau \ll \tau_\times$ there will generally be no particles detected at x_T in the averaging period. The system therefore cannot reliably estimate the mean concentration at x_T, and hence cannot precisely identify the threshold position. For averaging times much greater than $\tau_\times$, on average at least one particle will be detected at x_T. The time-averaged

concentration profile will then approach (3.2), and $\bar{x}$ will approach x_T. Hence $\tau_\times$ determines the cross-over time between the two observed regimes of constant w and $w \propto \tau^{-1/2}$. Figure 3.1**F** shows that the scaling in equation (3.25) is also reproduced in our simulations. For the parameter values above, $\tau_\times = 0.3s$, and for a more realistic copy number of 1000, $\tau_\times = 0.03s$. These timescales are extremely short compared to cell cycle timescales, but do nevertheless show that some sort of time averaging is probably essential: a single instantaneous measurement is unlikely to provide precise positional information. In fact, as we have seen, averaging over much longer times (tens of seconds) may be necessary if very high (1%) precision is required.

Note that in section 3.2.1 we predicted that there would be another regime at short averaging times $\tau\mu \ll 1$, where the width goes as

$$w(\tau) = k_{2d}\left[\frac{\lambda}{\tau J}\exp\left(x_T/\lambda\right)\left(\ln\left(\frac{D\tau}{(\Delta x)^2}\right)+\alpha\right)\right]^{1/2}. \tag{3.26}$$

This is not observed in the simulations shown above because, at short times $\tau \ll \tau_\times$, we enter the constant $w \sim \lambda$ regime. For the parameter values used, the transition from $w \sim \lambda$ at $\tau \ll \tau_\times \approx 0.3s$ to the long time behaviour (3.19) for $\tau \gg 1/\mu \approx 4s$ overwhelms the small logarithmic effect. The cross-over in the behaviour of w at $\tau_\times$ appears as a result of comparing density measurements to a fixed threshold. However, when considering fluctuations in the underlying density itself this threshold is not important, so there is no such cross-over. The short-time behaviour predicted in equation (3.26) is therefore observable in the fluctuations in the protein density, as shown in figure 3.2. If the production rate J were increased significantly, the $\tau_\times \propto J^{-1}$ and $1/\mu$ timescales could be separated further and the $\ln\tau$ scaling may then affect the positional accuracy of the system. However, even in this case, the logarithmic variation in (3.26) is intrinsically weak, and will likely have a negligible effect in a biological context.

Simulations of the model in three dimensions were also performed. Similar behaviour was observed in this case, and equation (3.20) gave good agreement with the observed width at long averaging times. This is shown in figure 3.3.

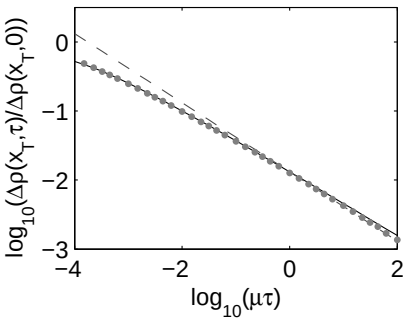

Figure 3.2: Uncertainty in time-averaged density measurements at short averaging times. The dashed line indicates the expected long time behaviour $\Delta\rho(x_T,\tau) \sim \Delta\rho(x_T,0)\left(\frac{(\Delta x)^2}{D\tau}\left(\ln\left(\frac{\lambda^2}{(\Delta x)^2}\right)+\alpha\right)\right)^{1/2}$. The full line includes the logarithmic τ-dependence expected at short times, $\Delta\rho(x_T,\tau) \sim \Delta\rho(x_T,0)\left(\frac{(\Delta x)^2}{D\tau}\left(\ln\left(\frac{D\tau}{(\Delta x)^2}\right)+\alpha\right)\right)^{1/2}$. The standard model parameters were used.

3.2.3 One-dimensional results

One-dimensional systems of this type are less likely to be biologically important than the two- and three-dimensional systems discussed previously. While biological gradients often determine position along one dimension, it is harder to find examples where the proteins themselves are confined to a one-dimensional space. Nevertheless, these one-dimensional systems show several interesting features which differ from the results in higher dimensions.

In one dimension, for large τ averaging time takes the form

$$\tau_{ind} \sim \frac{(\Delta x)\lambda}{D}. \tag{3.27}$$

The time-averaged width is therefore given by

$$w(\tau) = k_{1d}\sqrt{\frac{\lambda^2}{J\tau}}\exp(x_T/2\lambda). \tag{3.28}$$

We can therefore see that in one dimension the potential accuracy of the system is fully independent of the detector size, Δx, provided $w \gg \Delta x$. The optimal decay length is now $\lambda = x_T/2$, significantly different from the optimal $\lambda \approx x_T$ which is seen

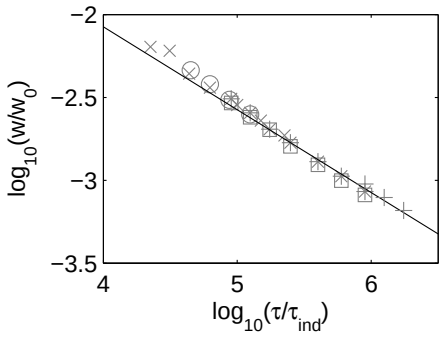

Figure 3.3: Data collapse of the width at large τ in $d = 3$ for a range of parameter values. Full line shows (3.20) with $k_{3d} = 1.2$. The parameter values are as follows: $*$:$L = 10\mu m$, $L_\perp = 6\mu m$, $D = 1\mu m^2 s^{-1}$, $\mu = 0.25 s^{-1}$, $J = 25\mu m^{-2} s^{-1}$, $\Delta x = 0.01\mu m$, $x_T = 2\mu m$; $\circ$: as $*$ except $D = 0.5\mu m^2 s^{-1}$; $\times$: as $*$ except $\Delta x = 0.02\mu m$; $\square$: as $*$ except $\mu = 0.11 s^{-1}$; $+$: as $*$ except $\mu = 0.11 s^{-1}$, $J = 10\mu m^{-2} s^{-1}$.

in higher dimensions. Figure 3.4**A** and **B** show that these results are reproduced in simulations.

In one-dimension, the early time regime $\tau\mu \ll 1$ is readily observable. Here the time-averaged width is given by

$$w(\tau) = k_{1d} \left(\frac{\lambda\sqrt{D}}{J\sqrt{\tau}} \right)^{1/2} \exp(x_T/2\lambda). \tag{3.29}$$

The change between $w \sim \tau^{-1/2}$ and $\tau \sim \tau^{-1/4}$ can readily be seen in figure 3.4**C**.

As in two-dimensions, there will be a crossover period at which time-averaging begins to improve positional accuracy. In general, this will be set by the typical time between proteins reaching the detector site. As before, we can identify a diffusive timescale for proteins to visit the detector site,

$$\tau_{diff} \sim \frac{l^2}{D} \sim \frac{D \exp(2x_T/\lambda)}{J^2\lambda^2}. \tag{3.30}$$

However, there is an additional constraint on the time between proteins visiting the detector site. The average flux across the site at position x_T will be

$$J_{x_T} = -D\frac{\partial\rho}{\partial x}|_{x_T} = J\exp(-x_T/\lambda). \tag{3.31}$$

In order to achieve this flux, the typical time between proteins reaching x_T cannot be longer than

$$\tau_{flux} \sim \frac{1}{J_{x_T}} \sim \frac{\exp(x_T/\lambda)}{J}. \tag{3.32}$$

The typical time between particles visiting the detector site will be the shorter of these two timescales. The crossover time at which time-averaging affects the measured width, $\tau_\times$, will therefore be set by τ_{flux} when

$$\tau_{diff} > \tau_{flux} \tag{3.33}$$

$$\frac{D\exp(2x_T/\lambda)}{J^2\lambda^2} > \frac{\exp(x_T/\lambda)}{J} \tag{3.34}$$

$$\frac{D\exp(x_T/\lambda)}{J\lambda^2} > 1 \tag{3.35}$$

This condition can be written in a number of different ways, such as $\rho_T\lambda < 1$, or in terms of the average number of proteins in the system, $N = J/\mu < \exp(x_T/\lambda)$. Therefore, we would expect to observe this regime when protein densities are extremely low. When the density is low, the diffusive timescale underestimates the frequency with which proteins visit the detector site. When $\rho_T < 1/\lambda$, proteins may in fact typically be closer to the detector site than $1/\rho_T$, because the curvature of the concentration profile has been neglected. Figure 3.4**D** shows simulation results confirming the appearance of this additional timescale.

Why is the second timescale not observed in two dimensions? The constraint on the flux across the target position must also apply in higher dimensions. In $d = 2$, the diffusive timescale is

$$\tau_{diff} \sim \frac{l^2}{D} \sim \frac{\exp(x_T/\lambda)}{J\lambda}. \tag{3.36}$$

The flux across a single detector site is

$$-D\frac{\partial\rho}{\partial x}|_{x_T}(\Delta x) = J(\Delta x)\exp(-x_T/\lambda), \tag{3.37}$$

giving a timescale of

$$\tau_{flux} \sim \frac{\exp(x_T/\lambda)}{J(\Delta x)}. \tag{3.38}$$

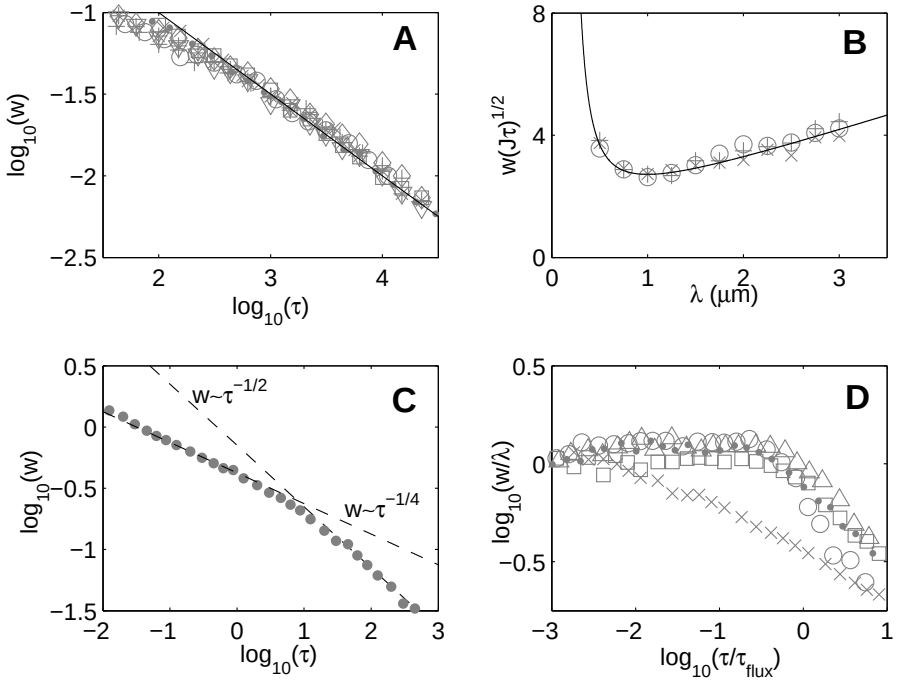

Figure 3.4: Simulation results for a single gradient in one dimension. **A** Scaling collapse for $w(\tau)$ as a function of τ, confirming (3.28). The fitting constant was $k_{1d} = 1$. **B** Variation of w with λ, showing the optimal decay length at $\lambda = x_T/2$ for $x_T = 2\mu m$. Results are shown for: $\times$: $\tau = 20s$; $\circ$: $\tau = 45s$; and $+$: $\tau = 90s$. The full line shows equation (3.28). **C** The switch between the $\tau^{-1/2}$ and $\tau^{-1/4}$ regimes predicted by (3.28) and (3.29). **D** The appearance of the τ_{flux} crossover timescale in one dimension. The $\times$ trace is representative of a parameter combination for which the τ_{diff} cross-over applies. Parameters: For panels **A** and **C**, $*$ indicates the standard parameter values of $L = 10\mu m$, $\Delta x = 0.01\mu m$, $D = 1\mu m^2 s^{-1}$, $\lambda = 2\mu m$, $J = 25s^{-1}$, $x_T = 2\mu m$. For the other data sets one parameter value was changed as follows: $\circ$: $D = 0.5\mu m^2 s^{-1}$; $\square$: $J = 2.5s^{-1}$; $\times$: $\Delta x = 0.02\mu m$; $\bullet$: $\lambda = 1\mu m$; $+$: $\lambda = 3\mu m$; $\diamond$: $x_T = 1\mu m$; ∇: $x_T = 3\mu m$. In **B**, the standard parameters were used. Parameters in **D** are as for **A**, but with $\triangle$: $J = 10s^{-1}$, $\lambda = 1\mu m$; and $\circ$: $J = 10s^{-1}$, $\lambda = 0.5\mu m$.

Thus for any $\lambda > \Delta x$ the diffusive timescale is dominant in higher dimensions.

3.2.4 Two non-interacting gradients

In order to reliably locate the centre of a system, the mechanism responsible must incorporate information about the overall system size so that the identified position can scale correctly. A single gradient characterised by a fixed decay length cannot achieve this. We therefore examine a system where protein gradients are produced by sources at both ends, and where the central position is identified as a concentration minimum.

We therefore modify our earlier model by adding an additional planar source at $x = L$. This addition is appropriate for modelling cell division inhibitors, such as MipZ in *Caulobacter*, that are injected into the membrane near both cell poles. However, our model would apply equally if the two sources are of different repressor proteins (as may be the case in fission yeast [48, 49]), although we do assume that J, D and μ are the same for both gradients. In this scenario, signalling activity will be determined by the total concentration. Without fluctuations, this will be described by

$$\frac{\partial \rho}{\partial t} = D\nabla^2\rho - \mu\rho + J\delta(x) + J\delta(x - L). \tag{3.39}$$

The steady-state solution is now

$$\rho(x) = \frac{J\lambda}{D}\frac{\cosh((x - L/2)/\lambda)}{\sinh(L/2\lambda)}, \tag{3.40}$$

which has the expected minimum at $x = L/2$.

We then suppose that the cell compares the concentration to a threshold value corresponding to the minimum of the average profile, $\rho_{min} = \rho(L/2) = \rho_T$. Positions where the concentration is at or below the threshold are identified as being at the centre of the cell. While the average steady-state density profile would never extend below ρ_{min}, fluctuations ensure that the concentration in the region around the centre spends a significant amount of time at or below the threshold. Around point(s) where $\langle\rho(x)\rangle = \rho_T$, noise in the protein concentration will lead to a distribution of

threshold crossing positions. We consider an expansion of the density fluctuations about $x_T = L/2$, giving, to leading order

$$\Delta\rho(x_T) = \frac{1}{2}\left|\langle\rho''(x_T)\rangle\right| w^2, \tag{3.41}$$

since any first order term proportional to $\langle\rho'\rangle$ vanishes at $x_T = L/2$. The width is therefore given by

$$w^2 = \frac{2\Delta\rho(L/2)}{\langle\rho''(L/2)\rangle}. \tag{3.42}$$

Substituting in (3.40) gives

$$w_0 = \left(\frac{4D\lambda^3 \sinh(L/2\lambda)}{J(\Delta x)^d}\right)^{1/4}. \tag{3.43}$$

As for a single gradient model, for systems in $d = 2$ or $d = 3$ dimensions, the typical occupancy of the threshold region will be much less than one. For example, if we take the parameter values considered previously for the Pom1p gradient in fission yeast, with 2000 protein copies, the average occupancy of a detector site at $x = L/2$ will be $\langle n(L/2)\rangle \sim 10^{-3}$. We assume here that Pom1p forms a gradient from both poles. In fact it may only form a single gradient with another hitherto unidentified protein forming the second polar gradient [48, 49]. However, as discussed earlier, this detail does not affect our calculations. As a second example, MipZ in *Caulobacter* ($L = 2.5\mu m$, $L_\perp = 2\mu m$) is typically present at about 1000 copies, and forms two polar gradients with a decay length $\lambda \approx 0.25\mu m$ [45]. The average occupancy at the centre of this system would be approximately $\langle n(L/2)\rangle \sim 10^{-3}$. Averaging measurements of the concentration over time is therefore required in both cases to obtain precise positional information. Since the width now goes as $(\Delta\rho)^{1/2}$, as shown in (3.42), we expect

$$\begin{aligned} w(\tau) &= w_0\left(\frac{\tau_{ind}}{\tau}\right)^{1/4} \\ &= \begin{cases} \tilde{k}_{2d}\left[\frac{\lambda^3}{\tau J}\sinh(L/2\lambda)\left(\ln\left(\frac{\lambda^2}{(\Delta x)^2}\right)+\tilde{\alpha}\right)\right]^{1/4} & \text{in } d=2 \\ \tilde{k}_{3d}\left[\frac{\lambda^3}{\tau J(\Delta x)}\sinh(L/2\lambda)\right]^{1/4} & \text{in } d=3 \end{cases}, \end{aligned} \tag{3.44}$$

where $\tilde{k}_{2d}$, $\tilde{\alpha}$ and $\tilde{k}_{3d}$ are constants. Averaging proceeds much more slowly than previously, with a $\tau^{-1/4}$ dependence. This follows directly from the vanishing of the first derivative at the average threshold position. In $d = 3$, and for $\lambda \ll L$, equation (3.44) predicts that w will be minimised when $\lambda \approx L/6$ is chosen. In $d = 2$ logarithmic corrections again alter this result slightly, with the optimal decay length now occurring at

$$\lambda \approx \frac{L}{6}\left(1 - \frac{1}{3\ln(L/6(\Delta x))}\right), \tag{3.45}$$

where we have included the leading logarithmic correction. This result arises for similar reasons as in the single gradient model. For the Pom1p gradient imaged by Padte et al [49], the decay length is observed to be $1 - 1.5\mu m$, comparable to this optimal decay length of about $1.5\mu m$ for a $10\mu m$ cell.

We simulated our model as described previously for the single gradient model in two dimensions with representative parameter values for fission yeast membrane gradients. In addition to the source at $x = 0$, particles were also added at $x = L$ in an identical but uncorrelated process. We used $\mu = 0.36s^{-1}$ chosen to give $\lambda = 1.67\mu m$, and $J = 6\mu m^{-1}s^{-1}$ giving on average 200 protein copies in total. Figure 3.5 shows the results of these simulations. Again we observe two distinct regimes. At averaging times longer than about a second, there is excellent agreement with equation (3.44), as we can see in figure 3.5**C**. Data are shown with $D = 0.5\mu\mathrm{m}^2s^{-1}$; $\mu = 1s^{-1}$; $\mu = 0.25s^{-1}$; $J = 9\mu\mathrm{m}^{-1}s^{-1}$; $\Delta x = 0.02\mu\mathrm{m}$; $L = 7.5\mu\mathrm{m}$; $L = 15\mu\mathrm{m}$ and $\Delta x = 0.02\mu\mathrm{m}$. Fitting to the simulation results we find $\tilde{k}_{2d} = 0.63 \pm 0.02$ and $\tilde{\alpha} = 2.5 \pm 1.0$. Figure 3.5**D** confirms the existence of the optimal decay length in our simulations. At short averaging times, the width tends to a constant value. This value can be estimated as in the single gradient model, by considering the probability distribution of particles,

$$p(x)dx = \frac{\cosh((x - L/2)/\lambda)}{2\lambda\sinh(L/2\lambda)}dx. \tag{3.46}$$

The symmetry of the system means that $\bar{x}$ will always fluctuate about $L/2$, as shown

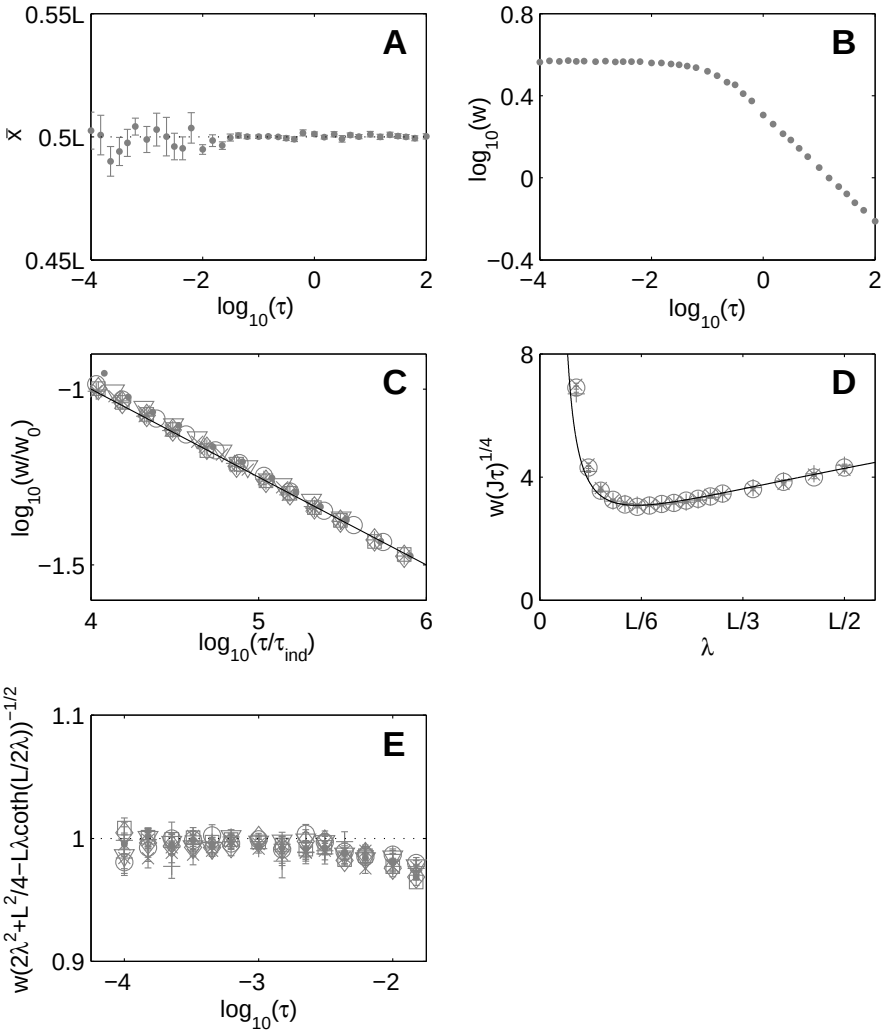

Figure 3.5: Two gradient model in $2d$. **A** The mean threshold position fluctuates about $L/2$ due to the symmetry of the system. **B** Variation of the width w as a function of averaging time. **C** Data collapse of the width as a function of averaging time, at long times, for a range of parameter values. The full line shows (3.44) with $\tilde{k}_{2d} = 0.63$ and $\tilde{\alpha} = 2.5$. $*$ indicates the standard parameter values. For the other data sets parameter values were changed as follows: $\circ$: $D = 0.5\mu\text{m}^2 s^{-1}$; $\square$: $J = 9\mu\text{m}^{-1}s^{-1}$; $\times$: $\Delta x = 0.02\mu\text{m}$; $\bullet$: $\mu = 1s^{-1}$; $+$: $\mu = 0.25s^{-1}$; $\diamond$: $L = 7.5\mu\text{m}$; $\triangledown$: $L = 15\mu\text{m}$ and $\Delta x = 0.02\mu\text{m}$. **D** Plot of width as a function of decay length for averaging times $\times$: $\tau = 30s$; $\circ$: $\tau = 45s$; and $+$: $\tau = 60s$. The full line shows the prediction from equation (3.44). **E** Scaling collapse of the width at short averaging times, given by (3.47). Parameter values are as in **C**.

in figure 3.5**A**. The width in this regime will be given by

$$w^2 = \int_0^L (x - L/2)^2 \, p(x) dx = 2\lambda^2 + \frac{L^2}{4} - \lambda L \coth(L/2\lambda), \tag{3.47}$$

which is also reproduced in simulations (figure 3.5**E**).

Since the width decays as $\tau^{-1/4}$ for this system, longer averaging times and/or higher protein copy numbers are required than in the single gradient model to achieve high precision. Intrinsic biochemical noise may therefore strongly constrain systems of this type. In order for the yeast-membrane gradient considered above to achieve precision of $\pm 5\%$ of the cell length after averaging for one minute, about 800 protein copies are required. Therefore, in the absence of any other positioning mechanisms, the Pom1p gradient will require ~ 1000 protein copies or more to precisely direct the location of cell division. We estimate that the MipZ gradient in *Caulobacter*, with 1000 protein copies, would be able to locate the cell centre to within $\pm 5\%$ of L after approximately $\tau = 2s$. However, since precision only improves as $\tau^{-1/4}$, averaging over $\tau = 20$ minutes would be required for the same system to achieve $\pm 1\%$ accuracy.

Similar results are also observed in one dimension. The time-averaged width is given by

$$w(\tau) = \tilde{k}_{1d} \left(\frac{4\lambda^4 \sinh(L/2\lambda)}{J\tau} \right)^{1/4}, \tag{3.48}$$

which is again independent of Δx, and leads to an optimal length scale $\lambda \approx L/8$. Note that the source of the $\tau^{-1/4}$ scaling in (3.48) is different from that in (3.29). By analogy with (3.29), a regime in which $w \sim \tau^{-1/8}$ is also possible for two oppositely directed gradients in one dimension.

3.2.5 Discussion

Noise in biochemical processes within a cell will lead to fluctuations in protein concentration gradients, and hence also to variation in the position where these gradients cross a particular threshold value. These fluctuations therefore place a limit on the potential precision of position determination mechanisms relying on concentration gradients alone. In subcellular systems with protein copy numbers in the thousands,

this noise will be sufficiently large that position cannot be determined reliably from a single measurement of the density profile. In order to determine position to within a few percent, a precision achieved by some subcellular systems, the protein concentration must be averaged over time. For a single subcellular membrane gradient, we have seen that by averaging over a period of a minute, excellent precision can potentially be achieved with only a few hundred protein copies. This remarkable precision is due to the sub-millisecond diffusive time-scale on which time-averaging occurs. Precise identification of the cell mid-plane by gradients emanating from both poles requires longer averaging times or higher copy numbers, since larger fluctuations result from the vanishing first derivative of the average concentration at the system centre. Intrinsic biochemical noise may therefore be a strong constraint on subcellular two-gradient positioning systems, dictating that the copy numbers be sufficiently high to suppress fluctuations.

So far we have focused almost exclusively on fluctuations in subcellular gradients, however our results are also applicable to developmental biology. Here the appropriate length scales are usually much longer, on the order of hundreds of micrometers in *Drosophila*. Moreover, the gradients affect patterns of gene expression through the binding of gradient molecules to DNA regulatory sequences inside individual nuclei. For example Bicoid, for which exponential gradients have been quantitatively measured in *Drosophila* [115], is thought to bind cooperatively to *hunchback* regulatory DNA. In this case we again expect molecular-scale effective measuring volumes, with $\Delta x \sim 0.01\mu$m being a reasonable order of magnitude. We next assume purely Poisson statistics for the fluctuations: this is a stronger assumption than for our earlier subcellular gradients, as there will be additional complications arising, for example, from the import/export of morphogens from nuclear compartments. However, if diffusive noise is dominant then Poisson statistics will be retained and we can expect our earlier analysis to apply, although with one important distinction. Instead of Δx setting the maximal possible precision, this will now be set by the size of individual nuclei (prior to cellularisation), since we expect relatively homogeneous gene expression within a single nuclear volume. A single nucleus in *Drosophila* has a length scale of around 10μm, still much smaller than the decay length of the gradient of $\lambda \sim 100\mu$m, al-

lowing for high precision gene expression [115]. Using the *Drosophila* Bicoid gradient as an example, we use $L = 500\mu$m, $L_\perp = 100\mu$m, and estimate $D = 10\mu\text{m}^2 s^{-1}$ and $\mu = 10^{-3} s^{-1}$, giving $\lambda = 100\mu$m, consistent with experiment [115]. Assuming a high copy number of 10^7 per embryo (we are not aware of experimental constraints on this figure), gives $J \sim 1\mu\text{m}^{-2} s^{-1}$. For a single gradient in three dimensions, we find that about a 5 minute averaging time is required to bring the error down to plus or minus a single nuclear length. For a two gradient model in three dimensions, longer averaging times on the order of an hour are required to reduce the centre-finding positional error to plus or minus about 2 nuclear lengths. Since gene expression may need to be controlled on shorter timescales than this, other designs, for example using *interacting* gradients [67, 68], may be required for high precision centre finding (see also below). The effects of the optimum gradient length scale will also be interesting to probe in a developmental biology context. However, our simple analysis may be complicated by the multiple roles played by many morphogens: for example, Bicoid not only activates *hunchback*, but it also helps to regulate pair-rule genes, such as Even-skipped. Nevertheless, it is interesting to note that the Bicoid gradient length scale $\lambda \sim 100\mu$m [115] is not too far away from the $L/6$ optimum for a two gradient case, and in a single gradient context will offer maximal precision well into the anterior half of the embryo.

Up to this point we have only considered systems with first order degradation. Morphogen gradients with nonlinear decay have also been proposed [66]. This nonlinearity will lead to non-Poissonian density fluctuations, which may significantly change the observed behaviour. England and Cardy [124] have previously calculated the response of a gradient with nonlinear decay to one source of biochemical noise, namely a fluctuating production rate. However, they calculated the change to the average gradient, while fluctuations about this average may also be important. It would certainly be of interest to compare the performance of linear and nonlinear degradation mechanisms in more detail.

Throughout this analysis we have assumed that the gradient protein concentration fluctuates about a steady-state profile, and hence averaging over a longer time will give a more precise estimate of the average profile. For a subcellular system, the

steady-state gradient will develop over timescales of less than about a minute, due to the micrometer length scales involved. This timescale is short compared to the cell cycle time, which ranges from tens of minutes up to many hours. For this reason we expect that subcellular gradients will be in steady-state and therefore that our analysis will be directly applicable. However, in developmental biology, the effective lifetimes will likely be much longer, and the gradient may take hours to fully reach steady-state. Moreover, a number of developmental biology systems are known to respond to a morphogen gradient that has not reached steady-state [125-127]. A further complication is the possibility of gradient formation by non-Fickian diffusion [128], where there is no steady-state at all. The model considered above does not take into account time-varying average gradients. If the average gradient is evolving, a longer averaging period will not necessarily lead to improved precision. Clearly, more work will be required to understand how such dynamically evolving systems are able to yield precise positional information and filter out fluctuations. Nevertheless, we do note that two gradient systems of the kind analysed here are naturally able to locate the system centre even without being in steady-state, due to the symmetry of the system [67]. The positional variations in such a non-steady-state scenario will not be the same as calculated here, but our analysis does form a first step towards the analysis of these more complex systems.

3.3 Two interacting gradients

Centre-finding mechanisms with interactions have also been proposed [67, 68]. We now consider the case where two morphogens, A and B, are produced at opposite poles, and interact to inactivate one another. The concentration profile will now consist of oppositely directed gradients with a reaction front where the two gradients meet. The effective gradient will be steep around the system centre due to the interaction between the two gradients. These mechanisms may therefore be able to achieve greater precision for mid-point determination than the noninteracting mechanism considered above.

For convenience we define the system in one dimension on the domain $-L/2 \leq$

$x \leq L/2$. Protein A is produced at rate J at $x = -L/2$. Protein B is produced at the same rate at $x = L/2$. The diffusion constants and degradation rates, D and μ respectively, for the two proteins are taken to be the same. The dynamic equations for the densities of A and B in the absence of noise are

$$\frac{\partial \rho_A}{\partial t} = D\nabla^2 \rho_A - \mu \rho_A - \nu \rho_A \rho_B \tag{3.49}$$

$$\frac{\partial \rho_B}{\partial t} = D\nabla^2 \rho_B - \mu \rho_B - \nu \rho_A \rho_B. \tag{3.50}$$

The chemical system $A + B \rightarrow \emptyset$, which is equivalent to this gradient model but with $\mu = 0$, has been studied extensively [129-133]. By analogy with this system, we can identify two components which affect the positional precision of this model. First, there will generally be a range over which there is a significant concentration of both A and B as the proteins diffuse around one another without reactions. The reaction front will have the approximate form $R(x) \approx \rho_A(x)\rho_B(x)$. For small reaction rates this component will dominate the uncertainty in position, and the front will have the mean-field width as reported by McHale et al [68], $w \sim (D^2/J_r\nu)^{1/3}$, where J_r is the flux of particles into the reaction region. The second contribution to positional uncertainty comes from fluctuations in the position, or "wandering", of the centre of the reaction front. This effect will dominate when the reaction rate is sufficiently large that the densities of A and B near the reaction front are low. In this case there will be a single well defined position at which reactions occur at a particular time, but this will move due to diffusion of particles. Some biological systems, where the particle flux is relatively small but the reactions between proteins are fast, may be in this regime. We will therefore estimate the positional uncertainty due to wandering of the reaction front by considering the large reaction rate limit.

To calculate the width of the distribution of front positions associated with this wandering, we follow the approach of Barkema et al [133]. It is convenient to consider an effective difference field, ψ, which is defined in a quantum field theory for this model [132]. ψ is on average the same as $\langle \rho_A \rangle - \langle \rho_B \rangle$, although importantly the fluctuations

in ψ are not the same as those in $\rho_A - \rho_B$. From the field theory, ψ follows

$$\frac{\partial \psi}{\partial t} = D\frac{\partial^2 \psi}{\partial x^2} - \mu\psi + \eta(x,t). \tag{3.51}$$

The term $\eta(x,t)$ represents the reaction noise, and satisfies

$$\langle \eta \rangle = 0, \quad \langle \eta(x,t)\eta(x',t') \rangle = 2\delta(x-x')\delta(t-t')R(x). \tag{3.52}$$

where $R(x)$ is the reaction front profile. The steady state solution to (3.51) with appropriate boundary conditions is

$$\psi_0(x) = -\frac{J_0\lambda}{D}\sinh(x/\lambda). \tag{3.53}$$

where $J_0 = J/\cosh(L/2\lambda)$. Now we expand ψ in terms of the mean field solution, ψ_0, plus a Fourier series expansion which represents the effects of the reaction noise on the density. Modes which couple most strongly to the reaction noise will be large at $x = 0$. Far from the reaction front, ψ should follow the mean-field solution and there should be no additional contributions from noise at the reaction front. We therefore retain only Fourier modes which are maximal at $x = 0$, and which vanish at $x = \pm L/2$:

$$\psi = \psi_0 + \sum_{n=0}^{\infty} \chi_n(t)\cos\left(\frac{(2n+1)\pi x}{L}\right). \tag{3.54}$$

Since we are considering the limit of fast annihilation reactions, A and B proteins cannot simultaneously be present at the same location without reacting. The reaction front is therefore localised to a single position, $R(x) \approx J_0\delta(x)$. Substituting into (3.51) we find

$$\chi_n(t) = \frac{2\sqrt{2J_0}}{L}\int_0^t d\tau\xi(\tau)\exp\left[\left(\frac{(2n+1)^2\pi^2 D}{L^2} + \mu\right)(\tau - t)\right], \tag{3.55}$$

with

$$\langle \xi \rangle = 0, \quad \langle \xi(t)\xi(t') \rangle = \delta(t-t'). \tag{3.56}$$

In the long-time limit, the fluctuations in ψ are given by

$$\left\langle \psi(0,t)^2 \right\rangle - \left\langle \psi(0,t) \right\rangle^2 = \frac{8J_0}{\pi^2 D} \sum_{m=0}^{\infty} \sum_{n=0}^{\infty} \frac{1}{(2m+1)^2 + (2n+1)^2 + \frac{2L^2}{\pi^2 \lambda^2}}. \tag{3.57}$$

This sum is divergent due to contributions from terms with large m and n. The L/λ term is constant, and hence can be neglected when these large m and n terms dominate. We can find an approximate solution by truncating the sum at some large $n, m \sim K$. This cutoff K takes the value cL/w_i, where w_i is the reaction front width due to wandering, and c is a dimensionless fitting parameter. By truncating the right hand side of (3.57) in this way we are neglecting Fourier modes with wavelength shorter than w_i. Fluctuations on such short length scales are contained entirely within the reaction front, and hence do not contribute to the front width. The resulting variance in ψ is

$$(\Delta\psi)^2 = \left\langle \psi(0,t)^2 \right\rangle - \left\langle \psi(0,t) \right\rangle^2 \sim \frac{J_0}{\pi D} \ln(cL/w_i). \tag{3.58}$$

Finally as before we can using a first order expansion to estimate w_i,

$$w_i = \frac{\Delta\psi}{|\psi'(L/2)|}, \tag{3.59}$$

which is now given by the solution to

$$w_i^2 = \frac{D}{\pi J_0} \ln\left(\frac{cL}{w_i}\right). \tag{3.60}$$

Simulations of this system were performed in the infinite reaction rate limit. If A and B particles occupy the same position after any time increment, an equal number of each are removed until only one species is present at each site. The distribution of these reaction events by position determines the front profile. Figure 3.6 shows these distributions as a function of x/w_i. We can see that the front position has an approximately Gaussian distribution with width given by equation (3.60). The above result reproduces the observed width well for parameter values which give $\lambda \lesssim L/4$ and $w_i \lesssim \lambda/4$. If w becomes comparable to λ, the approximation that the ψ profile

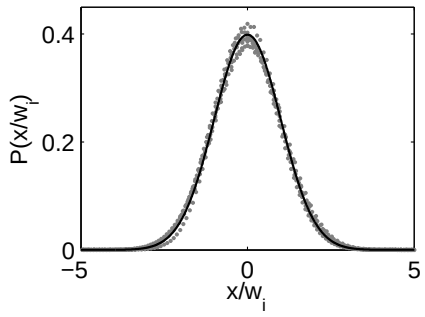

Figure 3.6: Probability distribution of position of reaction front. The solid line shows a normal distribution. Standard parameter values are: $L = 10\mu m, \Delta x = 0.01\mu m, D = 1\mu m^2 s^{-1}, \lambda = 1\mu m, J = 1000 s^{-1}$. These parameters were varied by setting $L = 7.5\mu m$; $D = 0.5\mu m^2 s^{-1}$; $\lambda = 0.5\mu m$; $J = 2000 s^{-1}$; $J = 750 s^{-1}$.

is linear near the front position, which is implicit in (3.59), is no longer valid. If λ becomes too large relative to the system size, the front is able to wander away from $x = 0$. In the case of $\mu = 0$ the reaction front is not constrained to lie near the centre of the system, since any linear profile with $\frac{d\psi_0}{dx} = -J/D$ is a valid solution to (3.51). The addition of degradation provides an effective restoring force which acts to localise the front to $x = 0$. However, for large λ this effect is weak, and our assumption that the front $R(x) \sim \delta(x)$ is located at $x = 0$ breaks down.

In general, for equivalent parameter values, w_i is smaller than the width we would expect in an equivalent non-interacting system. For the parameter values used in figure 3.6, we find $w_i \sim 0.26\mu m$. For two non-interacing gradients we would have $w_0 \sim 0.43\mu m$. Note that due to the mutual degradation of proteins, the copy number in the interacting system will be much lower than in the non-interacting system. We might expect this reduction in copy number to increase density fluctuations. In contrast to the non-interacting system, where the midpoint is marked by a minimum of the concentration profile, in this case the effective concentration profile $\langle \psi(x) \rangle$ is steep near the interface. The system is therefore still able to resolve position accurately. This example is biologically somewhat unrealistic because the system under consideration is one-dimensional, and the production rates are very large. Nevertheless, by introducing reactions between the two gradients, the precision of the system can potentially be increased.

Chapter 4

Establishment of Embryonic Polarity in *C. elegans*

4.1 Introduction

Experimental screens for defects in asymmetric divisions and division timing in the early *C. elegans* embryo identified a group of seven PAR proteins, along with a number of other factors such myosin, its regulators, and several cytoplasmic proteins [100, 134, 135], which are required for correct cell polarity. In *C. elegans* the PAR proteins consist of PAR-1 through PAR-6, plus PKC-3. The PAR proteins are largely conserved in other organisms, such as *Drosophila* and mammals, and have been found to regulate cell polarity in diverse cell types, including epithelial cells and neuroblasts [90-92]. PAR-3, PAR-6 and the atypical protein kinase C PKC-3 form a conserved group which frequently associate with the cortical cytoskeleton and with CDC-42 [90, 92, 95]. PAR-1 and PAR-4 are conserved kinases, although their substrates are not known. PAR-5 is a 14-3-3 protein; these typically contain multiple binding sites for other phosphorylated proteins. The RING-finger protein PAR-2 is the only *C. elegans* PAR protein which is not found in other organisms.

The polarity establishment process is summarised in figure 4.1**A** [104, 105, 107]. Initially the PAR proteins and cortical actomyosin are uniformly present throughout the embryo. Fertilisation by the sperm causes actomyosin to contract towards the

anterior pole. PAR-3, PAR-6 and PKC-3 (the anterior PAR proteins) are restricted to this shrinking anterior domain. PAR-1 and PAR-2 (the posterior PAR proteins) accumulate in this newly vacated posterior cortical region. Here we present a mathematical model of this polarity establishment process.

The PAR protein interactions and random diffusive motion can be readily described by a system of nonlinear reaction-diffusion equations. However, the distributions of the PAR proteins are also influenced by the dynamics of the cortical actomyosin network, with increased anterior PAR protein binding to regions with enhanced actomyosin concentrations. The dynamics and regulation of the actomyosin network is highly complex, potentially involving actin polymerisation, myosin motor activity, cross-linking proteins and interaction with the cell membrane. Many of these effects and interactions are not well understood. We therefore construct a highly simplified model of actomyosin contraction that reproduces the experimental results on cellular length scales, while neglecting smaller-scale details that do not significantly affect the global protein distributions. We couple this description to our reaction-diffusion model, thereby enabling us to calculate the contractile actomyosin density and PAR protein distributions.

Initially, we develop a simple model that includes only the previously reported interactions between the PAR proteins together with diffusion and actomyosin contraction. We find that these interactions allow us to reproduce many features of the PAR system that are observed *in vivo*, including the polar cortical domains and the cortical dynamics in *par* mutant phenotypes. However, this model is unable to correctly reproduce the polarised distributions of the PAR proteins in the cytoplasm and the resulting polarity of cytoplasmic components such as MEX-5/6 [104], which are vital for the different development of the two daughter cells. We consider a number of ways in which the model can be modified to better capture the observed cytoplasmic polarity. We also suggest experiments that can test these possible mechanisms. Finally we also predict that, while contraction of the actomyosin network is crucial for the establishment of polarity, the motion of PAR proteins in the resulting cortical and cytoplasmic flows is of lesser significance, provided cytoplasmic diffusion is sufficiently fast.

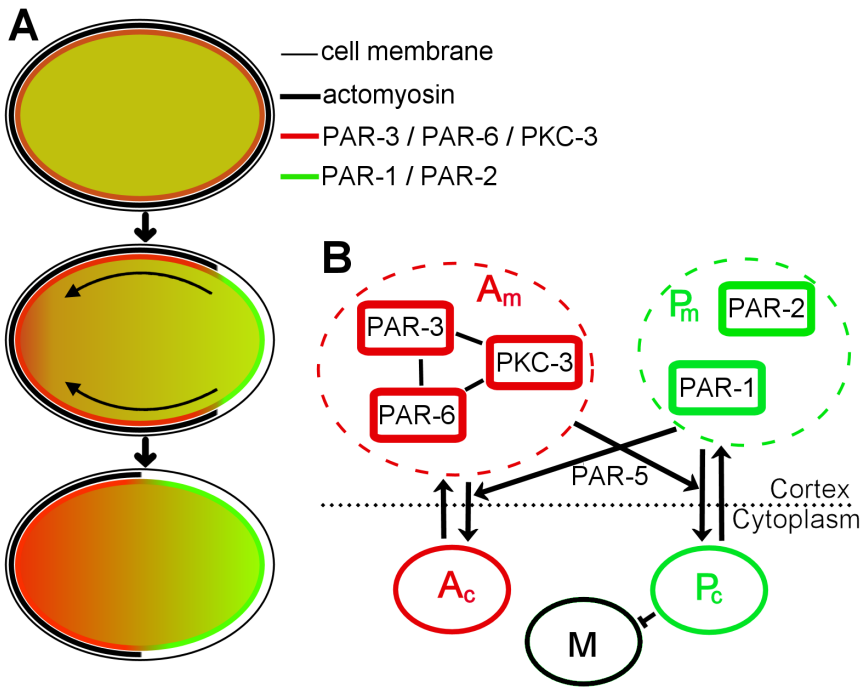

Figure 4.1: **A** Summary of PAR dynamics in wild-type embryos. Shown are the PAR distributions before, during, and after actomyosin contraction. Arrows indicate the direction of cortical actomyosin flow. The anterior pole is to the left. **B** Summary of the reaction scheme for the basic model in equations (4.1-4.4) and (4.9). For clarity, actomyosin and the spatial aspects of the model are not shown.

4.2 An initial model of the PAR system

4.2.1 PAR interactions

We first construct a mathematical model of the previously reported interactions between the PAR proteins. To simplify our model somewhat we separate the PAR proteins into anterior and posterior groups, as PAR protein types within each group are normally colocalised within the embryo [136-138]. The variable A will represent the densities of the anterior PAR proteins PAR-3, PAR-6 and PKC-3, that have been suggested to form a complex [137, 138]. We will let P represent the densities of the posterior PAR proteins PAR-1 and PAR-2, although it is not known whether PAR-1 and PAR-2 interact directly. The PAR proteins can be cortically-localised (A_m, P_m) or in the cytoplasm (A_c, P_c). Reactions between proteins within each group tend to

promote association - all of the anterior proteins are required for the cortical localisation of PAR-6 and PKC-3 [104, 137, 138], and PAR-2 may enhance the cortical localisation of PAR-1 [136]. Interactions between the two groups tend to be antagonistic, and mutual negative feedback from the localisation of each group onto the other has been proposed to explain in part the segregation of the PAR proteins into anterior and posterior domains [104]. The shared properties of association/antagonism by members of each group make it advantageous to model the PAR system at the level of the anterior/posterior protein groups, rather than modelling each protein type separately. A model of the latter type would be significantly more complex, but with little additional predictive advantage.

Crucial to the polarity establishment process is rearrangement and contraction of the cortical actomyosin network towards the anterior pole [107]. The density of this contractile actomyosin domain is represented in our model by a. Levels of actomyosin that remain at the posterior cortex are much lower than those at the anterior [107, 139] and cortical ruffling is eliminated at the posterior, suggesting that the observed global contraction is largely driven by the anterior domain. Consequently, we do not include this posterior actin domain in the model. Since the embryo is polarised only along the anterior-posterior axis, we restrict the model to one dimension.

Both the anterior and posterior PAR proteins dynamically associate with the cortex [105]. We will assume that this cortical dynamics is the result of both diffusion of cortical proteins and exchange of proteins between the cortex and cytoplasm. We further assume that the anterior PAR proteins associate at an increased rate with the contractile actomyosin region, consistent with the observation that during polarity establishment in posterior *par* mutants, the anterior PAR proteins are restricted to the anterior cortex [104]. It is not known whether the anterior PAR proteins associate directly with the actomyosin cytoskeleton itself. The cortical localisation patterns of myosin and PAR-6 are slightly different but highly correlated [107]. This enhanced association may be due to the presence of CDC-42, which is required for maximal cortical localisation of the anterior PAR proteins [140, 141], or some other difference between the cortical actomyosin in the anterior and posterior domains. In addition to spontaneous dissociation, PKC-3 phosphorylates PAR-2 [142] and we assume this

promotes removal of the posterior PAR proteins from the cortex. We also allow PAR-1 to stimulate dissociation of the anterior PAR proteins from the cortex, possibly through phosphorylation of PAR-3. Evidence for this reaction has been found in PAR homologues in other species [143], and a similar process has been proposed to occur in *C. elegans* [142]. In this way, cortical localisation of one group acts to exclude the other, and hence provides an effective positive feedback to its own accumulation. The cortical exclusion reactions likely require the 14-3-3 protein PAR-5 [104]. We do not model PAR-5 explicitly since it is uniformly localised throughout the cortex and cytoplasm [144]. We also do not include PAR-4, since its interactions with other PAR proteins and its effect on their distributions is not known.

Figure 4.1**B** summarises the interaction network. Our model consists of reaction-diffusion equations for the PAR protein interactions. The PAR proteins are also coupled to a simple model of cortical actomyosin contraction by incorporating enhanced cortical binding of the anterior PAR proteins in the presence of contractile actomyosin. The resulting equations are

$$\frac{\partial A_m}{\partial t} = D_m \nabla^2 A_m + (c_{A1} + c_{A2} a) A_c - c_{A3} A_m - c_{A4} A_m P_m \tag{4.1}$$

$$\frac{\partial A_c}{\partial t} = D_c \nabla^2 A_c - (c_{A1} + c_{A2} a) A_c + c_{A3} A_m + c_{A4} A_m P_m \tag{4.2}$$

$$\frac{\partial P_m}{\partial t} = D_m \nabla^2 P_m + c_{P1} P_c - c_{P3} P_m - c_{P4} A_m P_m \tag{4.3}$$

$$\frac{\partial P_c}{\partial t} = D_c \nabla^2 P_c - c_{P1} P_c + c_{P3} P_m + c_{P4} A_m P_m \tag{4.4}$$

The first term on the right hand side of (4.1-4.4) represents undirected protein diffusion. The remaining terms describe the various reactions in the model. $(c_{A1} + c_{A2} a) A_c$ represents cortical association of the anterior PAR proteins, which is enhanced in the presence of contractile actomyosin. The density of actomyosin, a, is calculated from our actomyosin model, as described in the next section. Similarly, P_c associates with the cortex through the $c_{P1} P_c$ term. $c_{A3} A_m$ and $c_{P3} P_m$ give spontaneous dissociation of the anterior and posterior PAR proteins. The terms $c_{A4} A_m P_m$ and $c_{P4} A_m P_m$ represent competitive exclusion of the cortical A and P groups. Since these binding and dissociation terms represent exchange between the cytoplasm and cortex, they appear

in the equations for both cortical and cytoplasmic densities with opposite signs. Note that the above model does not incorporate production or degradation of the PAR proteins.

4.2.2 Modelling actomyosin contraction

In the model described above, actomyosin dynamics feeds back onto the PAR distributions through the varying density of contractile actomyosin. As the anterior actomyosin network contracts its density increases, leading to enhanced binding of the anterior PAR proteins. In order to quantify this effect, we now need to construct a simplified model of the actomyosin activity. Such a model will enable us to calculate the density of actomyosin in the contractile region, while neglecting detailed actomyosin dynamics which do not affect the PAR distributions on a cellular scale. We emphasise that the polarisation of the actomyosin cytoskeleton is crucial in our model in order to break the symmetry of the system. If the actomyosin dynamics are removed, no spatial variation in the PAR protein densities can develop.

We assume that the actomyosin network is initially under tension. A polarization cue from the sperm [103, 145] is believed to cause a down-regulation of the actomyosin network near the posterior pole. While it is possible that the polarity signal also affects the PAR proteins directly, this effect is not necessary in our model for polarity establishment. Once the symmetry of the network has been broken in this way, the remaining network is unstable and contracts towards the anterior. We therefore choose to model the effective dynamics of the actomyosin network as an elastic medium. The convergent flows of myosin observed in kymographs are consistent with such a global contraction model [107]. To introduce positive feedback from the anterior PAR proteins onto contractility [107], we will allow the elastic properties of the system to vary depending on A_m. We simplify the elastic model further by assuming that, rather than A_m altering the local elastic properties, the properties of the actomyosin network as a whole depend only on the total amount of A_m in the contractile region, and that the actomyosin network contracts uniformly. This is a reasonable assumption, since, in our simulations, the density of A_m in the anterior contractile domain is relatively

constant, varying by only up to 20% from the average in this region. However, in reality, actomyosin contraction is non-uniform on short length scales, giving rise to dynamic features such as cortical ruffling and pseudocleavage. Nevertheless, we find that our coarse-grained model gives good agreement with measurements of the cortical dynamics over cellular length scales. The assumption of homogeneity also makes the model much simpler to analyse and allows us to easily compute the contraction dynamics. Relaxing this assumption would require significantly more complex model while not giving qualitatively different behaviour at a cellular scale.

The resulting dynamical equations are simply those of a uniform spring. In the subcellular environment viscous forces dominate over inertial forces. The motion of the spring will therefore be overdamped, and we neglect the second-order term in the equation of motion. In this limit of large damping, the dynamics of the spring are determined by four physical quantities: the Young's modulus, E, which is the ratio of the applied stress to the resulting strain; the cross-sectional area, $\tilde{A}$; the damping coefficient, γ, which determines the rate of energy dissipation; and the natural length, Λ, the length of the spring when no force is applied. Assuming that $\tilde{A}$ and γ are constant as the spring expands and contracts the length of the spring, $l(t)$, will be given by

$$\frac{dl}{dt} = v_l(t) = -\frac{\epsilon}{\Lambda}\left(l(t) - \Lambda\right) \tag{4.5}$$

where $\epsilon = E\tilde{A}/\gamma$. Clearly assuming a constant $\tilde{A}$ is a crude approximation for the actomyosin network, an approximation that will become less accurate close to the embryo poles. Nevertheless, our model captures the essence of the contraction process at the cellular scale and agrees well with the experimentally observed actomyosin dynamics.

During contraction, the density of a simple spring remains uniform along the spring's length. In modelling the cortical actomyosin network in this way, we therefore require that the density of contractile actomyosin is uniform across the contractile domain of length $l(t)$,

$$a(x,t) = \begin{cases} a_0 \frac{L}{l(t)} & 0 \leq x \leq l(t) \\ 0 & l(t) < x \leq L \end{cases} \tag{4.6}$$

where a_0 is the actomyosin density at $t = 0$. Beyond the end of this domain we assume that there is no contractile actomyosin present, i.e. $a = 0$. Initially, the contractile actomyosin network occupies the entire cortex, i.e. $l(0) = L$. The position of the posterior end of the contractile actomyosin domain at a later time is calculated from (4.5).

The presence of the anterior PAR proteins appears to enhance actomyosin contractility through an unknown mechanism [107]. From (4.5) we see that this could take place through two effects. First, increased A_m may allow the actomyosin network to contract to a shorter final length, acting to reduce Λ. This effect is essential to achieve the different sizes of anterior domains that are seen in different mutants. Secondly, A_m may act to change ϵ, altering the stiffness of the actomyosin network for a fixed natural length. In our model, the best agreement with experiment (with the exception of MEX-5/6 mutants, as discussed below) is achieved when ϵ remains constant, and where the effect of A_m is to vary only the natural length, according to

$$\Lambda(t) = \Lambda_0 + \Lambda_1 m(t) \tag{4.7}$$

with $m(t)$ representing the contractile activity stimulated by the anterior PAR proteins. As discussed above, we take $m(t)$ to depend on the total amount of A_m in the contractile region, given by

$$m(t) = \frac{1}{L}\int_0^{l(t)} A_m dx \tag{4.8}$$

The assumption of linearity in equation (4.7) is not specifically required to reproduce the correct dynamics. With a suitable rescaling of Λ_1 and the introduction of saturation of $m(t)$ (i.e. $m(t)$ tends to a constant) when A_m is large, quadratic or higher functions can be used with similar results.

With this model the magnitude of the local velocity at a given time, determined by the spring dynamics, is zero at the anterior pole and increases linearly towards the posterior until the end of the anterior actomyosin domain. The rate of contraction slows as a spring approaches its natural length, so the speed of the posterior end of

the actomyosin region decreases over time. Both these properties appear consistent with experimental observations of the cortical actomyosin contraction pattern [107].

The similar and partially redundant CCCH finger proteins MEX-5 and MEX-6 are an important part of the signalling pathway that links PAR polarity to asymmetric gene expression [100]. Surprisingly, the cytoplasmic MEX-5/6 proteins, which become polarised in response to PAR polarity, were also found to affect polarity establishment [104, 105]. Disrupting MEX-5/6 reduces the size and rate of expansion of the posterior PAR-2 domain. MEX-5/6 have been implicated in controlling protein degradation [146], and other finger motif proteins are thought to regulate RNA levels or translation rates [100, 147-150]. It is therefore possible that MEX-5/6 affect actomyosin dynamics indirectly by regulating the levels of other factors that interact with the cytoskeleton. Consistent with this mechanism, the reduced rates of contraction in cells depleted of MEX-5/6 could be achieved in our actomyosin model by reducing the parameter ϵ.

Note that our simple model does not include actin polymerisation or depolymerisation reactions. While these processes may play a role in actomyosin reorganisation, the defects observed in *nmy-2* depleted cells [104, 135] suggest that the observed PAR dynamics is largely due to myosin-driven contraction. It is however possible that the actin turnover rate dictates the spontaneous dissociation rate of the anterior PAR proteins (although it is not clear whether the anterior PAR proteins actually associate directly with the actin cytoskeleton). It appears unlikely that such a mechanism operates for the posterior PAR proteins, which are localised in regions of lower actin density.

4.2.3 Simulations

Since *in vivo* concentrations of the PAR proteins are not known, we model concentrations in arbitrary units of protein numbers per unit length, chosen such that the densities in the are scaled to around $1\mu m^{-1}$. Simulations of equations (4.1-4.4) were initialised with uniform concentrations $a = 1\mu m^{-1}$, $A_c = 0\mu m^{-1}$, $A_m = 1\mu m^{-1}$, $P_c = 1\mu m^{-1}$, $P_m = 0\mu m^{-1}$. The dynamic equations for the anterior and posterior PAR proteins were integrated numerically on a lattice with spacing $\delta x = 0.2\mu m$ and

with a fixed time interval of $\delta t = 10^{-3}s$. Smaller values were also tested and found not to alter the behaviour of the system, showing that any numerical instability was not significant. Simulations were run for 10 minutes with $v_l(t)$ set to zero, to allow the system to reach steady-state. This point is marked as $t = 0$ in figures. The $t = 0$ state in the wild-type simulations is $A_c \approx 0.4\mu m^{-1}$, $A_m \approx 0.6\mu m^{-1}$, $P_c \approx 0.6\mu m^{-1}$, $P_m \approx 0.4\mu m^{-1}$. The $t = 0$ densities are different in the various mutant simulations, depending on the particular change to the dynamic equations. In each case there exists only one physical steady-state, so the choice of initial conditions is not significant.

Actomyosin contraction was initiated $t = 0$. At each subsequent time step the contractile actomyosin activity, $m(t)$, and natural length, $\Lambda(t)$, were calculated from equations (4.8) and (4.7) respectively. These values were then used in equations (4.5) and (4.6) to find $v_l(t)$ and the updated $l(t)$ and actomyosin density. The reaction and diffusion terms were calculated with an explicit discretisation scheme.

Parameter values were constrained to fit the dynamics observed in FRAP experiments [105]. Otherwise, different parameter combinations were tested manually and selected by inspection to best match the wild-type and mutant behaviour. The qualitative model behaviour in wild-type simulations was robust to at least a 50% change in each reaction parameter individually. Parameters for the actomyosin network were selected to match the three cases of wild-type, *par-1* and *par-3* mutants. The following parameter values were used: $L = 50\mu m$, $a_0 = 1\mu m^{-1}$, $\Lambda_0 = 42.5\mu m$, $\Lambda_1 = 27\mu m^2$, $\epsilon = 0.4\mu m s^{-1}$, $D_m = 0.25\mu m^2 s^{-1}$, $D_c = 5\mu m^2 s^{-1}$, $c_{A1} = 0.01s^{-1}$, $c_{A2} = 0.07\mu m s^{-1}$, $c_{A3} = 0.01s^{-1}$, $c_{A4} = 0.11\mu m s^{-1}$, $c_{P1} = 0.08s^{-1}$, $c_{P3} = 0.04s^{-1}$, $c_{P4} = 0.13\mu m s^{-1}$.

4.2.4 Wild-type dynamics

Figure 4.2 shows simulation results for the model described above as kymographs for the cortical density of actomyosin together with the cortical and cytoplasmic densities of the anterior and posterior PAR proteins. Initially, both anterior and posterior PAR proteins are present in the cytoplasm and at the cortex and are uniformly distributed along the cell length, as seen in experiment [104]. Levels of A_m and P_c are slightly

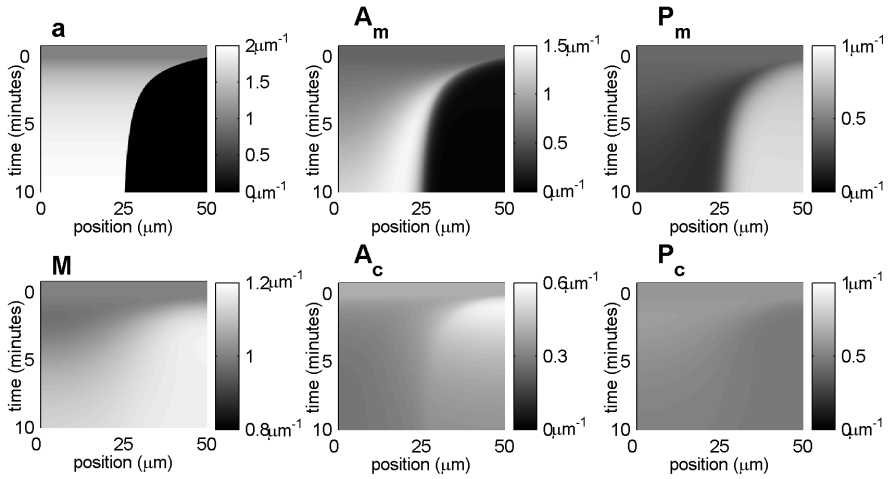

Figure 4.2: Wild-type simulation results for the model given by equations (4.1-4.4) and (4.9). Kymographs showing the densities of: a, contractile actomyosin; A_m, cortically-localised anterior PAR proteins; P_m, cortically-localised posterior PAR proteins; A_c, anterior PAR proteins in the cytoplasm; P_c, posterior PAR proteins in the cytoplasm; and M, cytoplasmic MEX-5/6. The time marked as zero indicates the initiation time of actomyosin contraction. The greyscale is shown for each panel. Densities are presented in arbitrary units of μm^{-1}.

higher than A_c and P_m respectively. In our model, actomyosin contraction generates an anterior region where binding of the anterior PAR protein is enhanced, and leaves a posterior region where cortical association of the anterior PAR proteins is greatly reduced. This eases the dissociation of the posterior PAR proteins at the posterior of the embryo, and hence the posterior PAR proteins become associated with the cortex at high levels here. The competition between the anterior and posterior PAR proteins means that each group excludes the other, thereby creating positive feedback allowing the density of whichever group is in the majority to increase. These reactions therefore give rise to the stably-polarised cortical distributions of the PAR proteins. Actomyosin contraction continues until ultimately the contractile domain is restricted to the anterior half of the embryo. Rapid initial contraction means that actomyosin quickly retracts to about 60% of the cell length within 3 to 4 minutes. The time to fully contract to mid-cell is approximately 8 minutes in our simulations, consistent with the time for which cortical and cytoplasmic flows are observed in vivo [105]. The resulting cortical distributions show good agreement with experiment [104]. The

maximal velocity, at the posterior end of the contractile actomyosin region, is initially peaked at about $15\mu m$ per minute, but rapidly drops to below $5\mu m$ per minute. These speeds are comparable with reported flow speeds during contraction of $5 - 8\mu m$ per minute [105-107].

4.2.5 Mutant phenotypes

Actomyosin dynamics and PAR localisation in cells depleted of the different *par* proteins have previously been characterised experimentally [104, 105, 107]. We have simulated the effects of the various mutants by making appropriate changes to the reaction scheme, discussed below. The results of these various changes are shown in figure 4.3.

In *par-3* mutants, PAR-6 and PKC-3 cannot associate with the cortex [104, 137, 138]. In these cells, the posterior PAR proteins are uniformly distributed throughout the cortex [104, 136], and actomyosin is cleared only from a small region around the posterior [107]. We model this mutant by preventing the remaining anterior PAR proteins from associating with the cortex, setting $c_{A1} = c_{A2} = 0$. This greatly suppresses actomyosin contraction, as shown in figure 4.3. Since the anterior PAR proteins cannot associate with the cortex, PAR-1 and PAR-2 are not excluded and hence accumulate uniformly at high levels, as seen in experiments. In our model, actomyosin contracts to approximately 85% of the embryo length, comparable to the experimentally measured actomyosin domain size of approximately 80% [107].

par-6 and *pkc-3* mutants have similar phenotypes to *par-3* mutants [104, 107]. PAR-6 is required to localise PKC-3 to the cortex [137] and (according to our model) thereby stimulate cortical exclusion of PAR-1 and PAR-2. In the absence of PAR-6, PKC-3 remains in the cytoplasm while PAR-3 is seen to associate with the cortex at lower levels than in wild-type embryos [151]. Similarly, in the absence of PKC-3, PAR-6 cannot become cortically localised [104, 138], while PAR-3 is again weakly detected at the cortex [137, 138]. We assume that cortical association of the remaining anterior PAR proteins is disrupted in these mutants, possibly due to the loss of interaction between PAR-6 and CDC-42 [140, 141]. We modelled both *par-6* and *pkc-3* mutants

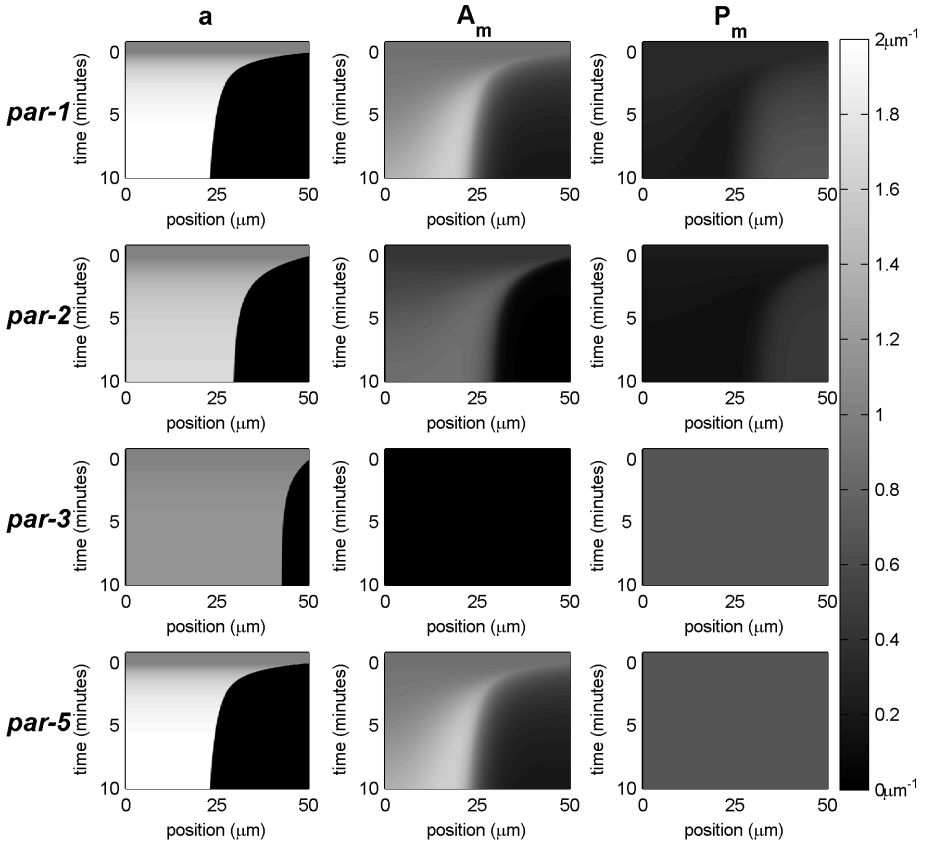

Figure 4.3: Cortical protein distributions in simulations of *par* mutant phenotypes. Simulations of equations (4.1-4.4) and (4.9) were performed with modifications to represent depletion of the different PAR proteins, as described in the text. The greyscale indicated on the right was used for all panels.

by allowing A to associate with the cortex at a reduced rate, reducing c_{A1} and c_{A2} by a factor of 4. In addition, we prevent A_m from excluding P_m, since cortical PKC-3 is required for this reaction. This was achieved by setting $c_{P4} = 0$. We found that the model behaviour was then similar to the *par-3* simulations described above for the posterior PAR proteins and actomyosin. The posterior PAR proteins are again uniformly distributed throughout the cortex, as observed experimentally for PAR-2 [104]. Quantitative measurements of the extent of actomyosin contraction in these mutants have not been reported. The different localisation patterns of PAR-3 and PAR-6/PKC-3 means that our assumption that the anterior PAR proteins function as a group is no longer valid. In implementing these mutants with the above

changes we slightly underestimate the density of cytoplasmic PAR-6/PKC-3, since we assume that these proteins are removed from the cytoplasm when A associates with the cortex. However, in our model, PKC-3 only interacts with the posterior PAR proteins when cortically localised, while PAR-6 has no direct effect on the posterior PAR proteins. We can therefore simply interpret A as the density of PAR-3 in these mutant simulations.

In *par-1* mutants, the anterior PAR domain retracts beyond mid-cell [104]. In our model, PAR-1 stimulates dissociation of the anterior PAR proteins. We simulate the *par-1* mutant by removing the competitive exclusion of A_m by P_m, $c_{A4} = 0$. PAR-2 is still able to associate with the cortex as in the wild-type [104, 136], although in our model it cannot stimulate exclusion of A_m. According to our model, since the anterior PAR proteins are not actively excluded from the cortex, higher levels accumulate, which stimulates greater actomyosin contraction, as shown in figure 4.3. PAR-2 appears at the cortex at reduced levels relative to wild-type, due to faster exclusion by PKC-3. The actomyosin network and anterior PAR domain rapidly contract to mid-cell and ultimately occupy approximately the anterior 45% of the embryo. Our model therefore produces the correct qualitative change relative to the wild-type dynamics for the anterior PAR domain, although the size of this domain is slightly larger in our model than is observed experimentally [104]. The extent of the actomyosin network in *par-1* mutants has not been reported. The initial rapid contraction of the anterior PAR domain appears somewhat faster than observed experimentally, where contraction beyond mid-cell takes approximately 6 minutes [104].

In *par-5* mutants the anterior and posterior PAR domains are seen to overlap [104, 144]. We assume that PAR-5 interacts with phosphorylated cortically-localised proteins and causes their dissociation. We therefore model this mutant by removing the competitive dissociation reactions between the cortical proteins, setting $c_{A4} = 0$ and $c_{P4} = 0$. This reproduces the overlapping domains of anterior and posterior PAR proteins observed experimentally, as shown in figure 4.3. The posterior PAR proteins remain uniformly localised, while the anterior PAR proteins become mostly restricted to an anterior cortical domain. These observations appear consistent with

experimental data [104], although the anterior PAR asymmetry appears somewhat more pronounced in our model than in experiments. In our simulations, *par-5* mutants show similar actomyosin contraction to *par-1* mutants. We are not aware of experimental measurements of the extent of actomyosin contraction in *par-5* mutants. Quantitative measurements of the PAR dynamics in *par-5* mutants are also complicated by the fact that the morphology of the cortex is much more irregular than in wild-type embryos [104].

Experiments in *par-2* mutants suggest that actomyosin contraction is slightly reduced relative to wild-type, although not as dramatically as in anterior PAR protein mutants [107]. Experimental measurements of the anterior PAR-6 domain in *par-2* mutants range from 50% [107] to 63% [104] of the cell length. PAR-2 has been suggested to promote cortical association of PAR-1 [136]. We model this by reducing the cortical association rate of P, c_{P1}, by a factor of 3. However, this effect alone is not sufficient to reproduce the observed dynamics. The reduced association rate of P leads to reduced cortical exclusion of A_m, and hence the anterior domain contracts beyond mid-cell in a similar way to the *par-1* mutant. This is qualitatively different from the reduced actomyosin contraction and expanded anterior PAR domain that are observed experimentally. Better agreement with the experimental dynamics can be achieved if, in addition to the reduced binding of PAR-1, we assume that PAR-1 is now more effective at excluding the anterior complex from the cortex than in the wild type. For example, PAR-2 may restrict access of PAR-1 to the appropriate phosphorylation sites on the anterior PAR proteins by binding to PAR-1, or because of crowding at the cortex. We included this effect by increasing the parameter c_{A4} by a factor of 4. Now even though PAR-1 is present at the cortex at lower levels, it is still able to effectively reduce the amount of A_m present. This result is shown in figure 4.3, where the anterior actomyosin and PAR domain both occupy approximately 60% of the embryo. The size of the anterior PAR domain is therefore comparable to experimental measurements [104, 107].

In summary, our model gives generally good agreement with the experimentally observed mutant phenotypes for the cortical PAR protein distributions. This agreement is especially encouraging given the great simplicity of the model.

4.2.6 Cytoplasmic polarity

A key feature of development in the early *C. elegans* embryo is the polarisation of cytoplasmic protein distributions, which leads to the asymmetric segregation of cytoplasmic proteins between daughter cells. The different cytoplasmic composition of these daughter cells leads to differentiation in development and cell fate. At the one-cell stage P-granules are restricted to the posterior, where they subsequently mark germline precursor cells [97]. Moreover, as the cortical PAR domains form, MEX-5/6 become restricted to the anterior cytoplasm [100, 104]. The cytoplasmic distribution of the posterior PAR proteins also appears polarised, with a higher density at the posterior [104]. PAR-1 has been suggested to negatively regulate MEX-5/6 activity, consistent with these proteins having oppositely polarised distributions [104]. It is therefore important to test whether our model is able to account for this cytoplasmic polarity.

We added an additional equation to the model to describe the cytoplasmic densities of MEX-5/6, M, as follows:

$$\frac{\partial M}{\partial t} = D_c \nabla^2 M + c_{M1} - c_{M2} M - c_{M3} P_c M \tag{4.9}$$

We assume that MEX-5/6 are uniformly produced at rate c_{M1} and degraded spontaneously at rate c_{M2}. We also allow MEX-5/6 to be degraded by P_c through the $c_{M3} M P_c$ term, consistent with negative regulation by PAR-1 [104]. For our simulations, we used the following parameter values: $c_{M1} = 0.1\mu m^{-1} s^{-1}$, $c_{M2} = 0.02 s^{-1}$, $c_{M3} = 0.135 \mu m s^{-1}$. Simulations were initialised with $M = 1\mu m^{-1}$, and the MEX-5/6 density at $t = 0$ was $M \approx 1\mu m^{-1}$.

Kymographs of the cytoplasmic protein densities resulting from the model equations (4.1-4.4) and (4.9) are shown in figure 4.2. As actomyosin contracts towards the anterior, the cytoplasmic distribution of the anterior PAR proteins also becomes polarised, with higher densities in the posterior cytoplasm. The posterior PAR proteins and MEX-5/6 are largely uniformly distributed, but with a slight increase in P_c at the anterior and M at the posterior. The cytoplasmic PAR distributions therefore have the opposite polarity to the cortical distributions. Hence, in our model, the

cytoplasmic PAR-1, PAR-2 and MEX-5/6 polarities are the opposite of those observed experimentally. The model also produces a polarised cytoplasmic distribution of the anterior PAR proteins, whereas experimentally the cytoplasmic PAR-6 density appears uniform [104].

This behaviour is a result of the model structure and cannot be rectified by simply changing values of the model parameters. The anterior PAR proteins bind preferentially in the anterior, causing depletion of A_c in the anterior relative to the posterior of the embryo. Dissociation of A_m is also faster in the posterior than in the anterior due to exclusion by P_m, which tends to further increase levels of A_c in the posterior part of the embryo. Similarly, dissociation of P_m is faster in the anterior of the embryo, where levels of A_m are high, than in the posterior. This leads to higher levels of P_c in the anterior. We conclude that the simple model considered thus far cannot explain the observed cytoplasmic distributions of the PAR proteins and the restriction of MEX-5/6 to the anterior cytoplasm. However, modifications to the model which correct these discrepancies may yield additional insight into the behaviour of the system.

4.3 Modifications to the basic model

4.3.1 MEX degradation by cortical PAR-1

While the cytoplasmic density of PAR-1 is higher in the anterior of the embryo than in the posterior in our model, the total density of cytoplasmic and cortical PAR-1 is higher at the posterior. Therefore, if cortical PAR-1 were able to affect MEX-5/6, the correct MEX-5/6 distribution could be produced even without the appropriate cytoplasmic PAR polarity. While there is no evidence that MEX-5/6 is present at the cortex, such an effect could occur if MEX-5/6 were to localise to the cortex transiently. This mechanism can be tested by introducing a cortical population of MEX-5/6 in addition to the cytoplasmic density, and allowing degradation of cortical MEX-5/6 to be induced by P_m rather than P_c. However, in order to effectively reverse the polarity of the cytoplasmic MEX-5/6 distributions, a significant proportion of the

total MEX-5/6 (about 10%) would have to be located at the cortex at any time. This mechanism therefore does not appear to be consistent with the available experimental evidence, especially as the cytoplasmic anterior and posterior PAR protein polarities remain incorrect.

4.3.2 Cortical and cytoplasmic flows

So far we have only coupled actomyosin contraction to PAR localisation indirectly, through the density of actomyosin. However, the actomyosin dynamics may also directly affect the localisation of the anterior PAR proteins, as cortical PAR-6 appears to move with the cortical actomyosin network [107]. Actomyosin contraction may also drive large-scale cytoplasmic flows, which carry cytoplasmic granules and vesicles [105, 106] thereby potentially affecting the cytoplasmic localisation of the PAR proteins. While our simple model shows that the motion of the PAR proteins in these flows is not necessary for the establishment of cortical polarity, it is possible that these flows contribute to cytoplasmic polarity by localising the posterior PAR proteins to the posterior of the embryo. We should therefore test these possible effects of introducing cortical and cytoplasmic flows. We model the motion of PAR proteins in cortical and cytoplasmic flows by adding advection to each of the model equations,

$$\frac{\partial A_m}{\partial t} = -\frac{\partial}{\partial x}(A_m v) + D_m \nabla^2 A_m + (c_{A1} + c_{A2} a) A_c - c_{A3} A_m - c_{A4} A_m P_m \quad (4.10)$$

$$\frac{\partial A_c}{\partial t} = -\frac{\partial}{\partial x}(A_c v_c) + D_c \nabla^2 A_c - (c_{A1} + c_{A2} a) A_c + c_{A3} A_m + c_{A4} A_m P_m \quad (4.11)$$

$$\frac{\partial P_m}{\partial t} = -\frac{\partial}{\partial x}(P_m v) + D_m \nabla^2 P_m + c_{P1} P_c - c_{P3} P_m - c_{P4} A_m P_m \quad (4.12)$$

$$\frac{\partial P_c}{\partial t} = -\frac{\partial}{\partial x}(P_c v_c) + D_c \nabla^2 P_c - c_{P1} P_c + c_{P3} P_m + c_{P4} A_m P_m \quad (4.13)$$

$$\frac{\partial M}{\partial t} = -\frac{\partial}{\partial x}(M v_c) + D_c \nabla^2 M + c_{M1} - c_{M2} M - c_{M3} P_c M \quad (4.14)$$

where $v(x,t)$ and $v_c(x,t)$ are velocity fields for the cortical and cytoplasmic flows respectively.

The appropriate velocity field, v, in the contracting actomyosin region can be calculated directly from our actomyosin model. We consider the conservation equation

for actomyosin,

$$\frac{\partial a}{\partial t} = -\frac{\partial}{\partial x}(av). \tag{4.15}$$

Since the density, a, remains uniform over $0 \leq x \leq l(t)$, $\frac{\partial a}{\partial t}$ must be the same everywhere in this region. This requires that $\frac{\partial v}{\partial x}$ also be uniform as a function of x. Finally, we can integrate and use the boundary conditions $v(0,t) = 0$ and $v(l(t),t) = v_l(t)$ to find

$$v(x,t) = v_l(t)\frac{x}{l(t)} \quad 0 \leq x \leq l(t), \tag{4.16}$$

as we would expect for a uniform spring. The remaining cortical and cytoplasmic flows are not given by our actomyosin model, so we will simply assume approximate forms for these flows. Other choices were also tested, and did not significantly alter the dynamics. We take the anterior-directed flow in the posterior cortex to be

$$v(x,t) = v_l(t)\frac{L-x}{L-l(t)} \quad l(t) < x \leq L. \tag{4.17}$$

This ensures that v is continuous at $x = l(t)$, and that the flow speed goes to zero at the posterior pole. It is also in general agreement with experimental observations [105]. We choose the cytoplasmic flow velocity in our model to be fastest near mid-cell, with the maximal flow velocity proportional to the maximal flow speed of the cortex:

$$v_c(x,t) = \begin{cases} -kv_l(t)\frac{x}{L/2} & 0 \leq x \leq L/2 \\ -kv_l(t)\frac{L-x}{L/2} & L/2 < x \leq L \end{cases}. \tag{4.18}$$

These forms are broadly consistent with experimental observations [105], where it appears that cytoplasmic flow speeds are reduced near the poles. k is a parameter chosen to match the cytoplasmic velocity to that observed experimentally; we used $k = 4/7$.

The advection of the PAR proteins was simulated with a first-order difference scheme, by calculating the flux between each pair of lattice sites. The change in

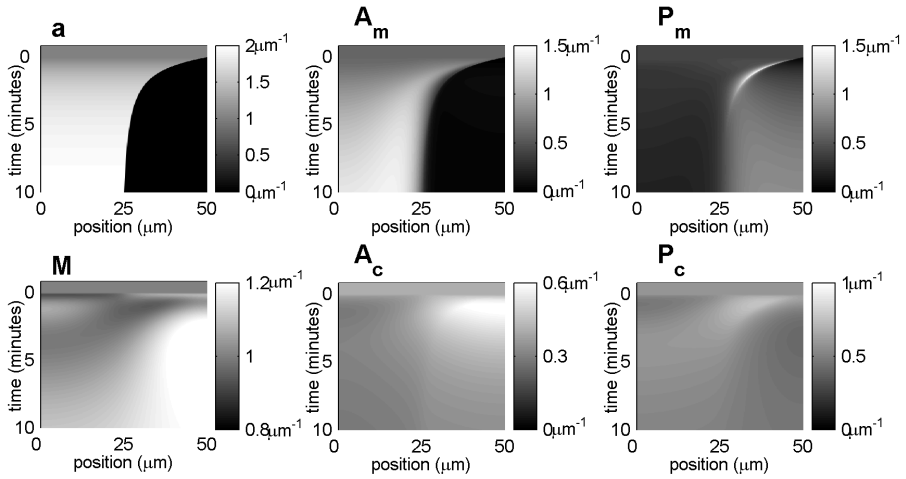

Figure 4.4: Model dynamics with advection of PAR proteins. Simulations of the wild-type model were performed with the modified model equations (4.10-4.14).

density at each lattice site due to advection is given by

$$\Delta\rho_i = \begin{cases} -\frac{\delta t}{\delta x}(v_i\rho_i - v_{i-i}\rho_{i-1}) & \text{if } v_i > 0 \\ -\frac{\delta t}{\delta x}(v_i\rho_{i+1} - v_{i-i}\rho_i) & \text{if } v_i < 0 \end{cases}. \tag{4.19}$$

Here v_i represents the velocity at the boundary between sites i and $i+1$. Boundary conditions were applied to ensure that $v(0) = v(L) = 0$. Since the flows are relatively slow and smooth ($|(\delta t)v_i| \ll \delta x$), and unidirectional, we find that this discretisation scheme remains well-behaved. A centred-difference scheme was also tested, with no change in the results.

The wild-type model dynamics with advection of the PAR proteins are shown in figure 4.4. During the early part of the polarity establishment process, we can identify dynamic features in the PAR distributions which are the result of the advection of these proteins. As we would expect, cytoplasmic flows carry the cytoplasmic PAR proteins into the posterior, generating a transiently higher density of A_c and P_c. Cortical flows also lead to a narrow, high-density, band of P_m near the interface of the anterior/posterior PAR cortical domains. However, the stable polarised distributions that form at late times are unchanged. Assuming sufficiently fast cytoplasmic diffusion (D_c larger than about $1\mu m^2 s^{-1}$), the system reaches a steady-state determined

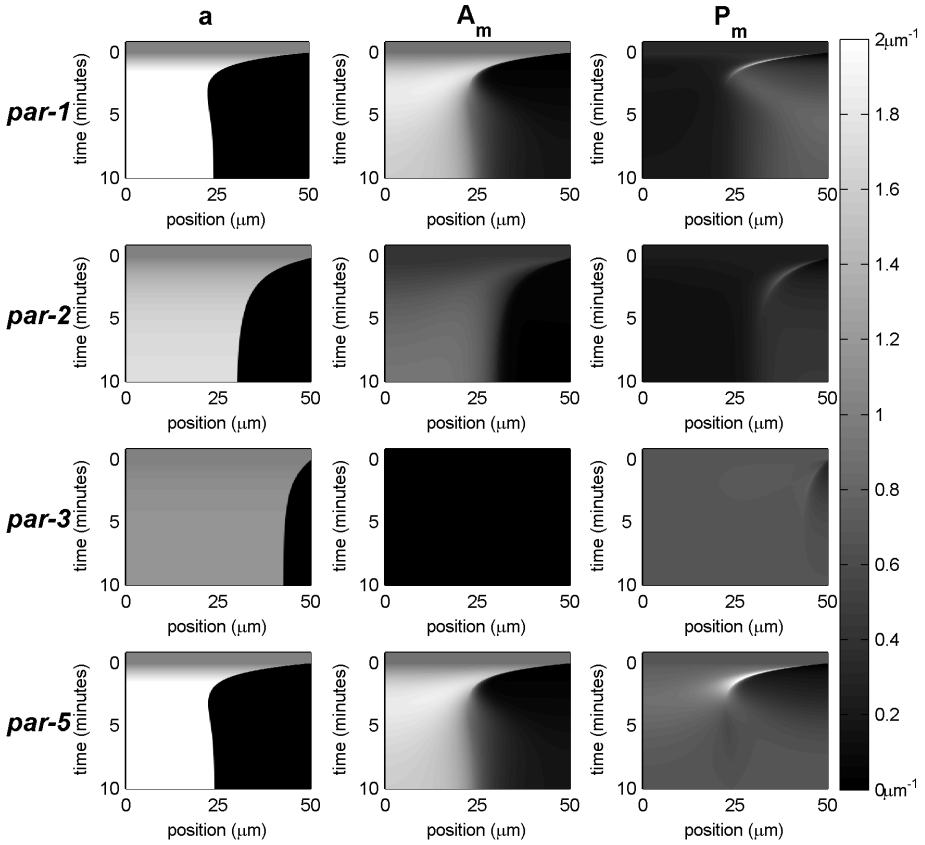

Figure 4.5: Simulations of *par* mutants with cortical and cytoplasmic flows. The greyscale indicated on the right was used for all panels.

by diffusion and the protein interactions, whose timescales are short compared to the timescales over which cortical and cytoplasmic flows occur. We therefore conclude that movement of the PAR proteins in cortical and cytoplasmic flows likely cannot account for cytoplasmic polarity in the embryo, and moreover, the flows lead to only minor transient changes in the cortical PAR distributions.

For completeness, simulations of the *par* mutants were also performed with cortical and cytoplasmic flows of the PAR proteins. As in the wild-type simulations, the establishment of polarity and the final PAR distributions were unaffected in all mutants. However, the dynamics in *par-1* and *par-5* mutants in particular showed some transient differences during the early phase of the contraction dynamics. In the model without advection, the intitially cortical anterior PAR proteins do not move with the actomyosin domain as it contracts into the anterior. The total levels of A_m in

the contractile region therefore decrease gradually as contraction takes place. If cortical flows are added the rapid advection overwhelms protein diffusion, so A_m proteins are carried with the actomyosin domain and remain confined within the contractile region. Contraction therefore occurs more rapidly and to a greater extent than in the model without flows. However, once the flow velocity decreases these additional proteins can once again diffuse out of the anterior region. This reduces levels of A_m, and leads to the slight re-expansion of the anterior domain which can be seen in figure 4.5.

4.3.3 Competitive degradation

The incorrect cytoplasmic polarity of the basic model appears in part because rapid competitive exclusion of cortical proteins increases the cytoplasmic density in the wrong half of the embryo. This effect can be overcome if proteins which are excluded from the cortex are not returned to the cytoplasmic pool, but instead are rapidly degraded. We therefore introduce into the model competitive degradation of the two PAR groups, perhaps due to the known phosphorylation reactions. We also add competitive degradation between the cytoplasmic A_c and P_c groups to further enhance the cytoplasmic polarity. To ensure stable levels of the various PAR proteins, homogeneous production (and spontaneous degradation) in the cytoplasm are also introduced. The resulting model equations are

$$\frac{\partial A_m}{\partial t} = D_m\nabla^2 A_m + (c_{A1} + c_{A2}a)A_c - c_{A3}A_m - c_{A4}A_m P_m \quad (4.20)$$

$$\frac{\partial A_c}{\partial t} = D_c\nabla^2 A_c - (c_{A1} + c_{A2}a + c_{A6})A_c + c_{A3}A_m + c_{A5} - c_{A7}A_c P_c \quad (4.21)$$

$$\frac{\partial P_m}{\partial t} = D_m\nabla^2 P_m + c_{P1}P_c - c_{P3}P_m - c_{P4}A_m P_m \quad (4.22)$$

$$\frac{\partial P_c}{\partial t} = D_c\nabla^2 P_c - (c_{P1} + c_{P6})P_c + c_{P3}P_m + c_{P5} - c_{P7}A_c P_c \quad (4.23)$$

$$\frac{\partial M}{\partial t} = D_c\nabla^2 M + c_{M1} - c_{M2}M - c_{M3}P_c M \quad (4.24)$$

c_{A5} is a constant production term for the anterior PAR proteins. Production of P is similarly controlled by c_{P5}. c_{A6} and c_{P6} are spontaneous degradation rates for A_c and

P_c respectively. $c_{A7}A_cP_c$ and $c_{P7}A_cP_c$ represent competitive degradation reactions between the anterior and posterior PAR proteins in the cytoplasm. Since we assume that cortical interactions lead to protein degradation, the $c_{A4}A_mP_m$ and $c_{P4}A_mP_m$ terms have been removed in (4.21) and (4.23) respectively.

Since we have added production and degradation, the total protein levels can be altered by changing these parameters. In *par* mutants the degradation reactions can be disrupted, leading to different protein expression levels from wild-type. If levels of A increase significantly it would be possible for the natural length, $\Lambda(t)$ given by (4.7) and (4.8), to become negative. Since this situation is unphysical, to remove this possibility we introduce saturation of $m(t)$ when levels of A_m are high,

$$m(t) = \frac{\frac{1}{L}\int_0^{l(t)} A_m dx}{1 + \frac{\sigma}{L}\int_0^{l(t)} A_m dx}. \tag{4.25}$$

In simulations of this model we used the following parameters values: $L = 50\mu m$, $\Lambda_1 = 42.5\mu m$, $\Lambda_1 = 60\mu m^2$, $\sigma = 1.75\mu m$, $\epsilon = 0.35\mu m s^{-1}$, $D_m = 0.25\mu m 2s^{-1}$, $D_c = 5\mu m^2 s^{-1}$, $c_{A1} = 0.008s^{-1}$, $c_{A2} = 0.072\mu m s^{-1}$, $c_{A3} = 0.032s^{-1}$, $c_{A4} = 0.008\mu m s^{-1}$, $c_{A5} = 0.1\mu m^{-1}s^{-1}$, $c_{A6} = 0.08s^{-1}$, $c_{A7} = 0.35\mu m s^{-1}$; $c_{P1} = 0.064s^{-1}$, $c_{P3} = 0.032s^{-1}$, $c_{P4} = 0.16\mu m s^{-1}$, $c_{P5} = 0.08\mu m^{-1}s^{-1}$, $c_{P6} = 0.06s^{-1}$, $c_{P7} = 0.016\mu m s^{-1}$. With these parameters, the densities at $t = 0$ are $A_c \approx 0.3\mu m^{-1}$, $A_m \approx 0.7\mu m^{-1}$, $P_c \approx 0.7\mu m^{-1}$, $P_m \approx 0.3\mu m^{-1}$, $M \approx 0.9\mu m^{-1}$. Simulation results for the wild-type are shown in figure 4.6. The data show correctly polarised distributions of P_c and M, and a slight anterior gradient of A_c.

Mutant simulations were also performed with this model, implemented as follows:

- *par-1*: We assume PAR-1 causes cortical and cytoplasmic degradation of the anterior PAR proteins and MEX-5/6. We therefore simulate this mutant by setting $c_{A4} = 0$, $c_{A7} = 0$, and $c_{M3} = 0$.

- *par-2*: As for the basic model, we simulated this mutant by reducing the binding rate of PAR-1, c_{P1}, by a factor of 3 and increasing c_{A4} by a factor of 4.

- *par-3*: As in the initial model, we prevent the anterior PAR proteins from

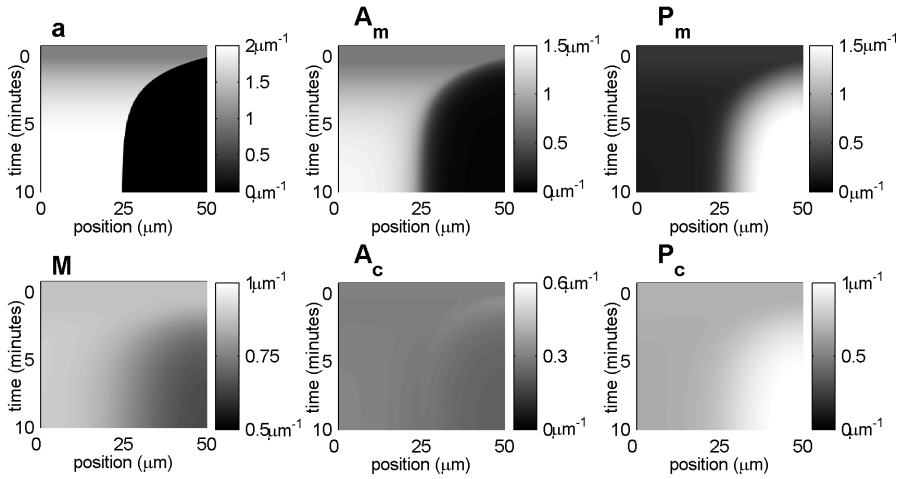

Figure 4.6: Wild-type simulation results for the model with competitive protein degradation.

associating with the cortex, $c_{A1} = c_{A2} = 0$.

- *par-5*: We assume PAR-5 is required for exclusion and degradation of cortical proteins. As in the initial model, we incorporated this effect by setting $c_{A4} = 0$ and $c_{P4} = 0$. However, we assume that PAR-5 is not required for cytoplasmic degradation reactions. These reactions were therefore left unchanged.

The results of mutant simulations are shown in figure 4.7. In all cases, the extent of the anterior domain is consistent with experimental observations [104, 107]. The timescales for contraction are also consistent with experiment, except in the case of *par-1* for which contraction again appears slightly faster than observed experimentally [104]. In addition to altered localisation patterns, the exclusion and degradation rates will also differ in the mutants as compared to the wild type, leading to very different expression levels, as shown in figure 4.8. In our simulations we see up to a five-fold change relative to wild-type, although this value is highly dependent on the model parameters.

With these modifications, the model is able to reproduce the appropriately polarised cytoplasmic distributions, and can also give good agreement with all experimentally observed mutant phenotypes. However, in order to generate the observed polarised distributions the PAR proteins would have to be rapidly turned over. The

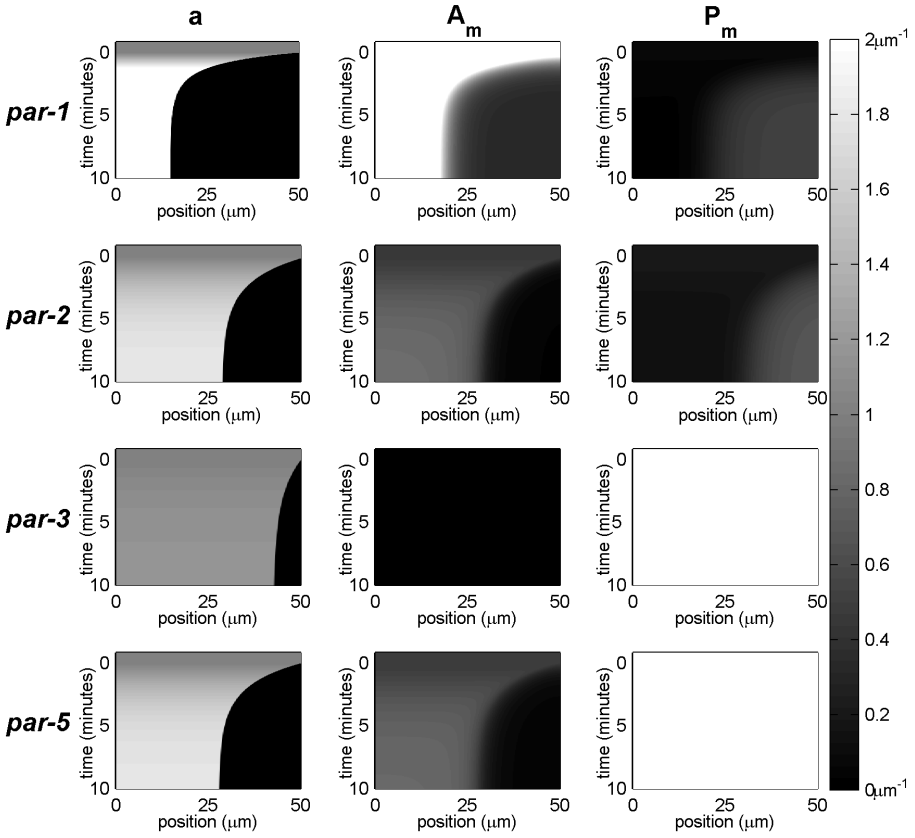

Figure 4.7: Results for simulations of *par* mutants in the competitive degradation model. The greyscale indicated on the right was used for all panels.

posterior PAR proteins, for example, must be displaced from the cortex on a timescale of minutes – otherwise P_m would remain uniform as the anterior PAR proteins are restricted to the anterior. If the displaced proteins are immediately degraded, this implies lifetimes also on the order of minutes. Such a rapid synthesis rate would be extremely energetically expensive to maintain.

4.3.4 Cytoplasmic cytoskeletal asymmetry

The polarisation of the embryo cortex is driven by rearrangement of the cortical actomyosin network. It is possible that the generation of cytoplasmic polarity is similarly driven by cytoskeletal rearrangement. PAR-2 is able to localise to the pronuclei or spindle and has been suggested to interact with microtubules [104, 152]. During the

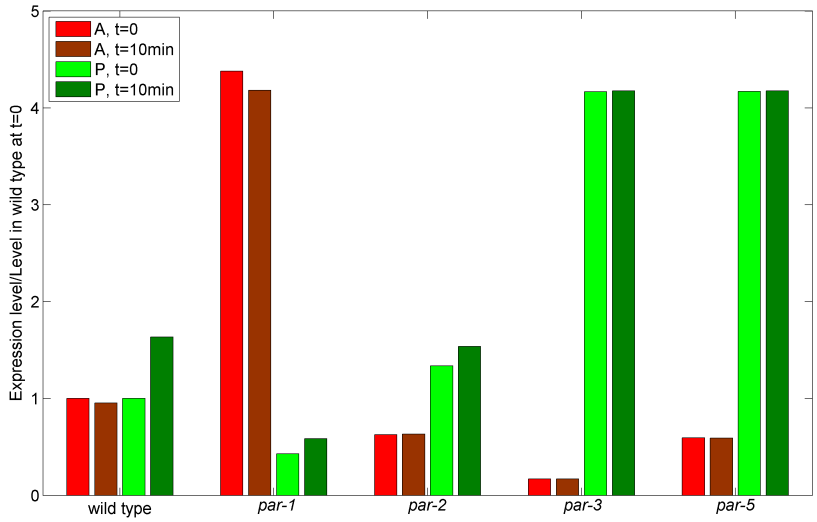

Figure 4.8: Protein levels in *par* mutants in the competitive degradation model. Shown are the total amounts of A and P at $t = 0$ and at $t = 10$ minutes, normalised by the amount at $t = 0$ in the wild-type simulations.

period of PAR polarity establishment, microtubules form primarily in the posterior part of the embryo as the pronuclei migrate and meet in the posterior [104, 141]. If the posterior PAR proteins are colocalised with the microtubules, this could effectively confine these proteins to the posterior cytoplasm. There is also evidence that cytoplasmic actin becomes largely restricted to the anterior [139]. If the cytoplasmic anterior PAR proteins are colocalised with the cytoplasmic actin, through a similar mechanism to their preferential localisation to the anterior cortex, this could help to confine the cytoplasmic anterior PAR proteins to the anterior cytoplasm. Hence, this effect could neutralise the posterior polarity for A_c found in our initial model, and thus lead to a uniform distribution for A_c, as observed experimentally.

To test this mechanism, we modify the basic model in equations (4.1-4.4) to introduce a second cytoplasmic state for the anterior and posterior PAR groups, A_i and P_i respectively. These variables represent proteins associated with the cytoplasmic cytoskeleton which are partly immobilised and also unable to bind to the cortex. We assume that the local cytoplasmic actin density consists of two contributions, a constant component which is uniformly distributed throughout the embryo, and a varying component which moves with the cortical actomyosin network and has den-

sity proportional to $a(x,t)$. We therefore take the local cytoplasmic actin density to be proportional to $(1+c_a a(x,t))$. As a simple estimate, we assume that the microtubule density is inversely related to the density of actomyosin, with the form $(1+c_a a(x,t))^{-1}$. However, our results are not specific to these particular choices for the cytoskeletal densities. We allow anterior and posterior cytoplasmic PAR proteins to associate with the appropriate cytoplasmic cytoskeletal constituent at a rate proportional to the effective cytoskeletal density. Binding to the cytoskeleton will restrict diffusion of A_i and P_i, so we assume the same diffusion constant, D_m, as for cortical proteins. The resulting equations are

$$\frac{\partial A_m}{\partial t} = D_m\nabla^2 A_m + (c_{A1}+c_{A2}a)A_c - c_{A3}A_m - c_{A4}A_m P_m \tag{4.26}$$

$$\frac{\partial A_c}{\partial t} = D_c\nabla^2 A_c - (c_{A1}+c_{A2}a)A_c + c_{A3}A_m + c_{A4}A_m P_m - c_{A5}(1+c_a a)A_c + c_{A6}A_i \tag{4.27}$$

$$\frac{\partial A_i}{\partial t} = D_m\nabla^2 A_i + c_{A5}(1+c_a a)A_c - c_{A6}A_i \tag{4.28}$$

$$\frac{\partial P_m}{\partial t} = D_m\nabla^2 P_m + c_{P1}P_c - c_{P3}P_m - c_{P4}A_m P_m \tag{4.29}$$

$$\frac{\partial P_c}{\partial t} = D_c\nabla^2 P_c - c_{P1}P_c + c_{P3}P_m + c_{P4}A_m P_m - \frac{c_{P5}}{1+c_a a}P_c + c_{P6}P_i \tag{4.30}$$

$$\frac{\partial P_i}{\partial t} = D_m\nabla^2 P_i + \frac{c_{P5}}{1+c_a a}P_c - c_{P6}P_i \tag{4.31}$$

$$\frac{\partial M}{\partial t} = D_c\nabla^2 M + c_{M1} - c_{M2}M - c_{M3}(P_c+P_i)M \tag{4.32}$$

We simulated these equations with parameters $c_a = 5\mu m$, $c_{A1} = 0.013s^{-1}$, $c_{A2} = 0.091\mu m^{-1}$, $c_{A5} = 0.003s^{-1}$, $c_{A6} = 0.06s^{-1}$, $c_{P1} = 0.096s^{-1}$, $c_{P5} = 0.04s^{-1}$, $c_{P6} = 0.04s^{-1}$, and the other parameters unchanged from the initial model. The $t=0$ state in the wild-type simulations is $A_c \approx 0.3\mu m^{-1}$, $A_m \approx 0.6\mu m^{-1}$, $A_i \approx 0.1\mu m^{-1}$, $P_c \approx 0.5\mu m^{-1}$, $P_m \approx 0.4\mu m^{-1}$, $P_i \approx 0.1\mu m^{-1}$, $M \approx 1\mu m^{-1}$.

Figure 4.9 confirms that this mechanism is able to suitably polarise the distributions of cytoplasmic P and MEX-5/6 and to generate a uniform cytoplasmic distribution of A, whilst retaining the cortical polarity of the basic model. For this mechanism to be effective a significant fraction of the cytoplasmic PAR proteins must be in the

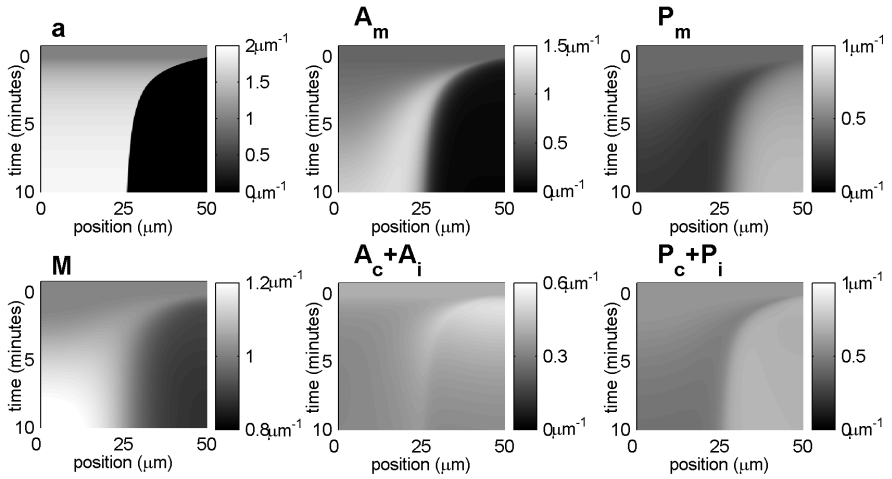

Figure 4.9: Simulation results for the model with partial immobilisation of the cytoplasmic PAR proteins. A_i and P_i represent the densities of the partly immobilised cytoplasmic forms of the anterior and posterior PAR proteins respectively. In this case, approximately half of the cytoplasmic posterior PAR proteins were in the immobile form.

immobile forms. We found that in order to reverse MEX-5/6 polarity, a ratio of partly immobilised to total cytoplasmic P of at least 0.25 was required in the posterior of the embryo. Simulations of the *par* mutants were also performed with this model, as described previously. In all cases, the behaviour of this model was essentially the same as the simple model (4.1-4.4) and (4.9).

4.4 Discussion

We have presented a mathematical model that couples interactions between the PAR proteins to actomyosin contraction, and largely reproduces the observed phenomenology of the PAR system at the one-cell stage of the *C. elegans* embryo. The cortical protein distributions in the wild-type and in *par*-depletion mutants can be explained through the currently understood reactions of cortical association and competitive exclusion. Our model also confirms that polarisation of the cortical actomyosin network is crucial for the correct establishment of polarity, restricting PAR-3/PAR-6/PKC-3 localisation to the anterior, which in turn leads to polarisation of PAR-1 and PAR-2 proteins. However, we predict that motion of the PAR proteins in flows that result

from this contraction are not required to achieve the correct protein distributions, since the model performs well without the inclusion of these effects.

The simple model considered here is consistent with the experimentally reported interactions and with a mutual exclusion mechanism for the cortical PAR proteins proposed previously [104]. However, reproducing the correct cytoplasmic polarity of the PAR proteins is not straightforward. This issue has received surprisingly little attention, and the processes by which cytoplasmic polarity is generated are not understood. Regulating cytoplasmic polarity through MEX-5/6 and other CCCH-finger proteins is a vital function of the PAR system, crucial for the correct development of the different daughter cells. Our modelling clearly shows that the establishment of the correct cortical polarity is not sufficient to guarantee the appropriate cytoplasmic polarity of PAR-1/PAR-2 and MEX-5/6. We therefore considered a number of possible mechanisms by which the correct cytoplasmic polarity could be achieved, and experiments should be able to directly test, and distinguish between, these different mechanisms.

Intuitively, it would appear likely that the posterior-directed cytoplasmic flow would play a role in establishing cytoplasmic asymmetry. The flow of cytoplasmic material may carry with it the posterior PAR proteins, leading to a polarised distribution of these proteins in the cytoplasm. Our model suggests that this transient polarity would be difficult to maintain once these cytoplasmic flows cease. Diffusion of the PAR proteins in the cytoplasm together with cortical binding and exclusion reactions would then rapidly disrupt the earlier PAR-1 and PAR-2 distributions. Experimentally the cytoplasmic distributions appear to remain stably polarised between pseudocleavage and cell division [104]. However, we have assumed throughout that the P_c proteins are able to diffuse rapidly within the embryo cytoplasm ($D_c = 5\mu m^2 s^{-1}$). The impact of the cytoplasmic flow on the final PAR distributions increases when diffusion of the P_c proteins is slow. For example, if the P_c proteins cannot diffuse freely (D_c less than about $1\mu m^2 s^{-1}$), then the cytoplasmic flows may significantly contribute towards the polarised distributions of PAR-1 and PAR-2. It would therefore be interesting to measure the mobility of the PAR proteins in the cytoplasm, for example by FRAP analysis, as a test of this conclusion. The posterior-directed

cytoplasmic flows cannot, however, account for the cytoplasmic distributions of the anterior PAR proteins or of MEX-5/6.

A competitive degradation model is able to reproduce the correct cytoplasmic and cortical dynamics. However, the necessary protein turn-over rates are so fast that this mechanism appears less likely. A number of relatively simple experiments should be able to show conclusively whether this mechanism is actually used *in vivo*. It is not clear whether the PAR proteins are in fact translated during the one-cell stage of development. Photobleaching of an entire embryo with fluorescently labelled PAR proteins, and observing recovery, could indicate whether the rate of protein production was sufficiently fast for the mechanism proposed above to be viable. Alternatively, blocking translation in the embryo would lead to a rapid decrease in PAR protein levels. We would expect these differences to be readily observable in experiments. This prediction contrasts strongly with predictions from our other models which suggest that PAR protein translation/degradation are not required at all for polarity establishment.

We have suggested that cytoplasmic asymmetry of the cytoskeleton may drive the establishment of cytoplasmic protein polarity in parallel to the establishment of cortical PAR polarity. The anterior PAR proteins could potentially be retained in the anterior by a polarised distribution of cytoplasmic actin, and microtubules could similarly localise the posterior PAR proteins to the posterior cytoplasm. Our model also suggests that the observed uniform distribution of the anterior PAR proteins is in fact the result of a balance between two competing effects. The asymmetric binding and dissociation reactions included in our basic model tend to produce a posteriorly-polarised cytoplasmic distribution. However, binding to an anterior polarised distribution of cytoplasmic actin largely cancels this effect, leading to a uniform cytoplasmic distribution of the anterior PAR proteins, in agreement with experiment. Important evidence in favour of this mechanism would be confirmation of the asymmetric cytoplasmic actin distribution suggested in [139]. Disrupting the cytoplasmic actomyosin components without affecting cortical contraction would be difficult. However, experiments to probe the role of microtubules would be possible without affecting cortical polarity. If microtubules are indeed responsible for retaining the

posterior PAR proteins in the posterior cytoplasm, we would expect the cytoplasmic polarity of PAR-1 and PAR-2 to be reversed if microtubule polymerisation could be appropriately disrupted. This mechanism can potentially explain cytoplasmic polarity during the pronuclear migration period, when the distribution of microtubules is biased towards the posterior of the embryo. However, it is still not clear how polarity would be maintained after pronuclear meeting, when the distribution of microtubules becomes more uniform.

The models discussed above include a highly simplified description of the actomyosin network. While a detailed model of actomyosin activity may give a more mechanistic description of the contraction dynamics and smaller-scale phenomena such as cortical ruffling and pseudocleavage, we were able to capture the correct dynamics at the cellular scale important for cell polarity. The good agreement between the model and experiment supports the use of such a coarse-grained model, and shows that a more detailed model is not necessary to explain the polar organisation of the PAR proteins. Our model does not, however, explain the secondary flows that are observed after pseudocleavage in *par* mutant embryos. In *par-2* mutants, actomyosin and the anterior PAR proteins flow back towards the posterior pole [104, 107]. In *par-1* and *par-5* mutants, the actomyosin distribution after pseudocleavage has not been reported, but the anterior PAR domain expands towards the posterior in both cases [104]. The slight re-expansion which is observed in figure 4.5 should not be identified with these posteriorly directed flows, as it during too soon after the initiation of polarity establishment and cannot account for the full extent of these posterior flows, nor for the dynamics in *par-2* mutants. It is therefore possible that our simple elastic model breaks down in this regime. A spring model in which the natural length is altered after pseudocleavage could potentially reproduce the correct PAR dynamics. However, it is not clear how the natural length in such a model should be determined. Munro et al [107] suggested that PAR-2 prevents re-expansion of the anterior domain after pseudocleavage by suppressing myosin binding. It is not clear why such a mechanism is not effective in *par-1* and *par-5* mutants, where PAR-2 is present at the cortex but posterior expansion of the anterior domain is observed. Alternatively, an inhomogeneous model including the posterior density of actomyosin

together with myosin binding and unbinding reactions could potentially describe this behaviour.

It is not clear whether actomyosin contraction in the wild-type embryo specifically targets the mid-embryo position, whereby the boundary between the anterior and posterior domains scales with embryo length, as occurs, for example, in the hunchback expression boundary in the Drosophila embryo [115]. Our model does not specifically self-organise to identify the mid-cell position – this must be achieved through appropriate parameter choices. However, scaling with embryo length can be achieved if the natural length in our actomyosin spring model is taken to be proportional to the embryo length. This can be achieved if the PAR protein and actomyosin densities remain constant as a function of embryo length. It would certainly be interesting to test the scaling properties of the anterior domain experimentally.

The model presented here deals specifically with the one-cell *C. elegans* embryo. One of the striking features of the PAR system is its conservation between different cell types and organisms [90-92]. In many cases cell polarity and actin reorganisation are linked [93, 94, 107], although we are not aware of any other examples where polarity establishment is accompanied by such large-scale rearrangement of cellular material. Our model suggests these secondary cytoplasmic flows are not required to achieve the correct polarity, and that segregation of the actomyosin network together with competitive interactions between the PAR proteins are the keys to establishing PAR polarity. Some aspects of the model may therefore be directly applicable in other contexts.

Chapter 5

Conclusion

We have presented and discussed three mathematical models applied to specific subcellular processes. In chapter 2 we considered a stochastic model of the pole-to-pole Min oscillations in *E. coli* [40]. The model relies on a dynamic instability in the network of protein reactions together with diffusive dynamics to drive these oscillations. We investigated possible roles for polymerisation, and studied for the first time partitioning of the Min proteins during cell division, finding that the partitioning is generally highly uneven. In chapter 3 we considered limits to positional precision in concentration gradients [74]. The instantaneous density fluctuations in gradients *in vivo* may be so large that estimating position from density measurements will be unreliable. Time-averaging is required in order to achieve reliable position determination. Finally, in chapter 4 we described a model of PAR polarity in *C. elegans*. We have considered a plausible interaction network which is able to reproduce much of the observed phenomenology, and where this model fails we have suggested modifications which allow the model to capture more of the experimental behaviour. We also investigated roles for actomyosin contraction, showing that this was required to generate different anterior and posterior domains, but that cortical and cytoplasmic flows are not necessary for the establishment of polarity.

There are numerous differences in structure and behaviour between the various models. The model of Min oscillations and the model of PAR polarity both deal with the generation of spatial localisation in an initially uniform system. However,

the mechanisms by which this is accomplished are very different. In the case of Min oscillations, spatial organisation arises spontaneously due to dynamic instability. Establishing PAR polarity requires the driving force of actomyosin contraction, which imposes spatial inhomogeneity on the system. In the gradient systems considered in chapter 3, the symmetry of the system was also broken by the predetermined gradient. In both the Min and gradient models we included important stochastic effects, whereas for the PAR proteins we considered only a continuum description of the system. This diversity in models is ultimately driven by the variety of biological systems under consideration. The construction of a model must be tailored to the particular system of interest. However, it is also due in part to the questions which the models are seeking to investigate.

In constructing models of biological systems there are broadly two distinct approaches. The first is a search for completeness and the inclusion of all the interactions and details which are known about a system. This can be an advantage in systems which are well studied and in which parameters such as reaction rates have been quantified. In these cases, such models can yield quantitative predictions about the detailed system behaviour. Of the models discussed here, the model of Min oscillations in chapter 2 includes the most detailed description of the system, with all known interactions and protein species, and the introduction of membrane structure. This model built on a range of previous work [31-34] which had shown that a dynamic instability mechanism was able to reproduce the observed dynamics. The reactions in this system are relatively well understood. The model presented here was therefore focused on aspects of the system which had not previously been considered, such as the dynamics during cell division.

However, in systems where there is more uncertainty, increasing levels of complexity can obscure the fundamental properties and key features of the system while adding little benefit. In such cases, models may have a more reductionist approach, seeking to represent the system in terms of a minimal number of components and effective interactions. Such models have the advantage of simplicity, and can allow for a more intuitive understanding of the system. The model of the PAR proteins in chapter 4 lies much closer to this approach. This was the first attempt at modelling

these phenomena, in a system where there is still considerable uncertainty about specific reactions. Many details of the interaction network are not well understood. The model was therefore focused on more basic questions, such as whether the proposed mechanisms and interaction network were viable. We therefore considered the system at a highly coarse-grained level and simplified the included reactions somewhat by considering only the anterior and posterior protein groups, also neglecting stochastic effects due to low protein copy numbers. However, the necessity of reducing complexity may mean that these simplified models are unable to reproduce the finer details of the system behaviour. Our basic actomyosin model, for example, cannot account for more detailed features of the experimentally observed dynamics, such as the smaller-scale cortical ruffling.

The goal of our analysis of gradient models of chapter 3 was not to study a specific example system, but instead to understand more general properties of concentration gradients. In many ways, these models are more abstract than the other examples presented. We therefore selected simple but widely applicable mechanisms for gradient formation. This also has the advantage of making analytic calculations straightforward, whereas for more complex systems of non-linear interactions this may not be the case.

Although we have come to understand some of the mechanisms behind these subcellular spatial phenomena, through the use of experimental observations and computer simulations, it is often not clear why biological systems have developed in this way. Again, the Min system in *E. coli* is a prime example. It is not known why *E. coli* has such an extravagant mechanism for regulating cell division while other bacteria, such as *B. subtilis* (which lacks MinE) and *Caulobacter*, employ much simpler accumulations of division inhibitors at both cell poles [45, 153] without oscillations. Similar questions can be asked of the early stages of *C. elegans* development. The embryos of other organisms also become polarised at early stages of development, but without such dramatic symmetry breaking in the cytoskeleton or cytoplasmic flows [93, 154]. The answers to these questions and many others must await further biological insight.

References

[1] B. Alberts, A. Johnson, J Lewis, M. Raff, K. Roberts, and P. Walter. *Molecular Biology of the Cell*. Garland Science, 4th edition, 2002.

[2] J. Lowe and L.A. Amos. Crystal structure of the bacterial cell-division protein FtsZ. *Nature*, 391:203–6, 1998.

[3] F. van den Ent, L.A. Amos, and J. Lowe. Prokaryotic origin of the actin cytoskeleton. *Nature*, 413:39–44, 2001.

[4] J. Lutkenhaus. FtsZ ring in bacterial cytokinesis. *Mol. Microbiol.*, 9:403–9, 1993.

[5] T. Kruse, J. Moller-Jensen, A. Lobner-Olesen, and K. Gerdes. Dysfunctional MreB inhibits chromosome segregation in *Escherichia coli*. *EMBO J.*, 22:5283–92, 2003.

[6] Z. Gitai, N. Dye, and L. Shapiro. An actin-like gene can determine cell polarity in bacteria. *Proc. Natl Acad. Sci. USA*, 101:8643–8, 2004.

[7] M.T. Cabeen and C. Jacobs-Wagner. Bacterial cell shape. *Nat. Rev. Microbiol.*, 3:601–10, 2005.

[8] Z. Gitai. The new bacterial cell biology: Moving parts and subcellular architecture. *Cell*, 120:577–86, 2005.

[9] D. Kentner and Sourjik V. Spatial organization of the bacterial chemotaxis system. *Curr. Opin. Microbiol.*, 9:619–24, 2006.

[10] D.C.-H. Lin and A.D. Grossman. Identification and characterization of a bacterial chromosome partitioning site. *Cell*, 92:675–85, 1998.

[11] A.L. Marston and J. Errington. Dynamic movement of the ParA-like Soj protein of *B. subtilis* and its dual role in nucleoid organization and developmental regulation. *Mol. Cell*, 4:673–82, 1999.

[12] K. Doubrovinski and M. Howard. Stochastic model for Soj relocation dynamics in *Bacillus subtilis*. *Proc. Natl Acad. Sci. USA*, 102:9808–13, 2005.

[13] J. Stricker, P. Maddox, E.D. Salmon, and H.P. Erickson. Rapid assembly dynamics of the Escherichia coli FtsZ-ring demonstrated by fluorescence recovery after photobleaching. *Proc. Natl Acad. Sci. USA*, 99:3171–5, 2002.

[14] S. Thanedar and W. Margolin. FtsZ exhibits rapid movement and oscillation waves in helix-like patterns in *Escherichia coli*. *Curr. Biol.*, 14:1167–73, 2004.

[15] D.M. Raskin and P.A.J. de Boer. Rapid pole-to-pole oscillation of a protein required for directing division to the middle of *Escherichia coli*. *Proc. Natl Acad. Sci. USA*, 96:4971–6, 1999.

[16] Z. Hu and J. Lutkenhaus. Topological regulation of cell division in *Escherichia coli* involves rapid pole to pole oscillation of the division inhibitor MinC under the control of MinD and MinE. *Mol. Microbiol.*, 34:82–90, 1999.

[17] A.M. Turing. The chemical basis of morphogenesis. *Phil. Trans. R. Soc. B*, 237:37–72, 1952.

[18] L. Wolpert. Positional information and the spatial pattern of cellular differentiation. *J. Theor. Biol.*, 25:1–47, 1969.

[19] M. Howard and K. Kruse. Cellular organization by self-organization: mechanisms and models for Min protein dynamics. *J. Cell Biol.*, 168:533–6, 2005.

[20] A.J. Koch and H. Meinhardt. Biological pattern formation: from basic mechanisms to complex structures. *Rev. Mod. Phys.*, 66:1481–507, 1994.

[21] J.D. Murray. A pre-pattern formation mechanism for animal coat markings. *J. Theor. Biol.*, 88:161–99, 1981.

[22] S. Sick, S. Reinker, J. Timmer, and T. Schlake. WNT and DKK Determine Hair Follicle Spacing Through a Reaction-Diffusion Mechanism. *Science*, 314:1447–50, 2006.

[23] X. Fu, Y.-L. Shih, Y. Zhang, and L.I. Rothfield. The MinE ring required for proper placement of the division site is a mobile structure that changes its cellular location during the *Escherichia coli* division cycle. *Proc. Natl Acad. Sci. USA*, 98:980–5, 2001.

[24] C.A. Hale, H. Meinhardt, and P.A.J. de Boer. Dynamic localization cycle of the cell division regulator MinE in *Escherichia coli*. *EMBO J.*, 20:1563–72, 2001.

[25] L.L. Lackner, D.M. Raskin, and P.A.J. de Boer. ATP-Dependent Interactions between *Escherichia coli* Min Proteins and the Phospholipid Membrane In Vitro. *J. Bacteriol.*, 185:735–49, 2003.

[26] Z. Hu, E.P. Gogol, and J. Lutkenhaus. Dynamic assembly of MinD on phospholipid vesicles regulated by ATP and MinE. *Proc. Natl Acad. Sci. USA*, 99:6761–6, 2002.

[27] K. Suefuji, R. Valluzzi, and D. RayChaudhuri. Dynamic assembly of MinD into filament bundles modulated by ATP, phospholipids, and MinE. *Proc. Natl Acad. Sci. USA*, 99:16776–81, 2002.

[28] J. Huang, C. Cao, and J. Lutkenhaus. Interaction between FtsZ and inhibitors of cell division. *J. Bacteriol.*, 178:5080–5, 1996.

[29] Z. Hu, A. Mukherjee, S. Pichoff, and J. Lutkenhaus. The MinC component of the division site selection system in *Escherichia coli* interacts with FtsZ to prevent polymerization. *Proc. Natl Acad. Sci. USA*, 96:14819–24, 1999.

[30] D.M. Raskin and P.A.J. de Boer. MinDE-Dependent Pole-to-Pole Oscillation of Division Inhibitor MinC in *Escherichia coli*. *J. Bacteriol.*, 181:6419–24, 1999.

[31] H. Meinhardt and P.A.J. de Boer. Pattern formation in Escherichia coli: A model for the pole-to-pole oscillations of Min proteins and the localization of the division site. *Proc. Natl Acad. Sci. USA*, 98:14202–7, 2001.

[32] M. Howard, A.D. Rutenberg, and S. de Vet. Dynamic Compartmentalization of Bacteria: Accurate Division in *E. Coli*. *Phys. Rev. Lett.*, 87:278102, 2001.

[33] K. Kruse. A Dynamic Model for Determining the Middle of *Escherichia coli*. *Biophys. J.*, 82:618–27, 2002.

[34] K.C. Huang, Y. Meir, and N.S. Wingreen. Dynamic structures in *Escherichia coli*: Spontaneous formation of MinE rings and MinD polar zones. *Proc. Natl Acad. Sci. USA*, 100:12724–8, 2003.

[35] Y.-L. Shih, T. Le, and L.I. Rothfield. Division site selection in *Escherichia coli* involves dynamic redistribution of Min proteins within coiled structures that extend between the two cell poles. *Proc. Natl Acad. Sci. USA*, 100:7865–70, 2003.

[36] G. Meacci and K. Kruse. Min-oscillations in *Escherichia coli* induced by interactions of membrane-bound proteins. *Phys. Biol.*, 2:89–97, 2005.

[37] D.A. Drew, M.J. Osborn, and L.I. Rothfield. A polymerization-depolymerization model that accurately generates the self-sustained oscillatory system involved in bacterial division site placement. *Proc. Natl Acad. Sci. USA*, 102:6114–8, 2005.

[38] N. Pavin, H.Č. Paljetak, and V. Krstić. Min-protein oscillations in *Escherichia coli* with spontaneous formation of two-stranded filaments in a three-dimensional stochastic reaction-diffusion model. *Phys. Rev. E*, 72:021904, 2006.

[39] E.N. Cytrynbaum and B.D.L. Marshall. A Multistranded Polymer Model Explains MinDE Dynamics in *E. coli* Cell Division. *Biophys. J.*, 93:1134–50, 2007.

[40] F. Tostevin and M. Howard. A stochastic model of Min oscillations in *Escherichia coli* and Min protein segregation during cell division. *Phys. Biol.*, 3:1–12, 2006.

[41] M. Howard and A.D. Rutenberg. Pattern Formation inside Bacteria: Fluctuations due to the Low Copy Number of Proteins. *Phys. Rev. Lett.*, 90:128102, 2003.

[42] D. Fange and J. Elf. Noise-Induced Min Phenotypes in *E. coli*. *PLOS Comput. Biol.*, 2:e80, 2006.

[43] A.L. Marston and J. Errington. Selection of the midcell division site in Bacillus subtilis through MinD-dependent polar localization and activation of MinC. *Mol. Microbiol.*, 33:84–96, 1999.

[44] M. Howard. A Mechanism for Polar Protein Localization in Bacteria. *J. Mol. Biol.*, 335:655–63, 2004.

[45] M. Thanbichler and L. Shapiro. MipZ, a Spatial Regulator Coordinating Chromosome Segregation with Cell Division in *Caulobacter*. *Cell*, 126:147–62, 2006.

[46] G.C. Brown and B.N. Kholodenko. Spatial gradients of cellular phosphoproteins. *FEBS Lett.*, 457:452–4, 1999.

[47] J.R. Robbins, D. Monack, S.J. McCallum, A. Vegas, E. Pham, M.B. Goldberg, and J.A. Theriot. The making of a gradient: IcsA (VirG) polarity in *Shigella flexneri*. *Mol. Microbiol.*, 41:861–72, 2001.

[48] S. Celton-Morizur, V. Racine, J.-B. Sibarita, and A. Paoletti. Pom1 kinase links division plane position to cell polarity by regulating Mid1p cortical distribution. *J. Cell Sci.*, 119:4710–8, 2006.

[49] N.N. Padte, S.G. Martin, M. Howard, and F. Chang. The Cell-End Factor Pom1p Inhibits Mid1p in Specification of the Cell Division Plane in Fission Yeast. *Curr. Biol.*, 16:2480–7, 2006.

[50] P. Kalb, K. Weis, and R. Heald. Visualization of a Ran-GTP Gradient in Interphase and Mitotic *Xenopus* Egg Extracts. *Science*, 295:2452–6, 2002.

[51] P. Niethammer, P. Bastiaens, and E. Karsenti. Stathmin-Tubulin Interaction Gradients in Motile and Mitotic Cells. *Science*, 303:1862–6, 2004.

[52] M. Caudron, G. Bunt, P. Bastiaens, and E. Karsenti. Spatial Coordination of Spindle Assembly by Chromosome-Mediated Signaling Gradients. *Science*, 309:1373–6, 2005.

[53] R. Wollman, E.N. Cytrynbaum, J.T. Jones, T. Meyer, J.M. Scholey, and A. Mogilner. Efficient Chromosome Capture Requires a Bias in the 'Search-and-Capture' Process during Mitotic-Spindle Assembly. *Curr. Biol.*, 15:828–32, 2005.

[54] J. Wong and G. Fang. HURP controls spindle dynamics to promote proper interkinetochore tension and efficient kinetochore capture. *J. Cell Biol.*, 173:879–91, 2006.

[55] J. Meyers, J. Craig, and D.J. Odde. Potential for Control of Signaling Pathways via Cell Size and Shape. *Curr. Biol.*, 16:1685–93, 2006.

[56] M. Howard. Cell Signalling: Changing Shape Changes the Signal. *Curr. Biol.*, 16:R673–5, 2006.

[57] W. Driever and C. Nusslein-Volhard. A gradient of bicoid protein in *Drosophila* embryos. *Cell*, 54:83–93, 1988.

[58] W. Driever and C. Nusslein-Volhard. The bicoid protein determines position in the *Drosophila* embryo in a concentration-dependent manner. *Cell*, 54:95–104, 1988.

[59] W. Driever and C. Nusslein-Volhard. The bicoid protein is a positive regulator of hunchback transcription in the early *Drosophila* embryo. *Nature*, 337:138–43, 1989.

[60] K.M. Cadigan, M.P. Fish, E.J. Rulifson, and R. Nusse. Wingless repression of *Drosophila frizzled* 2 expression shapes the wingless morphogen gradient in the wing. *Cell*, 93:767–77, 1998.

[61] E.V. Entchev, A. Schwabedissen, and M. González-Gaitán. Gradient formation by the TGF-beta homolog Dpp. *Cell*, 103:981–91, 2000.

[62] L. Niswander, S. Jeffrey, G.R. Martin, and C. Tickle. A positive feedback loop coordinates growth and patterning in the vertebrate limb. *Nature*, 371:609–12, 1994.

[63] E. McGlinn and C.J. Tabin. Mechanistic insight into how shh patterns the vertebrate limb. *Curr. Opin. Genet. Dev.*, 16:426–32, 2006.

[64] A. Poh, A. Karunaratne, G. Kolle, N. Huang, Smith E., J. Starkey, D. Wen, I. Wilson, T. Yamada, and M. Hargrave. Patterning of the vertebrate ventral spinal cord. *Int. J. Dev. Biol.*, 46:597–608, 2002.

[65] D. Tannahill, L.W. Harris, and R. Keynes. Role of morphogens in brain growth. *J. Neurobiol.*, 64:367–75, 2005.

[66] A. Eldar, D. Rosin, B.-Z. Shilo, and N. Barkai. Self-Enhanced Ligand Degradation Underlies Robustness of Morphogen Gradients. *Dev. Cell*, 5:635–46, 2003.

[67] M. Howard and P.R. ten Wolde. Finding the centre reliably: robust patterns of developmental gene expression. *Phys. Rev. Lett.*, 95:208103, 2005.

[68] P. McHale, W.-J. Rappel, and H. Levine. Embryonic pattern scaling achieved by oppositely directed morphogen gradients. *Phys. Biol.*, 3:107–20, 2006.

[69] M.B. Elowitz, A.J. Levine, E.D. Siggia, and P.S. Swain. Stochastic Gene Expression in a Single Cell. *Science*, 297:1183–6, 2002.

[70] M. Thattai and A. van Oudenaarden. Intrinsic noise in gene regulatory networks. *Proc. Natl Acad. Sci. USA*, 98:8614–9, 2001.

[71] J. Paulsson. Summing up the noise in gene networks. *Nature*, 427:415–8, 2004.

[72] H.C. Berg and E.M. Purcell. Physics of chemoreception. *Biophys. J.*, 20:193–217, 1977.

[73] W. Bialek and S. Setayeshgar. Physical limits to biochemical signalling. *Proc. Natl Acad. Sci. USA*, 102:10040–5, 2005.

[74] F. Tostevin, P.R. ten Wolde, and M. Howard. Fundamental limits to position determination by concentration gradients. *PLOS Comput. Biol.*, 3:e78, 2007.

[75] X.-C. Yu and W. Margolin. FtsZ ring clusters in *min* and partition mutants: role of both the Min system and the nucleoid in regulating FtsZ ring localization. *Mol. Microbiol.*, 32:315–26, 1999.

[76] M.D. Migocki, M.K. Freeman, R.G. Wake, and E.J. Harry. The Min system is not required for precise placement of the midcell Z ring in *Bacillus subtilis*. *EMBO Rep.*, 3:1163–7, 2002.

[77] H.H. McAdams and L. Shapiro. A Bacterial Cell-Cycle Regulatory Network Operating in Time and Space. *Science*, 301:1874–7, 2003.

[78] J.-Y. Matroule, H. Lam, D.T. Burnette, and C. Jacobs-Wagner. Cytokinesis monitoring during development: Rapid pole-to-pole shuttling of a signaling protein by localized kinase and phosphatase in *Caulobacter*. *Cell*, 118:579–90, 2004.

[79] J. Errington. Regulation of endospore formation in *Bacillus subtilis*. *Nat. Rev. Microbiol.*, 1:117–26, 2003.

[80] P.J. Piggot and D.W. Hilbert. Sporulation of *Bacillus subtilis*. *Curr. Opin. Microbiol.*, 7:579–86, 2004.

[81] J. Chant and J.R. Pringle. Budding and cell polarity in *Saccharomyces cerevisiae*. *Curr. Opin. Genet. Dev.*, 1:342–50, 1991.

[82] J. Chant. Cell polarity in yeast. *Annu. Rev. Cell Dev. Biol.*, 15:365–91, 1999.

[83] K. Madden and M. Snyder. Cell polarity and morphogenesis in budding yeast. *Annu. Rev. Microbiol.*, 52:687–744, 1998.

[84] C. Jones and P. Chen. Planar cell polarity signaling in vertebrates. *Bioessays*, 29:120–32, 2007.

[85] J.A. Zallen. Planar polarity and tissue morphogenesis. *Cell*, 129:1051–63, 2007.

[86] K. Shin, V.C. Fogg, and B. Margolis. Tight junctions and cell polarity. *Annu. Rev. Cell Dev. Biol.*, 22:2207–35, 2006.

[87] M. Götz and W.B. Huttner. The cell biology of neurogenesis. *Nat. Rev. Mol. Cell Biol.*, 6:777–88, 2005.

[88] G.R. Wiggin, J.P. Fawcett, and T. Pawson. Polarity proteins in axon specification and synaptogenesis. *Dev. Cell*, 8:803–16, 2005.

[89] A.C. Horton and M.D. Ehlers. Neuronal polarity and trafficking. *Neuron*, 40:277–95, 2003.

[90] I.G. Macara. Parsing the polarity code. *Nat. Rev. Mol. Cell Biol.*, 5:220–31, 2004.

[91] A. Suzuki and S. Ohno. The PAR-aPKC system: lessons in polarity. *J. Cell Sci.*, 119:979–87, 2006.

[92] B. Goldstein and I.G. Macara. The PAR proteins: Fundamental players in animal cell polarization. *Dev. Cell*, 13:609–22, 2007.

[93] F.E. Duncan, S.B. Moss, R.M. Schultz, and C.J. Williams. PAR-3 defines a central subdomain of the cortical actin cap in mouse eggs. *Dev. Biol.*, 280:38–47, 2005.

[94] T. Nishimura, T. Yamaguchi, K. Kato, M. Yoshizawa, Y. Nabeshima, S. Ohno, M. Hoshino, and K. Kaibuchi. PAR-6-PAR-3 mediates Cdc42-induced Rac activation through the Rac GEFs STEF/Tiam1. *Nat. Cell Biol.*, 7:270–7, 2005.

[95] E. Munro. PAR proteins and the cytoskeleton: a marriage of equals. *Curr. Opin. Cell Biol.*, 18:86–94, 2006.

[96] J. Sulston, E. Schierenberg, J. White, and N. Thomson. The embryonic cell lineage of the nematode *Caenorhabditis elegans*. *Dev. Biol.*, 100:64–119, 1983.

[97] S. Strome and W.B. Wood. Immunofluorescence visualization of germ-line-specific cytoplasmic granules in embryos, larvae, and adults of *Caenorhabditis elegans*. *Proc. Natl Acad. Sci. USA*, 79:1558–62, 1982.

[98] A.A. Hyman and J.G. White. Determination of cell division axes in the early embryogenesis of *Caenorhabditis elegans*. *J. Cell Biol.*, 105:2123–35, 1987.

[99] S.N. Hird, J.E. Paulsen, , and S. Strome. Segregation of germ granules in living *Caenorhabditis elegans* embryos: cell-type-specific mechanisms for cytoplasmic localisation. *Development*, 122:1303–12, 1996.

[100] C.M. Schubert, R. Lin, C.J. de Vries, R.H.A. Plasterk, and J.R. Priess. MEX-5 and MEX-6 function to establish soma/germline asymmetry in early *C. elegans* embryos. *Mol. Cell*, 5:671–82, 2000.

[101] K. Kemphues. PARsing embryonic polarity. *Cell*, 101:345–48, 2000.

[102] S.W. Grill, J. Howard, E. Schaffer, E.H. Stelzer, and A.A. Hyman. The distribution of active force generators controls mitotic spindle position. *Science*, 301:518–21, 2003.

[103] B. Goldstein and S.N. Hird. Specification of the anteroposterior axis in *Caenorhabditis elegans*. *Development*, 122:1467–74, 1996.

[104] A.A. Cuenca, A. Schetter, D. Aceto, K. Kemphues, and G. Seydoux. Polarization of the *C. elegans* zygote proceeds via distinct establishment and maintenance phases. *Development*, 130:1255–65, 2003.

[105] R.J. Cheeks, J.C. Canman, W.N. Gabriel, N. Meyer, S. Strome, and B. Goldstein. *C. elegans* PAR proteins function by mobilizing and stabilizing asymmetrically localized protein complexes. *Curr. Biol.*, 14:851–62, 2004.

[106] S.N. Hird and J.G. White. Cortical and cytoplasmic flow polarity in early embryonic cells of *Caenorhabditis elegans*. *J. Cell Biol.*, 121:1343–55, 1993.

[107] E. Munro, J. Nance, and J.R. Priess. Cortical flows powered by asymmetrical contraction transport PAR proteins to establish and maintain anterior-posterior polarity in the early *C. elegans* embryo. *Dev. Cell*, 7:413–24, 2004.

[108] G.F. King, S.L. Roland, B. Pan, J.P. Mackay, G.P. Mullen, and L.I. Rothfield. The dimerization and topological specificity functions of MinE reside in a structurally autonomous C-terminal domain. *Mol. Microbiol.*, 31:1161–9, 1999.

[109] Y.-L. Shih, X. Fu, G.F. King, T. Le, and L.I. Rothfield. Division site placement in *E.coli*: mutations that prevent formation of the MinE ring lead to loss of the normal midcell arrest of growth of polar MinD membrane domains. *EMBO J.*, 21:3347–57, 2002.

[110] M.B. Elowitz, M.G. Surette, P.-E. Wolf, J.B. Stock, and S. Leibler. Protein Mobility in the Cytoplasm of *Escherichia coli*. *J. Bacteriol.*, 181:197–203, 1999.

[111] V. Krstić, Z. Maglica, H.Č. Paljetak, B. Podobnik, and N. Pavin. Min-protein Oscillations in *E. coli*: Three-Dimensional Off-Lattice Stochastic Reaction-Diffusion Model. *J. Stat. Phys.*, 128:5–20, 2006.

[112] S. Sengupta and A. Rutenberg. Modeling partitioning of Min proteins between daughter cells after septation in *Escherichia coli*. *Phys. Biol.*, 4:145–53, 2007.

[113] S. Rueda, M. Vicente, and J. Mingorance. Concentration and Assembly of the Division Ring Proteins FtsZ, FtsA, and ZipA during the *Escherichia coli* Cell Cycle. *J. Bacteriol.*, 185:3344–51, 2003.

[114] S.J.R. Arends and D.S. Weiss. Inhibiting Cell Division in Escherichia coli Has Little If Any Effect on Gene Expression. *J. Bacteriol.*, 186:880–4, 2003.

[115] B. Houchmandzadeh, E. Wieschaus, and S. Leibler. Establishment of developmental precision and proportions in the early *Drosophila* embryo. *Nature*, 415:798–802, 2002.

[116] A. Kicheva, P. Pantazis, T. Bollenbach, Y. Kalaidzidis, T. Bittig, F. Julicher, and M. Gonzalez-Gaitan. Kinetics of Morphogen Gradient Formation. *Science*, 315:521–5, 2007.

[117] P.B. Detwiler, S. Ramanathan, A. Sengupta, and B.I. Shraiman. Engineering Aspects of Enzymatic Signal Transduction: Photoreceptors in the Retina. *Biophys. J.*, 79:2801–17, 2000.

[118] T. Shibata and K. Fujimoto. Noisy signal amplification in ultrasensitive signal transduction. *Proc. Natl Acad. Sci. USA*, 102:331–6, 2005.

[119] S. Tanase-Nicola, P.B. Warren, and P.R. ten Wolde. Signal Detection, Modularity, and the Correlation between Extrinsic and Intrinsic Noise in Biochemical Networks. *Phys. Rev. Lett.*, 97:068102, 2006.

[120] B. Houchmandzadeh, E. Wieschaus, and S. Leibler. Precise domain specification in the developing *Drosophila* embryo. *Phys. Rev. E*, 72:061920, 2005.

[121] U.C. Täuber, M. Howard, and B.P. Vollmayr-Lee. Applications of field-theoretic renormalization group methods to reaction-diffusion problems. *J. Phys. A: Math. Gen.*, 38:R79–131, 2005.

[122] J. Magdalena and M.B. Goldberg. Quantification of *Shigella* IcsA Required for Bacterial Actin Polymerization. *Cell Motil. Cytoskeleton*, 51:187–96, 2002.

[123] H. Müller-Krumbhaar and K. Binder. Dynamic Properties of the Monte Carlo Method in Statistical Mechanics. *J. Stat. Phys.*, 8:1–24, 1973.

[124] J.L. England and J. Cardy. Morphogen Gradient from a Noisy Source. *Phys. Rev. Lett.*, 94:078101, 2005.

[125] B.D. Harfe, P.J. Scherz, S. Nissim, H. Tian, A.P. McMahon, and C.J. Tabin. Evidence for an expansion-based temporal Shh gradient in specifying vertebrate digit identities. *Cell*, 118:517–28, 2004.

[126] S. Ahn and A.L. Joyner. Dynamic changes in the response of cells to positive hedgehog signalling during mouse limb partitioning. *Cell*, 118:505–16, 2004.

[127] H.-C. Park, J. Shin, and B. Appel. Spatial and temporal regulation of ventral spinal cord precursor specification by Hedgehog signalling. *Development*, 131:5959–69, 2004.

[128] G. Horning, B. Berkowitz, and N. Barkai. Morphogen gradient formation in a complex environment: An anomalous diffusion model. *Phys. Rev. E*, 72:041916, 2005.

[129] E. Ben-Naim and S. Redner. Inhomogeneous two-species annihilation in the steady state. *J. Phys. A: Math. Gen.*, 25:L575–83, 1992.

[130] S. Cornell and M. Droz. Steady-state reaction-diffusion front scaling for $mA + nB \rightarrow$[inert]. *Phys. Rev. Lett.*, 70:3824–7, 1993.

[131] B.P. Lee and J. Cardy. Scaling of reaction zones in the $A + B \rightarrow 0$ diffusion-limited reaction. *Phys. Rev. E*, 50:R3287–90, 1994.

[132] M. Howard and J. Cardy. Fluctuation effects and multiscaling of the reaction-diffusion front for $A + B \rightarrow \emptyset$. *J. Phys. A: Math. Gen.*, 28:3599–621, 1995.

[133] G.T. Barkema, M.J. Howard, and J.L. Cardy. Reaction-diffusion front for $A + B \rightarrow \emptyset$ in one dimension. *Phys. Rev. E*, 53:R2017–20, 1996.

[134] K.J. Kemphues, J.R. Priess, D.G. Morton, and N.S. Cheng. Identification of genes required for cytoplasmic localization in early *C. elegans* embryos. *Cell*, 52:311–20, 1988.

[135] S. Guo and K.J. Kemphues. A non-muscle myosin required for embryonic polarity in *Caenorhabditis elegans*. *Nature*, 382:455–8, 1996.

[136] L. Boyd, S. Guo, D. Levitan, D.T. Stinchcomb, and K.J. Kemphues. PAR-2 is asymmetrically distributed and promotes association of P granules and PAR-1 with the cortex in *C. elegans* embryos. *Development*, 122:3075–84, 1996.

[137] Y. Tabuse, Y. Izumi, F. Piano, K.J. Kemphues, J. Miwa, and S. Ohno. Atypical protein kinase C cooperates with PAR-3 to establish embryonic polarity in *Caenorhabditis elegans*. *Development*, 125:3607–14, 1998.

[138] T.-J. Hung and K.J. Kemphues. PAR-6 is a conserved PDZ domain-containing protein that colocalized with PAR-3 in *Caenorhabditis elegans* embryos. *Development*, 126:127–35, 1999.

[139] S. Strome. Flourescence visualization of the distribution of microfilaments in gonads and early embryos of the nematode *Caenorhabditis elegans*. *J. Cell Biol.*, 103:2241–52, 1986.

[140] D. Aceto, M. Beers, and K.J. Kemphues. Interaction of PAR-6 with CDC-42 is required for maintenance but not establishment of PAR asymmetry in *C. elegans*. *Dev. Biol.*, 299:386–97, 2006.

[141] S. Schonegg and A.A. Hyman. CDC-42 and RHO-1 coordinate acto-myosin contractility and PAR protein localization during polarity establishment in *C. elegans* embryos. *Development*, 133:3507–16, 2006.

[142] Y. Hao, L. Boyd, and G. Seydoux. Stabilization of cell polarity by the *C. elegans* RING protein PAR-2. *Dev. Cell*, 10:199–208, 2006.

[143] R. Benton and D. St Johnston. Drosophila PAR-1 and 14-3-3 inhibit Bazooka/PAR-3 to establish complementary cortical domains in polarized cells. *Cell*, 115:691–704, 2003.

[144] D.G. Morton, D.C. Shakes, S. Nugent, D. Dichoso, W. Wang, A. Golden, and K.J. Kemphues. The *Caenorhabditis elegans par-5* gene encodes a 14-3-3 protein required for cellular asymmetry in the early embryo. *Dev. Biol.*, 241:47–58, 2002.

[145] N. Jenkins, J.R. Saam, and S.E. Mango. CYK-4/GAP provides a localized cue to initiate anteroposterior polarity upon fertilization. *Science*, 313:1298–301, 2006.

[146] C. DeRenzo, K.J. Reese, and G. Seydoux. Exclusion of germ plasm proteins from somatic lineages by cullin-dependent degradation. *Nature*, 424:685–9, 2003.

[147] G. Seydoux, C.C. Mello, J. Pettitt, W.B. Wood, J.R. Priess, and A. Fire. Repression of gene expression in the embryonic germ lineage of *C. elegans*. *Nature*, 382:713–6, 1996.

[148] K. Ogura, N. Kishimoto, S. Mitani, K. Gengyo-Ando, and Y. Kohara. Translational control of maternal *glp-1* mRNA by POS-1 and its interacting protein SPN-4 in *Caenorhabditis elegans*. *Development*, 130:2495–503, 2003.

[149] I. D'Agostino, C. Merritt, P. Chen, G. Seydoux, and K. Subramaniam. Translational repression restricts expression of the *C. elegans* nanos homolog NOS-2 to the embryonic germline. *Dev. Biol.*, 292:244–52, 2006.

[150] J.M. Pagano, B.M. Farley, L.M. McCoig, and S.P. Ryder. Molecular basis of RNA recognition by the embryonic polarity determinant MEX-5. *J. Biol. Chem.*, 282:8883–94, 2007.

[151] J.L. Watts, B. Etemad-Moghadam, S. Guo, L. Boyd, B.W. Draper, C.C. Mello, J.R. Priess, and K.J. Kemphues. par-6, a gene involved in the establishment of asymmetry in early *C. elegans* embryos, mediates the asymmetric localization of PAR-3. *Development*, 122:3133–40, 1996.

[152] C.A. Rappleye, A. Tagawa, R. Lyczak, B. Bowerman, and R.V. Aroian. The anaphase-promoting complex and separin are required for embryonic anterior-posterior axis formation. *Dev. Cell*, 2:195–206, 2002.

[153] A.L. Marston, H.B. Thomaides, D.H. Edwards, M.E. Sharpe, and J. Errington. Polar localization of the MinD protein of *Bacillus subtilis* and its role in selection of the mid-cell division site. *J. Genes Dev.*, 12:3419–30, 1998.

[154] J.-R. Huynh and D. St Johnston. The origin of asymmetry: Early polarisation of the *Drosophila* germline cyst and oocyte. *Curr. Biol.*, 14:R438–49, 2004.